A HYBRID MODEL BASED ON FUNCTIONAL DECOMPOSITION FOR VORTEX SHEDDING SIMULATIONS

By

Qian Li

B. Eng.

Supervisor

Prof. Qingwei Ma

A thesis submitted to

City, University of London

for the degree of

Doctor of Philosophy

School of Mathematics, Computer Science and Engineering

City, University of London

September, 2017

CONTENTS

LIST OF FIGURES

LIST OF TABLES

ACKNOWLEDGEMENTS

I would like to express my sincere gratitude to my supervisor Prof. Qingwei Ma, for his continuous support and guidance. His keen enthusiasm for research always inspire me and encourage me. I really appreciate the knowledge and the insight he has shared with me in our weekly meeting.

Many thanks go to my second supervisor Dr. Shiqiang Yan. I appreciate the patient and generous help he gives me every time I stuck in my research. His high standard requirement and hard-working attitude towards work inspired me a lot as a researcher. Prof. Qingwei Ma and Dr.Shiqiang Yan, they both have taught me so much, and set a good example for my career and life.

Furthermore, the accomplish of this thesis has benefited from the valuable comments given by Prof. Qingwei Ma, Dr. Shiqiang Yan and Dr. Jinghua Wang.

Special thanks to the members of our research group with who I have spent an unforgettable time together and friends in the department have helped me along the way.

I am very thankful for the guidance comes from Prof. Weiping Huang and Prof. Lin Zhao. Thanks for their support and encouragement at the Ocean University of China throughout my master study.

I appreciate the sponsorship provided by China Scholarship Council. Also, thanks for the scholarship from Prof. Qingwei Ma and Dr. Shiqiang Yan during my study.

To my dearest Mom and Dad, thanks for your endless love and support. You are always my source of strength and power. Thanks for being such wonderful parents and making me feel so luck by encouraging me and standing by me every step of the way.

DECLARATION

No portion of the work referred in the thesis has been submitted in support of an application for other degree or qualification of this or any other university or other institute of learning.

I grant powers of discretion to the City, University of London's Library to allow this thesis to be copied in whole or in part without any reference to me. This permission covers only single copies made for study purpose subject to the normal condition of acknowledgement.

Qian Li

ABSTRACT

Vortex-Induced Vibration (VIV) is one of the significant physics that encounter in the engineering practice. The good understanding of the structure response and technologies to suppress the significant vibration and undesirable forces induced by VIV is of vital importance for the entire design/planning procedure. However, for both the single-phase and multiphase flow, the main challenge is how to significantly improve the simulation efficiency and meanwhile maintain the accuracy.

This research aims to develop a hybrid model which can simulate VIV significantly more efficiently. A novel framework for a hybrid model which is based on the functional decomposition is proposed. The theoretical hypothesis of the hybrid model is that the viscous effect is only significant near the offshore structures or breaking waves, and may be ignored in other areas. In this model, all physical variables are split into two parts. One part is solved by a quasi-turbulent model in whole domain and the other part solved by using a residual turbulent model in a smaller domain. The two models are implemented simultaneously based on their respective meshes and time steps. Due to this feature, the techniques such as the sub-cycle strategy are employed for the improvement of the efficiency without the deterioration of the accuracy.

In this work, the equations and boundary conditions of the hybrid model for single phase and multiphase flow are derived. Corresponding algorithms and codes are developed using the open-source platform of OpenFOAM. The method is validated by simulating representative cases of flows past stationary and oscillating circular cylinder under various combinations of (*Re, A/D, Fr*) for single phase and of flows past stationary circular cylinder underneath an air-water interface for multiphase. It is demonstrated that the results of the hybrid model agree well with experimental data and with those obtained by using the original OpenFOAM. The investigation is also carried out on the efficiency of the hybrid model and indicate that the computational time of the hybrid model is significantly less than that of original OpenFOAM to obtain the similar results for the same cases. The investigation also indicates that the higher the Reynolds number, the larger the oscillation amplitude, the more computational time can be saved by using

the new hybrid model. In some case, the hybrid model can save 80% of the computational time than using the original OpenFOAM solver.

LIST OF SYMBOLS AND TECHNICAL TERMS

A	Oscillation amplitude
A/D	Amplitude ratio
D	Cylinder diameter
G	Spatial filter
N	Number of members of the ensemble
T	Wave period
U	Free stream flow velocity
$\overline{C_D}$	Mean drag coefficient
$C_{L\,rms}$	Root mean square lift coefficient
C_L, C_D	Drag and lift coefficients
C_{LA}	Amplitude of the fluctuating lift coefficient
C_μ	$C_\mu = 0.09$, constant in the k-ε turbulent model
D_c	Crossflow direction domain size
D_{in}	Distance between inlet and cylinder
D_{out}	Cylinder to outlet distance
F_L, F_D	Fluid drag and lift force
F_T	Transition frequency
F_r	Frequency ratio
F_r'	Froude number
N_c	Critical sub-cycle number
N_s	Sub-cycle number

N_t	Total number of independent samples
R_e	Reynolds number (UD/v)
S_t	Strouhal number
$\overline{U}$	Assemble average velocity of the flow
U_{max}	Maximum velocity magnitude estimated by quasi-turbulent model
U^*_{max}	Maximum velocity magnitude estimated by the residual model
U_r	Reduced velocity
W_C	Critical width of the significant turbulent viscosity zone
f_n	Fundamental natural frequency
f_o	Exciting frequency
f_s	Vortex-shedding frequency
m^*	Fluid added masses
u^*, p^*	Velocity and pressure of the residual field
u_T, p_T	Velocity and pressure of the total field
$u_{ni}(x_i, t)$	$u(x_i, t)$ at the n^{th} series
u_{pi}	Potential component of the total velocity in the complementary RANS equations
y^+	Distance from the wall measured in viscous lengths
y_w	Distance from the centre of the first cell to the wall
d	Water depth
h	Distance from the cylinder to the free surface
h/D	Submerged depth
Γ_c	Coupling boundary in the hybrid method
Ω_R	Overlapping sub-domain
τ_{ij}^{LES}	Shear stress term in LES
Ω_T	Quasi-turbulent solver domain
Ω_{T1}	Same domain size to Ω_R but different solver is implemented
$\overline{u_i' u_j'}$	Reynolds stresses
Φ_1	Function of the wall

a_{ij}	Deviatoric part of the Reynolds stresses
c_α	Interface compression coefficient
u_{bi}	Velocity with which the integration boundary (r) moves.
$u_i'(x_i, t)$	Fluctuation of the time-averaged value
u_τ	Friction velocity
δ_ν	Viscous length scale
μ_{air}, μ_w	Dynamic viscosity of air and water
$\mu_{eff}(x_i, t)$	Effective dynamic viscosity
$\nu_T(x_i, t)$	Turbulent /eddy viscosity
$\nu_{eff}(x_i, t)$	Effective kinematic viscosity
$\rho_{air,}\, \rho_w$	Densities of air and water
τ_w	Wall shear stress
φ_{lift}	Lift angle
ΔL	Minimum mesh size in the quasi-turbulent domain
$\Delta T1$	Time step for the quasi-turbulent field
$\Delta T2$	Time step for the residual solver
Δl	Minimum mesh size in the residual field domain
α	Volume fraction
γ	Diffusion coefficient
Δf	Filter width
σ	Surface tension coefficient
κ	Local interfacial curvature
k	Turbulent kinetic energy
Φ	Velocity potential
$\nabla \frac{1}{f}$	Surface gradient operator
δ	Boundary-layer thickness
ε	Turbulent dissipation
θ	Phase of the harmonic oscillation
κ	Von Karman constant

λ	Wavelength
μ	Dynamic viscosity
$\mu'(x_i, t)$	Effective dynamic viscosity of the quasi-turbulent field
ν	Constant molecular viscosity
$\nu'(x_i, t)$	Effective kinematic viscosity of the quasi-turbulent field
ρ	Flow density
ω	Specific turbulent dissipation rate

Abbreviation

2G-URANS	Second-Generation URANS
ALE	Arbitrary Lagrangian–Eulerian
DES	Detached Eddy Simulation
DNS	Direct Numerical Simulation
DOF	Degree of freedom
FEM	Finite Element Method
FFT	Fast Fourier Transform
FNPT	Fully Nonlinear Potential Theory
FSI	Fluid-Structure Interaction
FVM	Finite Volume Method
HOS	Higher-Order Spectrum method
HPC	High-Performance Computing
HR	High Reynolds number wall treatment
IMLPG_R	Improved Meshless Local Petrov Galerkin method with Rankine source solution
KC	Keulegan Carpenter number
LES	Large Eddy Simulations
LR	Low Reynolds number wall treatment
MLPG	Meshless Local Petrov Galerki
MPS	Moving Particle Semi-implicit
MULES	Multi-dimensional Universal Limiter for Explicit Solution
NS	Navier–Stokes

2P	Two vortex pairs each cycle
PANS	Partially Filtered Navier-Stokes
PISO	Pressure Implicit with Splitting of Operators
QALE	Quasi-Arbitrary-Lagrangian-Eulerian
QDNS	Quasi-Direct Numerical Simulation
RANS	Reynolds-Averaged Navier–Stokes equations
RKE	Realizable k-ω turbulent model
RMS	Root mean square
2S	Two single vortices shed each cycle
S-A	Spalart–Allmaras turbulent model
SGS	Sub Grid Scale
SPH	Smoothed Particle Hydrodynamics
SST	Shear-Stress-Transport model
SWENSE	Spectral Wave Explicit Navier-Stokes Equations approach
URANS	Unsteady Reynolds-averaged Navier–Stokes equations
VEM	Vortex Element Methods
VIV	Vortex Induced Vibration
VLES	Very-Large Eddy Simulation
VOF	Volume of Fluid
WKO	Wilcox k-ω model

1

INTRODUCTION

1.1 Background

Vortex-Induced Vibration (VIV) is a motion induced on the bodies interacting with the external fluid flow and is closely related to the vortex shedding from the surface of the bodies. It is one of the significant physics that encounter in the engineering practice, in particular for cylindrical structures, such as transmission lines, aircraft control surfaces, buoyancy and spar hulls, risers and mooring lines, sub-sea pipelines, chimneys, bridges and so on. These structures are widely used in ocean engineering practices, e.g. oil/gas (Figure 1.1.1 is the illustration of FPSO Aoka Mizu, including its moorings and sub-sea flexible pipelines) and oceanic renewables industries. For instance, there were totally 3,858 oil and gas platforms extant in the Gulf of Mexico in 2006 and the operation water depth in the Brazil and Gulf of Mexico has exceeded 3000m (NOAA, 2013). The proportion of production wells at depths deeper than 300m was 95% by 2015 and more than 20% of Gulf wells were deeper than 2,000m in 2016 (CW Composites World, 2016). A great number of pipelines, risers and electric transmission lines have been and will be implemented. All these structures are subjected to the effects of VIV, which may lead to severe fatigue damage and threats to these structures. To avoid the

damage, the issues associated with VIV must be carefully addressed during the entire design/planning procedure, such as towing, installation, operation and demolishment. For this purpose, understanding of the structure response and technologies to suppress the significant vibration and undesirable forces induced by VIV become highly demanded.

Physical experiments and numerical investigations have been and are carried out in order to achieve a good understanding of the hydrodynamics associated with the VIV. In the aspect of numerical work, a Navier-Stokes (NS) solver with appropriate turbulence modelling is essential to resolve the vortex shedding and associated turbulent flow features. It is generally accepted that the optimal numerical computation strategy depends on the level of the complexity of the flow and the degree of accuracy needed for the flow of interest (Girimaji & Abdol-Hamid 2005). Conventionally, the most prevalent Reynolds-averaged Navier–Stokes (RANS) model is used to predict the mean statistical flow properties. In order to reflect the turbulent behaviour of the flow associated with VIV, an appropriate turbulence model (either one-equation or two-equation), such as Spalart–Allmaras(S–A) (Spalart & Allmaras, 1992) and k-ω models (Menter 1994; Menter 1993), are used to provide closure to the equation systems. Obviously, solving additional equations for the turbulent model leads to extra CPU time. Alternatively, the Large Eddy Simulations (LES) is well capable of handling a wider range of turbulence physics based on either explicitly or implicitly a length scale related to the numerical grid. However, the simulation conducted by LES is typically 10 ~ 100 times more expensive than RANS computations (Rodi 1997), partially because a much finer mesh resolution is required to realise the small-scale eddies, especially for the case with the wall-bounded flow. For example, for resolving the near-wall flow field, the computational cost of LES is scaled as $Re^{1.8}$, where Re is the Reynolds number, compared to that by the RANS modelling (Xiao & Jenny 2012). Nevertheless, the LES modelling typically spends less CPU time compared to the Direct Numerical Simulation (DNS), which is another and the most accurate way to resolve turbulence. For the latter, the corresponding scale factor is $Re^{2.25}$ (Xiao & Jenny 2012).

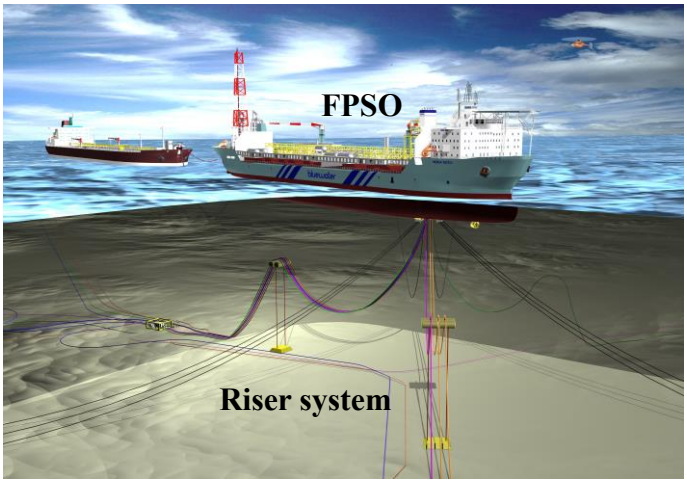

Figure 1.1.1 Offshore pipeline near the free surface (Bluewater, 2017)

No matter which way is applied, the computational cost for the VIV modelling is often high. In order to achieve reasonable results in an allowable CPU time, most of the numerical simulation of this kind is limited to a small computational domain surrounding the structures (~100*D*, where *D* is the characteristic dimension of the structure) and/or in two-dimension. It has also been demonstrated by Pope (2001) that, to capture the evolution of small eddies and to maintain the numerical stability, there are decreases of the spatial scales and temporal scales with the relationship of $Re^{-\frac{3}{4}}$ and $Re^{-\frac{1}{2}}$ respectively with the increase of the Reynolds number. The computational cost may be dramatically increases if a free surface flow is involved. In fact, for most of the offshore structures, which are often exposed to water waves, the free surface effect may need to be taken into account, especially, for the pipe segments near the water surface, as illustrated in Figure 1.1.1, and transmission pipelines during loading/offloading operation. Within the NS solver, one need to track or identify the free surface to correctly model the free surface flow and water waves. Classic models include multi-phase NS with volume of fluid technology (short as VOF and proposed by Hirt & Nichols (1981)), single-phase/multi-phase level set methods, multi-phase NS with marker-and-cell approach and single-phase/multi-phase meshless methods (e.g. Smoothed Particle Hydrodynamics (SPH), Moving Particle Semi-implicit method (MPS) and the Meshless Local Petrov Galerkin methods (MLPG)). Not only the extra cares on effectively resolving the free surface and accurately modelling the water wave

propagating, another constraint induced by the free surface flow is the size of the computational domain. It may be essential to cover the dimension in the depth direction from the water surface to the seabed, i.e. thousands meters for deep water application; at least 5~10 wave lengths (Wang 2016) in the horizontal plane at a scale of hundreds to thousands meter. Unfortunately, all the above-mentioned methods are too time-consuming for practical applications for such a large computational domain. Thus, simplified and empirical numerical models are widely used in the industrial design practices, with aid of experimental investigation. "*Is there any way to accelerate the computing without loss of accuracy?"* may be one of the most frequently questions in the numerical practices for VIV, high-Re problems and other problems with significant turbulent effects.

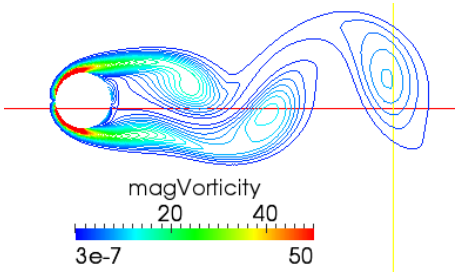

Figure 1.1.2 Illustration of vorticity distribution around a cylinder

One direct way for accelerating the numerical simulation is to conduct highly parallel computing using high-performance computing (HPC). On the other hand, efforts have been devoted to developing more robust modelling strategy or methodologies. The developments in these two directions do not conflict with each other and shall be combined to maximise the computational efficiency. In this work, the latter is focused.

One typical development for VIV of risers or mooring lines is the strip method (see Schulz & Meling (2004); Holmes *et al*. (2006); Bao *et al*. (2016)), which converts the three-dimensional problems to strips of 2D problems. In the strip method, the fluid stress on strips of the structure is modelled by 2D fluid-structure interaction (FSI) model where the structure motion and deformations are modelled by using 3D solid mechanics. This method simplifies the problem and dramatically improve the computational robustness. However, it is assumed that the fluid flow at different strip does not interact with each other. Furthermore, in the 2D FSI model of the strip method, the turbulence

modelling takes effects in the entire computational domain. In fact, the turbulent effects and vortex shedding may only be significant near the structure and in the wake area, as demonstrated by Figure 1.1.2, which shows the vorticity distribution around a fixed cylinder subjected to constraint inflow. Far away from these regions, the flow may be dominated by inertia force, e.g. gravity-driven flow, and the viscous effects may be ignored. In many cases, the potential flow may be sufficient to describe the flow feature in these regions, e.g. the propagation of the waves from far-field towards near field. This fact initiates the development of hybrid approaches, which combining different numerical methods and physical models.

Existing hybrid models for the problems considered in this study adopts two strategies, i.e. domain splitting (also called domain decomposition) and functional decomposition (also referred to as the velocity decomposition). For the domain splitting approach, the entire computational domain is split into two or more sub-domains, and different models are applied in different sub-domains (e.g. Quéméré *et al*., 2001; Quéméré & Sagaut (2002)). Taking the classic wave-structure interaction problems as an example (Figure 1.1.3(a)), RANS approach may be applied in the sub-domain near the structure (viscous domain) and the potential theory is applied in other sub-domains (inviscid domain, see, for example, Sriram *et al*. (2014); Yan & Ma (2017)). The success of models adopting this strategy usually relies on (1) a smooth transition between different sub-domains, e.g. the viscous effects, velocity-pressure relation; and (2) consistent solutions by different models at the interface between two sub-domains. For the former, a translational zone (or interface zone) is applied instead of a single interface; for the latter, an iteration may be necessary to ensure the boundary conditions of two models on the interfaces are satisfied simultaneously. The functional decomposition approach adopts a different domain configuration as shown in Figure 1.1.3(b), where a simpler model, e.g. the potential theory or Euler's equation is solved in the entire computational zone; only near the structure (dashed region in Figure 1.1.3(b), a complementary equation is solved and, consequently, the summation of the solutions to the simplified model and those to the complementary equation satisfies the RANS with or without turbulence models (e.g. Monroy & Ducrozet (2009); Luquet *et al*. (2007) and Ferrant *et al*. (2007)).

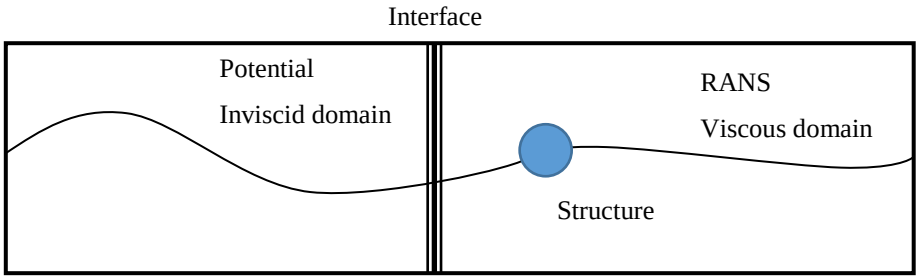

(a) The computational domain for the domain-splitting model

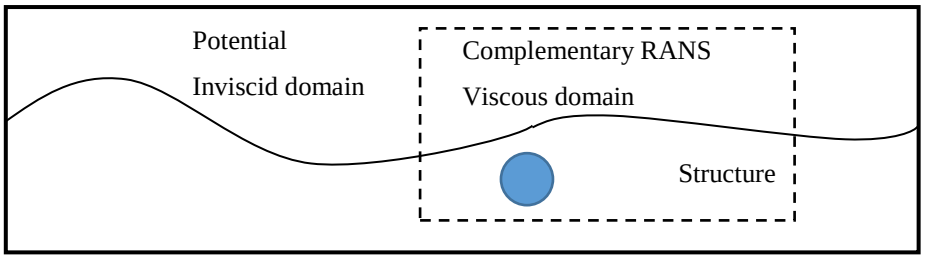

(b) The computational domain for the function-splitting model

Figure 1.1.3 Examples of different hybrid numerical models

By using these strategies, a few hybrid models have been developed. The majority couple (1) potential model and other higher-order potential model (e.g. Wang *et al.*, 2016); (2) potential theory (or other equivalent simplified model, e.g. nonlinear Schrödinger's equation and Euler's equation) and NS solver, e.g. RANS with or without turbulent modelling (e.g. Sriram *et al.*, 2014); (3) incompressible NS solver with compressible NS solver (e.g. Martínez Ferrer *et al.*, 2016); and (4) RANS approach with turbulent model and LES (Fan *et al.*,2017; Wei *et al.*, 2016; Sajjadi *et al.*, 2017; Kocutar *et al.*, 2015; Gopalan *et al.*, 2013). Considering the fact that the turbulence modelling is essential near the structure for the problems concerned here, i.e. VIV problems, available hybrid models may only couple the turbulent NS solver with either a potential theory (2) or another turbulent NS solver (4). Option (4) couples two turbulent NS solvers and, therefore, its computational efficiency may be impractical low; whereas Option (2) may suffer from a sudden change of the fluid properties from an inviscid/irrotational flow (no viscosity) to a turbulent flow (constant physical viscosity and unsteady turbulent/eddy viscosity), especially for high-Re problems, and consequently may be either numerically unstable or computationally costly (e.g.

requires large transitional zone for a smooth transition of viscous effects, large domain for solving turbulent models small time step size and so on).

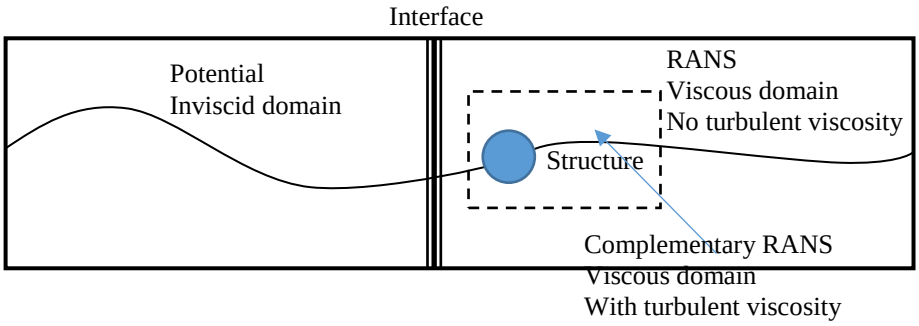

Figure 1.1.4 Proposed multi-model hybrid approach

This issue can be addressed by replacing the turbulent NS solver in Option (2) by a hybrid model coupling simplified RANS solver (e.g. the RANS without turbulent models) and turbulent NS solver (e.g. the RANS with turbulent model). Overall, one example of the new approach can be illustrated in Figure 1.1.4. The induction of the laminar NS solver (constant physical viscosity) between the inviscid/irrotational flow solver (no viscosity) and the turbulent flow solver (constant physical viscosity and unsteady turbulent/eddy viscosity) makes the viscous effects changes step by step, increasing the numerical instability. For the viscous domain, the solution of the turbulent modelling may only require in a small region near the structure, saving the CPU time on resolving the turbulent/eddy viscosity. To the best of my knowledge, no attempts have been found in the public domain to couple a simplified RANS solver with a turbulent solver.

1.2 Aim and objectives

This research aims to develop a hybrid model coupling a simplified RANS solver with a turbulent RANS solver for effectively modelling VIV. The functional decomposition (velocity decomposition) strategy is adopted. The objectives comprise:

1. Understanding the spatial-temporal distribution of the turbulent/eddy viscosity associated with flow around submerged structures with or without free surface effects, which is the foundation to develope the hybrid model;

2. Developing the hybrid model to couple the simplified RANS and turbulent RANS solvers;
3. Numerically investigating the performance of the developed hybrid model, e.g. the computational efficiency, accuracy and convergence;
4. Investigating the feasibility of coupling the developed hybrid model with a fully nonlinear potential model in a domain-splitting way, as sketched in Figure 1.1.4.

It is noted that only two-dimensional development and investigation will be considered in this thesis. One may apply the developed model to many scenarios, e.g. a long-span horizontal pipeline subjected to a unidirectional wave/current; a strip of the 2D fluid-structure interaction model in the above-mentioned strip method. One may also consider this research as a conceptional study, which proves the superiority of the hybrid model over the conventional model in terms of computational robustness, for the development of 3D hybrid model in the future.

1.3 Outline of the thesis

The introduction above only gives a brief discussion of the existing literature. The details can be found in Chapter 2. Following which, the methodology of the fundamental equations and the spatial-temporal distribution of the turbulent viscosity for both single- and multi-phase flow simulation are presented in Chapter 3. In Chapter 4, the methodology of the hybrid method is derived for both single- and multi-phase flow separately. Its implementation details will be given in Chapter 5 with various features of the hybrid model being discussed. Chapter 6 focuses on the validation of the present model by comparing its prediction with experimental and other numerical results available in the public domain; whereas Chapter 7 demonstrates the efficiency of the hybrid model. The thesis is concluded by Chapter 8, together with the discussion on the feasibility of coupling the developed hybrid model with a potential solver and recommendation on future work.

2

LITERATURE REVIEW

This section of the literature review starts with the classical VIV problem studied by both experimental and numerical approaches regarding both the single- and multi-phase flow. Due to the complexity of the VIV study, the movement of the cylinder is usually classified into two types: the free vibration and the forced vibration. Hence, review of the free and forced vibration will be given separately. After that, the numerical simulation models, both the traditional single models and the hybrid models belonged to different categories are compared and reviewed. At last, discussions are given about the existing problems, and the objective of this study is described.

2.1 Experimental researches

2.1.1 Free and forced vibration studies

One important way to predict VIV is to generate a complete experimental database by testing cylinders undergoing free or controlled sinusoidal oscillations in a free stream. Firstly, regarding the free vibration, several investigators including Griffin & Ramberg (1982), Williamson & Roshko (1988), Brika & Laneville (1993, 1995), Khalak & Williamson (1997), Lin & Rockwell (1996), Noca, *et al*. (1999), Govardhan & Williamson (2000) have conducted a series of experimental researches. Among them,

Brika & Laneville (1993, 1995), were the first to show evidence of the *2P* (*P* is short for vortex pairs) vortex wake mode from free vibration and confirmed the earlier explanation by Williamson & Roshko (1988) for the hysteresis loop in terms of a change in wake vortex patterns. Brika & Laneville (1993, 1995) found a clear correspondence of the *2S* mode with the initial branch of response, and the *2P* mode with the lower branch. However, Khalak & Williamson (1997) observed that the phenomena at low mass ratios and low mass damping are distinct from those mentioned above. A direct comparison is made between the response in water by Khalak & Williamson (1997) with the largest-response plot of Feng (1968). The lighter body has a value of mass ratios yielded a much higher peak amplitude. Khalak & Williamson (1997) also observed the existence of three distinct branches, in which the low mass ratio type of response is characterised by not only the initial branch and the lower branch, but also by the new appearance between the other two branches of a much higher upper response branch. Regarding the phenomenon of ‘‘lock-in’’ or synchronization, however, for the low mass ratio in water in the experiment of Khalak & Williamson (1997), the body oscillates at a distinctly higher frequency, is different to the traditional concept in the studies of Blevins (1990) and Sumer & Fredsoe (2006).

Secondly, the forced vibration experiments researches have been carried out by Bishop & Hassan (1964), Sarpkaya (1978), Staubli (1983), Gopalkrishnan (1993), Hover, *et al*. (1997, 1998), Sheridan, *et al*. (1998), Blackburn & Williamson (2001), Carberry *et al*. (2001, 2003, 2004, 2005), Parnaudeau, *et al*.(2008) and Morse & Williamson (2009) etc. They have measured the forces on bodies in harmonic, the multifrequency motion and the wake patterns. Williamson & Roshko (1988), studied the vortex wake patterns for a cylinder that forced to translate in a sinusoidal trajectory. They defined a whole set of different regimes for the vortex wake modes. Each periodic vortex wake pattern comprises single vortices (*S*) and vortex pairs (*P*), giving patterns such as the *2S*, *2P* and *P+S* modes, which are the principal modes near the fundamental lock-in region. The *2P* and *P+S* modes have been found in controlled vibration studies in-line with the flow by Griffin & Ramberg (1974), and Ongoren & Rockwell (1988) as well as transverse to the flow (Zdero *et al*., 1995). The *P+S* mode was also found in Griffin & Ramberg’s (1974) well-known smoke visualizations. The significance of

these modes from controlled vibration is that they provide a map of regimes, within which we observe certain branches of free vibration. One deduction from the Williamson & Roshko's (1988) study was that the jump in the phase of the transverse force in Bishop & Hassan's (1964) classical forced vibration study, and also the jump in phase measured in Feng's (1968) free vibration experiments, were caused by the changeover of mode from the *2S* to the *2P* mode. This has since been confirmed in a number of free-vibration studies like Brika & Laneville (1993), etc. Cheng & Moretti (1991) conducted a series of experiments with a circular cylinder subjected to forced transverse vibration in a uniform cross-flow at Reynolds numbers of 1500 and 1650. Blevlns & Burton (1976) have provided extensive data for the amplitude ratio versus the lift coefficient for a variety of conditions. Hover *et al*. (1997); Hover *et al*. (1998) and Hover *et al*. (2001), Gopalkrishnan *et al*. (1994), developed a novel virtual cable testing apparatus and conducted a series of tests using this faculty. A further significant result has been presented by Bearman *et al*. (2001), who have presented an excellent agreement between in-line response measurements at $Re=10^4$ and $Re=10^5$. There was also good agreement for the limited transverse VIV response data at these Reynolds numbers. Sheridan *et al*. (1998) and Carberry *et al*.(2001, 2003, 2004, 2005) made extensive measurements of force from controlled vibrations of cylinders, providing a number of interesting results and data can be used for numerical validation.

2.1.2 VIV subject to the free surface

Comparing to the deep water VIV problem, the experimental researches of VIV considering the effect of the free surface is much less. Firstly, in terms of the submerged depth/gap ratio effect, a series of researches have been conducted. Miyata *et al*. (1990) found that vortex shedding is suppressed when the submerged depth (*h/D*) is very small, where *h* is the distance from the cylinder to the free surface, *D* is the diameter of the circular cylinder. Sheridan *et al*. (1997) experimentally observed that the near-wake structure for small *h/D* falls under a number of modes which are very different from those of deep water. Carberry (2002) observed three different wake states (Modes I, II, and III) as *h/D* decreases, agreeing with the wake structures previously reported by Sheridan, *et al*. (1997) and Reichl, *et al*. (2005). Mode I wake is essentially a modified

Kármán wake with the amplitude of the fluctuating lift force larger than that for deep water case. The periodic vortex shedding appears to be suppressed and the lift varies little with time in both Modes II and III. The flow over the top of the cylinder remains attached to and separates from the free surface for Modes II and III, respectively. In Mode III, the separated flow forms a jet which can either remain attached to the cylinder or flow downwards obliquely. Saelim (1999) investigated the one-degree-of-freedom (one-DOF) transverse VIV of an elastically mounted rigid horizontal circular cylinder beneath a free surface. The results showed that, for small *h/D*, very large regions of hysteresis occur in the variation of vibration amplitude as a function of reduced velocity. For large values of *h/D*, the vibration frequency is higher than natural structure frequency and lower than the vortex shedding frequency in the lock-in zone; for very small *h/D*, the vibration frequency takes on values close to the vortex shedding frequency, hence much higher than natural structure frequency. Rockwell *et al*. (2003) later presented some typical vortex shedding regimes for $h/D = 0$. Cetiner & Rockwell (2001) experimentally investigated the stream wise oscillations under several combinations of amplitude ratio and frequency ratio. They found that the transverse force is phase-locked to the cylinder motion when $h/D \approx 0$ and such locked-in states are destabilised because of an instantaneous jet-like flow mentioned above when *h/D* is finite. Sheridan *et al*. (1997) conducted experiments using the PIV technique and found that close to a free surface the near-wake structure falls under a number of modes which are very different from those of the deeply submerged cylinder wake. Carberry (2002) observed three different wake states as gap ratios decreases which also found by other experimental (Sheridan *et al*., 1997) and numerical (Reichl *et al*., 2005) studies.

Secondly, for the wave and current combing situations, Moreau & Huang (2010) demonstrated that cross-flow VIV in combined wave and current flow is significantly different from that in current or wave alone. Furthermore, the response is very much dependent upon the velocity ratio between the current and wave particle velocity. In their experiment, the cross-flow vibration of a cylinder in co-linear steady and oscillatory flows is investigated for the inline Keulegan Carpenter number varying from 5 to 27 and for the reduced velocity ranging from 3 to 19. For the collinear steady and oscillatory flow, Low *et al*. (1989) measured the pressure distribution around the

cylinder circumference and integrated it to yield the in-line force. The results were given in terms of drag and inertia coefficients as functions of the *KC* number and the reduced velocity. Yokoi & Kamemoto (1994a) examined the vortex shedding frequency and pattern of an in-line oscillating circular cylinder in uniform flow at rather small *KC* numbers and found that the vortex shedding frequency was synchronised with multiples of the oscillation frequency. The summary of the experimental studies carried out for both free and forced/controlled vibration situation with or without the presence of the free surface are given in Table 2.1.1.

Table 2.1.1 A summary of the experimental studies for VIV problems

VIV without free surface		VIV considering free surface
Free vibration	Forced vibration	
Griffin & Ramberg, (1982). Williamson & Roshko (1988), Brika & Laneville (1993, 1995), Khalak & Williamson (1997), Lin & Rockwell, (1996); Noca *et al*. (1999), Govardhan & Williamson (2000) and Brika & Laneville (1993, 1995)	Bishop & Hassan (1964), Sarpkaya (1978), Staubli (1983) , Gopalkrishnan (1993), Hover *et al*. (1997, 1998), Sheridan, *et al*. (1998), Blackburn and Williamson (2001), Carberry *et al*. (2001, 2003, 2004, 2005), Parnaudeau *et al*.(2008) and Morse & Williamson (2009)	Miyata *et al*. (1990), Sheridan *et al*. (1997), Carberry (2002), Saelim (1999), Reichl *et al*. (2005), Rockwell *et al*. (2003), Moreau & Huang(2010), Yokoi & Kamemoto (1994a) and Low *et al*. (1989)

2.2 Numerical simulations

2.2.1 Single models

Regarding the numerical simulation, Navier-Stokes equations give us the possibility to resolve all the flow physics. Nevertheless, applying the equations to a turbulent flow is a challenging topic that requires extremely fine meshes and time steps and leads to high computational costs. Furthermore, in the real practice, engineers are usually interested in some averaged values and some special physics. Hence, there is no need to

resolve all details. In RANS model, the turbulent flow behaviour is approximated modelled by using the Reynolds-Averaging concept to simplify Navier-Stokes equations. This model provides results for mean quantities with engineering accuracy at moderate cost for a wide range of turbulent flow problems. Therefore, RANS is the most widely used turbulent in the VIV simulations. Guilmineau & Queutey (2004) conducted a simulation adopting the incompressible two-dimensional RANS equations together with a SST k-ω model for a low mass-damping case, where the Reynolds number is in the range 900–15000. The simulations predicted correctly the maximum amplitude. However, fail to match the upper branch found experimentally. Ünal, *et al*. (2010) investigated four turbulent models: Spalart–Allmaras (S–A), Realizable k-ε (RKE), Wilcox k-ω (WKO) and Shear-Stress-Transport k-ω (SST), and found that both WKO and SST models exhibited successful performance producing highly correlated predictions of the main flow characteristics with the experimental data. In order to provide a reliable and useful assessment tool for the engineering design work, Ong *et al*. (2009) conducted a simulation covering the supercritical to upper-transition flow regimes around a 2D smooth circular cylinder.

The model of LES is based on a filtering concept (Leonard, 1975). If a spatial filter $G = G_{\Delta f}$ is applied to a variable ϕ, this yields a smoothed counterpart $\bar{\phi}$ with scales smaller than the filter width Δf being removed. Numerical simulations of VIV using LES are extensive. For instance, Al-Jamal & Dalton (2004) have performed a 2D LES study of the VIV response of a circular cylinder at a Reynolds number of 8000 with a range of damping ratios and natural frequencies. Kim (2014) examined the transition process between two different wake states in the frame of LES for the high Reynolds number flows range from 5500 to 41300. Other simulations include Selvam (1997), Wang & Catalano (2001), Catalano, *et al*.(2003) and Breuer (2000).

Both RANS and LES have its advantages and drawbacks. The LES eddy stress based on a relation between the length scale to a numerical grid and explicitly involves the step size of the computational grid. RANS models, in contrast, only depend on the physical quantities, including geometric features like the wall distance. In the wall regions, it is fair to describe most of the current LES work as Quasi-Direct Numerical Simulation (QDNS) (Spalart *et al*. 1997). The magnitude of the SGS stresses is of the

same order as the viscous stresses, since the typical eddy-viscosity levels are very close to the molecular viscosity. The cost of LES in the entire boundary layer exceeds the computing power by orders of magnitude. As a result, RANS is the only choice for most of the boundary layer. RANS and LES show their advantage in the boundary layer and separation regions, separately. However, regarding the three-dimensional separation, it is beyond the capability of RANS and the LES model is often employed.

DNS is model-free numerical simulations of turbulence. DNS differs from the RANS in that the turbulence is explicitly resolved, rather than modelled by a closure model. It also differs from LES in scales, even the very smallest ones are captured and no need for a subgrid-scale model. Its advantage is the ability to provide complete knowledge, unaffected by approximations within the simulation period (Coleman & Sandberg 2010). This ability, however, comes at a high price and severe limitation on the maximum Reynolds number and complex geometry that can be considered, which prevents DNS from being used as a general-purpose design tool. DNS as a powerful model has been adopted in the VIV simulations as well. Dong & Karniadakis (2005) conducted a DNS simulation for turbulent flows past a stationary circular cylinder and a rigid cylinder undergoing forced harmonic oscillations at *Re* =10000. Comparisons with the available experimental data show that the simulation has captured the flow physical quantities and the statistics of the cylinder wake correctly. Dong *et al*. (2006) investigated the effects of Reynolds number (at *Re*=3900, 4000 and 10000) by combining PIV measurements and DNS simulations. The statistical characteristics of the cylinder wake and on the shear-layer instability in the transitional range are observed altered with the variation of Reynolds number.

Comparing the three models, there are not only differences but similarities. As for RANS modelling, the nonlinear convection term in the transport equation introduces an unclosed term, describing the impact of the sub-filter scales on the resolved motion, it is replaced by a model term τ_{ij}^{LES} in LES. For the efficiency reason, the ratio of the filter width Δf to the step size of the grid Δg is usually set equal to one or a small integer. τ_{ij}^{LES} is usually called sub-grid scale (SGS) model. However, that in most LES, filtering is rather a concept behind the development of the method than an explicitly applied procedure to specify the resolved motion (Fröhlich & Rodi 2002). Hence, in the ultimate

limit $\Delta g \to 0$, the SGS model vanishes so that the simulation turns into a DNS without turbulence model. This structural similarity is also the foundation of the RANS/LES/DNS hybrid method. The comparisons of RANS, LES and DNS models are given in Table 2.2.1.

Table 2.2.1 Comparisons of RANS, LES and DNS models in VIV simulation

	RANS	LES	DNS
Advantage	(1) Engineering accuracy at moderate cost for a wide range of flows. (2) Most affordable solution provided for the boundary layer	(1) Wider range of eddy structure are captured (2) in the separation area.	Most accurate and approach comparing to the experimental results
Drawbacks	(1) Can better handle the standard eddies but eddy structures are highly geometry-specific. (2) Ineffective for flows with significant nonlocal (in space and time) effect.	Very expensive in the wall regions	A high price and severe limitation on the maximum Reynolds number and complex geometry
Connection and similarities	For the LES model, if the filter size $\Delta g \to 0$, then the model becomes to DNS. If the calculation of the eddy viscosity term using a RANS turbulent model, then the LES model turns into a RANS model.		

Recent years have seen the boot of the HPC. With the fast development of the HPC, for one thing, we expect the current turbulent flow simulations can benefit from it, for another the advance in HPC hardware has led to additional challenges for the turbulent model algorithms, such as the need to parallelise numerical schemes efficiently by using a large number of processors (Coleman & Sandberg 2010). These developments will undoubtedly pose new challenges for the maintenance of current codes and the development of new efficient numerical methods.

2.2.2 Single models considering the free surface

Regarding the flow past a circular cylinder, the most studied case is the stationary circular cylinder subject to the inline steady flow. However, fewer considering the influence of the free surface. According to the previous studies, it is generally agreed that the pressure distribution and the near wake structure of the circular cylinder near the free surface are very different to that deeply submerged cylinder situations.

Considering the effect of the submerged depth, Chung (2015) numerically compared the cases of gap ratio= 0.4, 0.8 to deep water situation. The jump of the amplitude and phase of lift was also reported, however not accompanied by considerable changes in vortex shedding timing. The magnitude of the negative time-averaged lift increases with decreasing *h/D*. The cylinder approaching a free surface suppresses occurrence of beating in the temporal variation of lift. Sheridan (1997) investigated the weak behaviours of 2D flow past a cylinder close to a free surface at a *Re* =180. The Froude numbers ranging from 0.03 to 0.7 and gap ratios between 0.1 and 5.0 is examined. His simulations reveal that this problem shares many features in common with flow past a cylinder close to a no-slip wall, and the flow is largely governed by geometrical constraints in the low Froude number. The study of Bozkaya *et al*. (2011) also reported the effects of gap ratio and frequency ratio on the mode, period, and geometry of vortex shedding as well as the lock-in phenomena.

For an oscillatory flow with a fixed cylinder, a great deal of work has been done on the inline hydrodynamic force, in the context of Morison equation, to investigate the drag and added-mass coefficients. However, much less work was done on the cross-flow force, among them, one can find the works by Verley (1982), Bearman *et al*. (1984). The key conclusion is that the lift force has many frequency peaks typically at multiples of the oscillatory flow frequency. Al-Mdallal *et al*. (2007) carried out a numerical investigation on the vortex shedding modes for very low Reynolds number and *KC* numbers.

For the oscillating circular cylinder, the numerical study of Chung (2016a) aimed to understand thoroughly the two-DOF VIV of a low-mass zero-damping circular cylinder near a free surface in the low Reynolds number regime (*Re*=100). For a transversely oscillating circular cylinder, the most important finding by Carberry *et al*. (2004) is the

lift-phase jump at frequency ratio around 0.82 for various gap ratio considered. The vortex shedding appears to be inhibited but not eliminated when the gap ratio decreases. Table 2.2.2 demonstrates the state-of-the-art regarding the multiphase flow past a circular cylinder.

Table 2.2.2 Numerical simulation of flow past circular cylinder considering the free surface

Flow conditions	Steady flow with the free surface	Oscillatory flow	Collinear steady and oscillatory flow
Previous studies	Chung (2015), Sheridan (1997), Bozkaya *et al*. (2011),	Verley (1982), Bearman *et al*. (1984)	Al-Mdallal *et al*. (2007), Yokoi & Kamemoto (1994a), Low *et al*. (1989)

2.2.3 Hybrid models

Besides the traditional single models, continuous efforts have been carried out to couple different models to make the best use of their advantages. The numerical approach that adopts such strategy is usually referred to as a hybrid model. The theoretical hypothesis of the hybrid models is that the viscous/turbulent effects are only significant in a limited area (Li *et al*., 2015; Edmund *et al*., 2013), suggesting that the turbulent viscosity is only confined to a small region such as near the offshore structures or breaking waves, and may be ignored in other areas. In term of the role that played by the viscous effects in the hydrodynamic problems, researchers have investigated the interactions between inviscid and viscous flows since Prandtl's boundary layer theory in the early 1900s. Prandtl (1904) assumed viscous effects are confined to a thin layer and derived the boundary layer theory. After that, the attempt of improving the potential velocity solution is to include the influence of the viscous boundary layer. For example, Lighthill (1958) proposed four alternative treatments of the displacement thickness for two-and three-dimensional flows. Other viscous–inviscid interactions studies intended to use a potential solver separately either by using potential solutions as initial conditions or by matching potential solutions to the viscous solutions in separate regions, e.g., Stern, *et al*. (1988), Chen, *et al*.(1996) and Chen, *et al*. (1999). However, the

displacement thickness is sensitive to small velocity changes in the outer parts of the viscous layer and does not has the capability to deal with the flow separation.

The terminologies for the developed hybrid methods varied in different publications. In this thesis, based on the nature of the various hybrid models, they can be classified into two broad categories: (1) the first one is the coupling of RANS model with more computationally efficient and therefore simplified solver, e.g., Euler or potential model. This method is aimed to handle the multi-properties flow, like propagation of wave and the fluid-structure interaction issues, in a less computationally expensive way. This method is referred as simplified /RANS hybrid method in this thesis. (2) The second category is the coupling of RANS with higher fidelity models like LES and DNS models. This method mainly focuses on the turbulent flow only and requires at least a RANS solver. In this thesis, the methods belong to this category are referred as RANS/LES/DNS hybrid method.

2.2.3.1 Simplified /RANS hybrid models

Within the regime of the simplified/RANS hybrid method, it can be further divided into two categories: (1) the velocity/function decomposition approach that splits either the velocity or the model/function and (2) the domain/zonal decomposition approach, which conducted in the spatial point of view.

For the functional decomposition method, a simplified model covers the entire computational domain, and a complementary RANS model is solved in a subdomain with significant viscous effects to correct the solution of the simplified models. Inside this subdomain, the desired solutions are obtained by summing up the solution of the simplified model and that of the complementary RANS model. Ferrant *et al*. (2003) and Luquet *et al*. (2007) presented a Spectral Wave Explicit Navier-Stokes Equations (SWENSE) approach. They used a potential flow theory to calculate the incident wave field while RANS model is employed to solve the diffracted flow allowing the inclusion of viscous effects. They had successfully employed this method to model waves interacting with a tension-leg platform and ship body in regular or irregular waves by coupling the Fully Nonlinear Potential Theory (FNPT) based on the Higher-Order Spectrum (HOS) method and RANS solver based on the VOF method. The way of

dividing the total velocity is not unique, Hafez *et al*. (2006) proposed a Helmholtz-type velocity decomposition technique to simulate the two-dimensional steady laminar incompressible flows. The potential function is used to represent the near and far velocity fields and the pressure is computed using the Bernoulli's law. The rotational velocity components within the viscous flow regions are calculated by the integration of the momentum equations. Hafez *et al*. (2009), extended their approaches to the unsteady laminar flow cases where the gradient of the potential is augmented with a correction accounting for the vorticity effects in the modified viscous layers. Helmholtz decomposition is also applied by Kim *et al*. (2005). A complementary set of RANS was developed for the steady incompressible turbulent flow, in which the hybrid solver in the coarse grid shows a solution as good as or even better than that corresponding to the original solver in the medium grid with a CPU time that is more than ten times less. Edmund (2012), Kim (2004) and Rosemurgy *et al*. (2012) apply a similar approach as Kim, but they did not solve the decomposed equations. An improvement was made by including the viscous effects in the potential flow with the viscous potential velocity acting as the inlet and far-field boundary conditions for the total fluid velocity. This allows the computational domain to be reduced to just beyond the vortical region. In the steady flow research done by Edmund (2012) and Edmund *et al*. (2013), the accuracy is retained and the computation time was reduced between 3% and 68%.

The main idea of the domain decomposition within the regime of Simplified /RANS hybrid method is that divides the computational domain by either a prior interface or an automatic interface. The local physics, such as wave breaking and vorticity are located within the subdomain governed by RANS model. The solution of the potential model provides the boundary condition for the NS model. Lynett & Coastal (2010) developed a Potential-NS model coupling the higher order Boussinesq equation with RANS equation, for simulating wave propagating from deep water to shoreline, involving the breaking waves. Narayanaswamy *et al*. (2010) also suggested a Potential-NS model coupling the higher order Boussinesq equation with the SPH method to study the coastal waves that could take accounts of the breaking effects. Clauss *et al*.(2016) studied the wave-structure interaction through coupling the Fully Nonlinear Potential Theory (short as FNPT) solver based on Finite Element Method (FEM) and NS solver based on VOF

method. Sriram *et al*. (2014) have developed a novel algorithm to couple the FNPT solver based on the Quasi-Arbitrary-Lagrangian-Eulerian Finite Element Method (QALE-FEM) and NS solver based on the improved Meshless Local Petrov Galerkin method with Rankine source solution (IMLPG_R) to study the breaking waves.

2.2.3.2 RANS/LES/DNS hybrid models

RANS/LES/DNS hybrid method is designed to deal with the turbulent problems only in the way of intermediate cost and degree of accuracy with respect to the traditional single models (Girimaji & Abdol-Hamid 2005). Most of the modification and trials are focused on RANS and LES combination since the shared structural similarity with respect to the transport equations and turbulent models. Researches regarding RANS/LES/DNS hybrid method including two different attempts: (1) the first one is the decomposition method that divides either the model or function and (2) the second one is related to the domain/zonal decomposition with an interface.

The approach Partially Filtered Navier-Stokes (PANS) developed by Girimaji & Abdol-Hamid (2005) belongs to the first type. It contains a term defining the ratio between resolved and modelled fluctuations (Menter *et al*., 2003) and is prescribed prior to a given simulation. The resolution of the flow is controlled by suitably specifying the unresolved kinetic energy parameter. Various modelled-to-resolved scale ratios ranging from RANS to DNS can be conducted by this method.

Most of the studies fall into the second type that adopts the domain decomposition approach. The comparison of two decomposition approaches is described in Table 2.2.3. The strategy is to employ the LES model and RANS model in different zones so that a boundary between different zones can be specified at each instant in time. Quéméré *et al*. (2001) and Quéméré & Sagaut (2002) proposed a multi-domain/multi-resolution decomposition approach. The proposed treatment is based on the definition of an interface variable, which is extrapolated from the LES subdomain or extracted from an auxiliary computation, depending on the type of interface. In the study of Quéméré *et al.* (2001), the memory requirement is reduced, and the CPU cost is about 37% and 46% for mesh ratio at the interface equal to two and four respectively when using coarser grids in the core of the channel. There is five times less CPU time demanded and good

agreement between mono-domain and multi-domain results. An investigation of a unified RANS–LES model regarding computational development, accuracy and cost are conducted by Gopalan *et al*. (2013). The Linear Unified Model (LUM) is compared to LES, the advantage of the LUM is a cost reduction of high-Reynolds number simulations by a factor of $0.07Re^{0.46}$.

It is important to note that there are models different to the zonal model like the segregated models, the transition of variables between different subdomains without discontinuity since only a source term in the auxiliary equation changes smoothly, e.g., Spalart, *et al*. (1997) and Spalart (2000) developed the model of Detached Eddy Simulation (DES) which offers RANS in the boundary layers and LES after massive separation. Eddies internal to the boundary layer are treated as attached eddies. Combining of the DES with different turbulence models are discussed separately with and in S-A (DES-SA) (Spalart *et al*. 1997) and SST model (DES-SST) (Menter 1994). Besides the above unified mesh strategy, a dual-mesh framework is applied by Xiao & Jenny (2012), in which both of the two meshes covering the whole domain. The consistency between the LES and RANS solutions is enforced via drift terms in the corresponding equations.

Table 2.2.3 Comparison of two decomposition approaches

	Domain decomposition	Functional/velocity/model decomposition
Advantage	Straightforward methodology	Easy implementation for the two solvers sharing the same structure of the governing equation
Drawbacks/ limitation	Either artificial transition zone need or additional iterations procedure required to make the consistent of coupled solvers	Special treatment of the coupling boundary needed

2.3 Discussions

Comparing the two types of movement of the cylinder, we can see, in the forced oscillations, the imposed amplitude and frequency drive the oscillation, while the free

oscillations are driven by the past and the prevailing state of the motion and the forces arising from it. The prediction of the structure responding to free vibration is very challenging. The shedding depends on a significant number of independent parameters. The relationship between these parameters (e.g., virtual mass, forces and body acceleration) is non-linear and not yet fully understood (Vecchi 2009). While in the forced vibration, the amplitude and the frequency of motion can be varied independently. Therefore, a useful approach to understand and eventually predict such complex problem is represented by forced vibrations simulations. Despite these differences, if the sinusoidal forced oscillation accurately represents the vortex-induced motion of the cylinder then the wakes for the two cases should be the same (Carberry *et al*. 2005). According to the above review, the study of the forced vibration can provide more insights into the interactions between the vortex mode and the cylinder movement (Kim 2014). Furthermore, forced oscillation experiments represent an idealisation of most features of VIV problems. The forced oscillation conducted so far show encouraging agreement with data from free cases (Sarpkaya 2003). Furthermore, the study presented in this thesis is mainly focused on the hydrodynamic characteristic of VIV which can be revealed by the forced oscillation of the structure. Thus, the forced vibration is applied in this research.

Based on above literature review of the previous research work, it is understandable that: (1) lots of achievement have been obtained by the experimental researches, which is a very important tool for the study of VIV problem. However, it has the drawback of high cost, low flexibility, facilities and cases dependent, etc. (2) Regarding the numerical studies, the researches focus on wave-current cylinder interaction are not sufficient. Further investigation should be carried out considering the effect of the free surface on the cylinder trajectories, hydrodynamic force coefficients, and vortex structures. (3) Furthermore, the current models are generally low efficient because of the high requirement of mesh, large computational domain and solving the additional turbulent model equations.

2.4 Existing problems, objectives and main contribution

It should be noted that VIV simulation is one of the applications of the hybrid model proposed in this thesis. This hybrid solver is capable of dealing with other turbulent related problems. Furthermore, it should be able to extend to a multiphase solver aimed at the free surface related issues. Comparing to the second broad category (RANS/LES/DNS hybrid method) in the above review which is characterised by computationally expensive and aimed at the turbulent flow only, the first type (simplified /RANS hybrid method) is more suitable to be employed in this study. Based on the literature review, despite their success, there are still problems related to the existing methods. To be more specific, there are three aspects need to be improved.

(1) The developed model should not be limited to the steady turbulent flow (Edmund *et al*., 2013; Ferrant *et al*., 2007) and laminar flow (Monroy & Ducrozet 2009). The hybrid method proposed is intended to deal with the unsteady turbulent flow, especially for the complex moving wall-bounded cases. Besides, in contrast to the DES-SA model (Spalart *et al*., 1997) or DES-SST model (Menter *et al*., 2003), it should not be limited by to a specific turbulent model but could work with variant turbulent models.

(2) Unlike the one-way coupling strategy, i.e., the viscous flow does not influence the potential flow in the previous research such as SWENSE method (Ducrozet *et al*., 2011; Monroy & Ducrozet 2009; Luquet *et al*., 2007), a two-way transformation technique is developed. This technique is used to bridge the gap of turbulent viscosity between the two coupled solvers. The viscous effect is involved in the simplified solver during the transformation of the variables, which can ensure the smooth transition between the two solvers and robustness of the model. Another benefit from the transformation technique is that a truncated domain can be applied, which can eventually lead to the computational time-saving. The size of the subdomain with remarkable viscous/turbulent effects is critical to obtain reliable results and is generally determined by comparing the results using different sizes with the experimental data for specific problems. One may agree that the size of the subdomain shall be closely related to the spatial variation of the turbulent viscosity or the vorticity. Nevertheless, a systematic investigation of the features of spatial variation of turbulent viscosity is

rarely found in the public domain. In this thesis, the studies of the subdomain size based on the investigation of the turbulent viscosity properties will be given.

(3) Although all the existing hybrid models are claimed to be efficient, only a few researches (Edmund *et al*., 2013, Kim, *et al*., 2005) have reported the details of the efficiency increase such as CPU time-saving. In this hybrid method, a sub-cycle strategy aimed at efficiency improvement is proposed. The sub-cycle technique is based on the difference between the mesh scale and time step for the simplified solver and the complex turbulent solver. The efficiency of the hybrid method can be boosted by both the spatial domain truncation and temporal sub-cycle. The comparison of the hybrid method and original solver efficiency will be demonstrated in various working conditions in this thesis.

In summary, the hybrid method of this thesis is intended for complex flows that many single models are likely to be invalid. The main purpose of this hybrid method is to improve the performance of the current single model while overcoming some drawbacks of the existing hybrid models. The theoretical hypothesis of the hybrid method is following the assumption that the turbulent viscosity effects are only confined to a limited region. This hypothesis is based on the investigation of the turbulent viscosity that given in Chapter 3. In response to (1), a hybrid numerical method aimed to deal with the unsteady turbulent flow is developed. In this work, RANS model is selected to coupling with the simplified solver under the consideration of numerically affordable. The algorithm allows the hybrid method to work with different turbulent models for the specific flow problems. Due to this study is confined to flow past a circular cylinder, investigations are carried out for which turbulent model is better by comparing the solutions from the different turbulent models(k-ε or k-ω SST model) with the experimental data and other numerical results (see Chapter 3.4). To resolve (2) and (3), as a distinguished feature, a two-way transformation strategy and sub-cycle technique are proposed. By doing so, the efficiency of the simulation using the hybrid method is substantially increased.

In this study, the computational fluid dynamics package OpenFOAM (Greenshields 2017) is used to implement this hybrid methodology. As an open source solver, OpenFOAM is gaining popularity in CFD research community. It is a powerful field

manipulation tool offering the access to versatile libraries and utilities, as well as the user-friendly customizable solvers (Weller & Tabor 1998). Furthermore, the object-oriented techniques of C++ allow the codes to closely resemble its mathematical counterpart and makes the top-level syntax amenable to development and modification (Greenshields 2015). All these features of OpenFOAM make it a suitable platform for the implementation of the techniques involved in the hybrid method.

3

CONVENTIONAL MODELS AND PRELIMINARY INVESTIGATIONS

This chapter summarises the conventional model for studying unsteady flow around a structure, including the governing equation and relevant model to deal with the turbulent flow. The classic RANS model, which is derived by the ensemble averaging method in the spatial-temporal domain, is selected. The fluctuating of the velocity, which is the nature of the turbulent flow, is reflected by the Reynolds stresses in the momentum equation based on the Boussinesq turbulent-viscosity hypotheses. The main focus of this chapter is the preliminary investigation on the spatial-temporal distribution of the turbulent viscosity, to which the Reynolds stress is proportional. This investigation leads to the hypothesis of the present research and forms the basis of the functional decomposition (velocity decomposition) hybrid model development. As indicated in Chapter 1, only 2D problem is considered in this research.

3.1 Fundamental equations of conventional model

The fundamental basis of the fluid dynamics are the Navier-Stokes equations and the continuity equation. Considering an incompressible Newtonian fluid, the momentum and continuity equations are described, respectively, as

$$\frac{\partial u_i}{\partial t} + \overline{u_j}\frac{\partial u_i}{\partial x_j} = -\frac{1}{\rho}\frac{\partial p}{\partial x_i} + \nu\frac{\partial u_i}{\partial x_j \partial x_j} \qquad (i = 1,2) \text{ (3.1.1)}$$

and

$$\frac{\partial u_j}{\partial x_j} = 0 \qquad \text{(3.1.2)}$$

where x is the Cartesian coordinate, u is the velocity, t is the time, p is the pressure, ρ is the density, ν is the dynamic viscosity. Subscripts i and j are summation indexes, which represent relevant Cartesian components. They equal to 1 and 2 for 2D problems (1, 2 and 3 for 3D problems). Here and throughout this thesis, whenever the same index appears twice in any term, a summation over the range of that index is implied.

In the RANS model, the ensemble averaging method is generally used for the unsteady turbulent flow. The concept of this method is to imagine a set of flows in which all variables that can be controlled are identical, but the initial conditions are generated randomly. All unsteadiness in the flow is ensemble averaged out and regarded as part of the turbulence. The flow variables, in this example one component of the velocity, are represented as the sum of two terms:

$$u_i(x_i, t) = \overline{u_i}(x_i) + u_i'(x_i, t) \qquad (i = 1,2) \text{ (3.1.3)}$$

where the symbols ($' - '$) and the ($' \; ' '$) represent the average and the fluctuating values, respectively.

Considering a series of measurement with the number of N_t identical experiments, the mathematical form can be written as

$$\overline{u_i}(x_i, t) = \frac{1}{N_t}\sum_{n=1}^{N_t} u_{ni}(x_i, t) \qquad (i = 1,2) \text{ (3.1.4)}$$

where N_t is the total number of independent samples, $u_{ni}(x_i, t)$ is $u(x_i, t)$ measured at the n^{th} series. The term Reynolds averaging refers to any of the processes above. Applying it to the incompressible continuity equation gives

$$\frac{\partial \overline{u_j}}{\partial x_j} = 0 \qquad (i = 1,2)\ (3.1.5)$$

Substituting Equation (3.1.3) to the incompressible momentum equation, it results in the RANS equation

$$\frac{\partial \overline{u_i}}{\partial t} + \overline{u_j}\frac{\partial \overline{u_i}}{\partial x_j} = -\frac{1}{\rho}\frac{\partial \bar{P}}{\partial x_i} + \nu\frac{\partial \overline{u_i}}{\partial x_j \partial x_j} - \frac{\partial \overline{u_i' u_j'}}{\partial x_j} \qquad (i = 1,2)(3.1.6)$$

which can be rearranged as

$$\left(\frac{\partial \overline{u_i}}{\partial t} + \overline{u_j}\frac{\partial \overline{u_i}}{\partial x_j}\right) = \frac{\partial}{\partial x_j}\left[-\frac{1}{\rho}\bar{P}\delta_{ij} + \nu\left(\frac{\partial \overline{u_i}}{\partial x_j} + \frac{\partial \overline{u_j}}{\partial x_i}\right) - \overline{u_i' u_j'}\right] \qquad (i = 1,2)(3.1.7)$$

In the right-hand side, there are three stress terms: $-\frac{1}{\rho}\bar{P}\delta_{ij}$is the mean pressure field, δ_{ij} is the Kronecker delta ($\delta_{ij} = 1$ if *i=j* and $\delta_{ij} = 0$ if $i \neq j$), $\nu\left(\frac{\partial \overline{u_i}}{\partial x_j} + \frac{\partial \overline{u_j}}{\partial x_i}\right)$ is the viscous stress from the momentum transfer at molecular level, $\overline{u_i' u_j'}$ is the Reynolds stresses arising from the fluctuating velocity field.

Because of the symmetry of the Reynolds stress tensor $\overline{u_i' u_j'}$, there are six independent elements of the tensor and therefore six more unknowns for 3D problems (three for 2D problems). Therefore, the system consisting of the continuity and momentum equations is not closed (under-determined). To close the system, i.e. get the same number of equations as the unknowns, one must provide extra equations to model the Reynolds stresses in some way. In the Newton's law of viscosity, the viscous stress is taken to be proportional to the velocity gradient. For the incompressible fluid, this gives

$$\tau_{ij} = \mu s_{ij} = \mu\left(\frac{\partial \overline{u_i}}{\partial x_j} + \frac{\partial \overline{u_j}}{\partial x_i}\right) \qquad (i = 1,2)(3.1.8)$$

where $\mu = \nu\rho$ is the dynamic viscosity of the flow. In this stress tensor matrix, the diagonal components are the normal stresses, and the off-diagonal components are the shear stresses. The turbulent kinetic energy, *k* is the half trace of the Reynolds stress tensor.

$$k = \frac{1}{2}\rho\overline{u_i' u_i'} \qquad (i = 1,2)(3.1.9)$$

The isotropic stress is defined as $\frac{3}{2}k\delta_{ij}$. Then the deviatoric part is

$$a_{ij} = \overline{u_i' u_j'} - \frac{3}{2} k \delta_{ij} \qquad (i = 1,2) \text{(3.1.10)}$$

It is observed that the turbulent stresses increase as the mean rate of deformation increase. Analogy to the stress-strain relation for a Newtonian fluid, i.e. Equation (3.1.8), Boussinesy introduced the turbulent-viscosity hypotheses in 1877. According to the hypotheses, the turbulent stress can be found by

$$\tau_{ij} = -\overline{u_i' u_j'} = \nu_T \left(\frac{\partial \overline{u}_i}{\partial x_j} + \frac{\partial \overline{u}_j}{\partial x_i}\right) - \frac{3}{2} k \delta_{ij} \qquad (i = 1,2) \text{(3.1.11)}$$

where the scalar field $\nu_T = \nu_T(x_i, t)$ is called the turbulent or eddy viscosity. This hypothesis introduces the macroscopic representations of the micro-scale fluctuating flow. It gives the possibility to model the overall effects of small vortexes by correlations and, therefore, resolve the larger eddies in the numerical simulation. This dramatically reduce the CPU time, compared to the DNS, where the fluctuating flow and the small eddies are modelled directly.

Submitting Equation (3.1.11) into Equation (3.1.7), it leads to

$$\frac{\partial \overline{u}_i}{\partial t} + \overline{u}_j \frac{\partial \overline{u}_i}{\partial x_j} = \frac{\partial}{\partial x_j}\left[\nu_{eff}\left(\frac{\partial \overline{u}_i}{\partial x_j} + \frac{\partial \overline{u}_j}{\partial x_i}\right)\right] - \frac{1}{\rho}\frac{\partial}{\partial x_j}\left(\bar{P} + \frac{2}{3}\rho k\right) \qquad (i = 1,2) \text{(3.1.12)}$$

in which the effective viscosity $\nu_{eff}(x_i, t)$ consists of two components, including a constant molecular viscosity ν and a spatial-temporal dependent turbulent/eddy viscosity $\nu_T(x_i, t)$, i.e.

$$\nu_{eff}(x_i, t) = \nu + \nu_T(x_i, t) \qquad (i = 1,2) \text{ (3.1.13)}$$

Further details of the treatment of viscous stress tensor can be found in Appendix A.

3.2 RANS in Arbitrary Lagrangian-Eulerian form

The above equations are usually solved using fixed Eulerian grid/mesh. Nevertheless, if a moving structure is involved, the computational mesh may need to move to conform to the motion of the structure, unless additional treatment is introduced, e.g. considering the structure as an additional phase in the modelling system and applying so-called immersed boundary method. In this study, the structure is not included in the computational domain and the FSI is realised by a partitioned way, in which the fluid

domain and the computational mesh are updated following the motion of the structure and non-slip boundary condition is applied on the structure surface boundary; the motion of the structure is then modelled by Newton's 2nd law in which the force due to the fluid on the structure is obtained by the pressure/stress on the structure surface boundary modelled by above equations; these two models are coupled in an iterative manner. This means that the above equation needs to be solved by using a computational grid/mesh which is neither fixed (Eulerian view) or following the fluid velocity. For this reason, one needs to write the above equations to an Arbitrary Lagrangian–Eulerian (ALE) form, i.e.

$$\frac{\partial u_{Tj}}{\partial x_j} = 0 \tag{3.2.1}$$

$$\frac{\partial u_{Ti}}{\partial t} + \left(u_{Tj} - u_{bj}\right)\frac{\partial u_{Ti}}{\partial x_j} = \frac{\partial}{\partial x_j}\left[v_{eff}\left(\frac{\partial u_{Ti}}{\partial x_j} + \frac{\partial u_{Tj}}{\partial x_i}\right)\right] - \frac{1}{\rho}\frac{\partial p_T}{\partial x_i} \quad (i = 1,2) \tag{3.2.2}$$

$$v_{eff}(x_i, t) = \nu + \nu_T(x_i, t) \qquad (i = 1,2) \tag{3.2.3}$$

where u_T and p_T are the ensemble averaged flow velocity and pressure. For clarity, the over-bar ($' - '$) representing the ensemble averaged value is omitted here and the rest of the thesis.

Considering the movement of the mesh when the flow subjected to the motion of the structure, an additional term, related to the nodal velocity, u_{bj}, is introduced in the convective term to accommodate the movement of meshes. If the computational grid/mesh is fixed, i.e. $u_b = 0$, Equation (3.2.2) become the corresponding Eulerian form, i.e. Equation (3.1.12); whereas if the nodal velocity equals to the fluid velocity, i.e. $u_{bj} = u_{Tj}$, Equation (3.2.2) is identical to the corresponding Lagrangian form. More details of the dynamic mesh can be found in Appendix B.

3.3 Validation of the original solver in OpenFOAM

Before conducting further investigation, the reliability and the accuracy of the numerical prediction from the solvers in OpenFOAM should be investigated at prior. These are carried out by using the cases with a circular cylinder being subjected to uniform current using the OpenFOAM solvers. The drag coefficient and Strouhal number predicted by the OpenFOAM solver are compared with experimental data,

including those by Wieselsberger (1923) for $40<Re<5\times10^5$ and Schewe (1983) for $Re>10^5$, and corresponding numerical results by Stringer *et al*. (2014).

It shall be pointed out that, in order to numerically simulate the turbulent flow problems by using two sets of governing equations, an appropriate turbulent model for evaluating the turbulent viscosity is required. However, it has been revealed by many researchers that different turbulent models give a considerably different prediction of the hydrodynamic parameters, e.g. the drag/lift forces and vortex shedding frequencies (reflected by the Strouhal number). Thus, two classic turbulent models, i.e. k-ε and k-ω SST turbulent models, are employed to assess the suitability of the turbulent model for the problems concerned in this work.

3.3.1 Convergence tests

It is well-known that all CFD work is highly dependent on the mesh resolution. Therefore, the convergence test against mesh resolution is performed at prior. The computational mesh is generated by using the OpenFOAM internal utility. A rectangular computational domain is used in the numerical simulation. The length and the width of the computational domain are *60D* ($D_{in}+D_{out}$) and *40D* (D_c) respectively, where D is the diameter of the cylinder. The circular cylinder is located in the central longitudinal axis. The distance between its centre and the upstream boundary of the computational domain (D_{in}) is *20D* (see Figure 3.3.1). This domain configuration is the same as that used by Stringer *et al*. (2014). The boundary conditions applied at the left end (upstream) and right end (downstream) are the velocity inlet and the pressure outlet, respectively. On the top and bottom boundaries, the slip condition is applied.

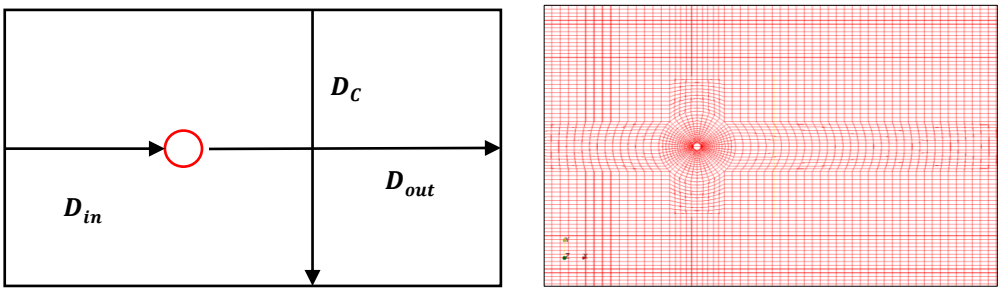

Figure 3.3.1 Sketch of the domain size and mesh block configuration

In the turbulent flow simulation, one of the biggest challenges is to deal with the wall treatment. There are generally two ways, i.e., the low-Reynolds-number (LR) models and high-Reynolds-number (HR) models. The Reynolds number here is for the local Reynolds rather than the global one, e.g., because of the low turbulent Reynolds number in the sublayer, models that resolve the sublayer are called low-Reynolds-number (LR) models. Regarding the LR models, the alternative to wall functions is to use a fine-grid analysis in which computations are extended through the viscosity-affected sublayer close enough to the wall to allow laminar flow boundary conditions to be applied. The LR approach is to capture through all the viscous effects region. Numerically, the LR approach is stiff but time-consuming. In order to reach the viscous sublayer, the first cell centre to body surface normalized distance (y^+) is supposed to be around 1, where $y^+ = (u_* y_w / v_{eff})$. After that, the distance from the centre of the first cell to the wall (y_w) can be determined, where u_* is the friction velocity in the first cell connected to the wall and v_{eff} is the local kinematic viscosity of the fluid. The proper y^+ can be obtained and improved through several trials. However, the HR models use the log law to estimate gradient in the cell, which exhibits high convergence and numerical stability with a much larger y^+ around 30. It should be noted that none of the current approaches can deal with buffer layer where both viscous and Reynolds stresses are significant. As a result, the first computational cell should be either in viscous sublayer or log-layer but not in-between (Utyuzhnikov, 2005). Based on the tests using both of the two approaches, the Low-Reynolds-number (LR) treatment provides more stable and reliable results for the studies cases. In the preliminary study, the convergence tests are carried out for all the studied cases. However, only the case of flow past oscillating circular cylinder with *Re*=1000 is presented here for demonstration. More details of different wall treatments can be found in Appendix C.

Table 3.3.1 Meshes and Courant number tested

Re=1000	Cell number	*Co*
M1	197400	0.1/0.5
M2	355840	0.1/0.2
M3	442288	0.1/0.2

Different sets of meshes are examined to figure out the most suitable mesh under the specific Reynolds number. The results are presented for three successively coarsened meshes, and they are referred to as *M1*, *M2* and *M3* with *M3* being the finest one. A multi-block grid system is adopted in this study, in which the mesh is clustered in the boundary layer, wake region. The sketch of mesh can be seen in Figure 3.3.1.The time step size Δt is automatically determined by using the Courant number *Co* (*Co*=($u\Delta x$)/Δt, where Δx is the mesh size). Two successively time discretization *Co1*=0.1 and *Co2* =0.2 are examined for *M1*, *M2* and *M3*, although these values may be too conservative.

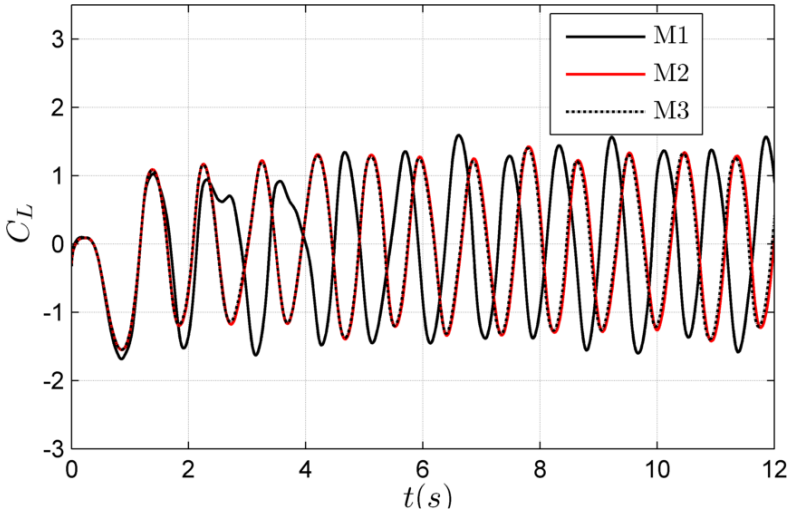

Figure 3.3.2 Lift coefficient variation with three meshes

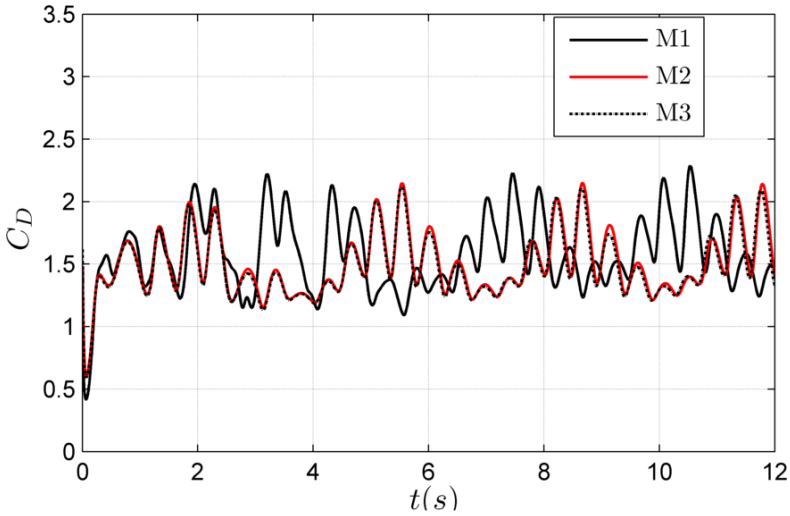

Figure 3.3.3 Drag coefficient variation with three meshes

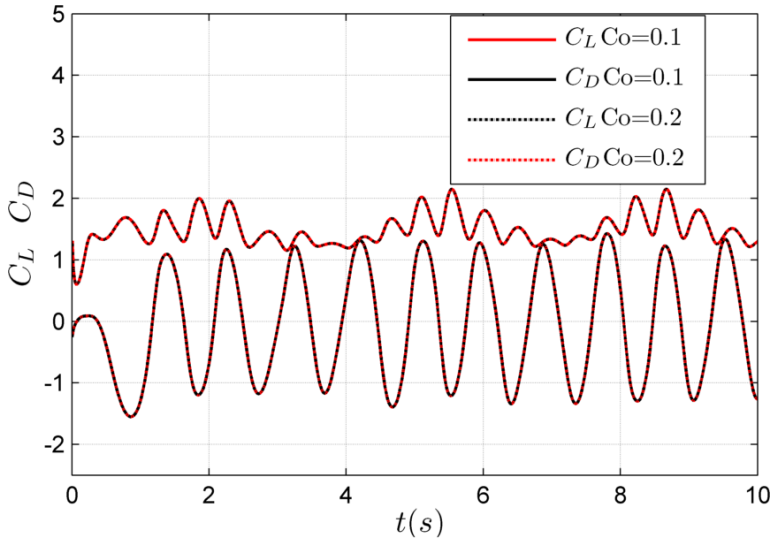

Figure 3.3.4 Converged *M2* with different Courant numbers

The main parameters compared are the drag (C_D) and lift coefficients (C_L), which are defined below,

$$C_D = \frac{1}{2}\frac{F_D}{\rho u^2 A'} \tag{3.3.1}$$

$$C_L = \frac{1}{2}\frac{F_L}{\rho u^2 A'} \tag{3.3.2}$$

where F_D and F_L are the drag force and the lift force respectively, F_D is the force component in the direction of the flow velocity, F_L is the force component in the cross-flow direction, ρ is the density of the fluid, u is the flow velocity, A' is the cross-sectional area.

Results for this case are shown in Figure 3.3.2 to Figure 3.3.4. It is found that the results obtained by using *M1* and *M2* are different, but *M2* and *M3* result in similar results for both C_D and C_L. This does not only demonstrate a good convergent property of the OpenFOAM solver but also demonstrates that *M2* is sufficient for obtaining the convergent solution. Thus then comparison for different *Co* with *M2* is carried out. As observed, *Co* = 0.1 and *Co* = 0.2 give almost identical results. Consequently, *M2* with *Co*=0.2 are applied for this specific working condition. In the further simulation, same convergence tests are conducted for different working conditions.

3.3.2 Validation analysis

After the convergence tests, in this section, it is the validation of the solver within the framework of OpenFOAM. It is well understood that for low *Re* (e.g. 40), the flow is laminar and can be numerically simulated using a steady model. The vorticity in such case is symmetrical about the central longitudinal axis of the cylinder as demonstrated by Stringer et al. (2014). When *Re*>40, the wake becomes unstable, which eventually leads to a vortex shedding alternately occurring on either side of the cylinder at a certain frequency, resulting in the oscillation of the drag coefficient and unsymmetrical/oscillating distribution of the turbulent viscosity as results are shown in Figure 3.3.5 for demonstration. In such case, the key parameters are the mean drag coefficient C_D and the Strouhal number $S_t = f_s U/D$.

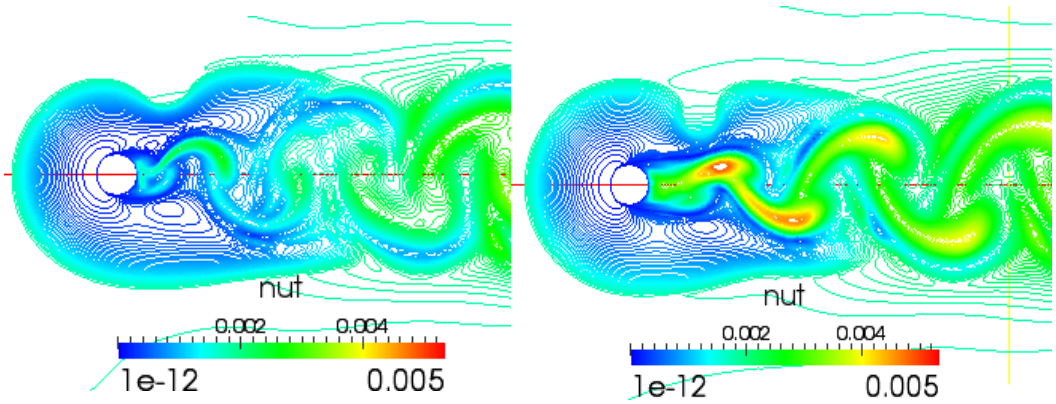

(a) k-ε model (b) k-ω SST

Figure 3.3.5 Distribution of the turbulent viscosity around the cylinder using (a) k-ε model and (b) k-ω SST with *Re* = 10^3

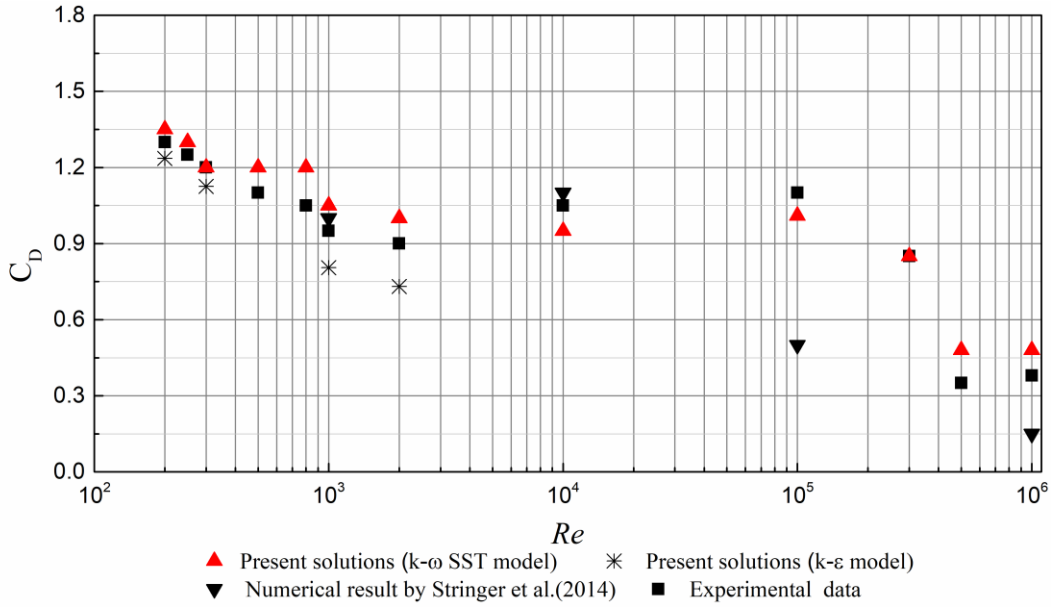

Figure 3.3.6 Comparison of mean drag coefficient as the function of *Re*

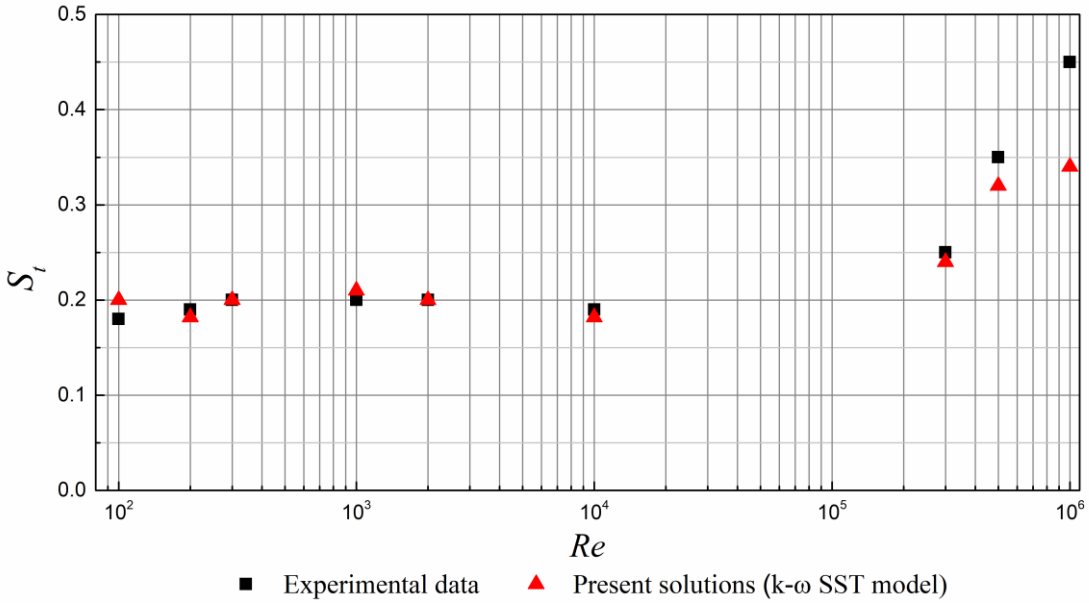

Figure 3.3.7 Comparison of Strouhal number as the function of *Re*

The comparisons of C_D and *St* are displayed in Figure 3.3.6 and Figure 3.3.7, respectively. From Figure 3.3.6, it is found that C_D predicted by the present method with k-ω SST turbulent model generally agrees well with the experimental data, the maximum relative difference is around 13% at $Re>5\times10^5$. It should be pointed out that Stringer *et al*. (2014) used the OpenFOAM with k-ω SST turbulent model to predict C_D

for *Re* within the same range but gave substantially different results as shown in Figure 3.3.6. Especially at $Re = 10^5$ where the vortex shedding is not observed in Stringer *et al*. (2014) but is found in the present study with k-ω SST turbulent model. One may also observe from that the Strouhal number predicted using the present method with k-ω SST turbulent model fairly agree with the experimental data in a large range of *Re* (see Figure 3.3.7). This implies that the present method with k-ω SST turbulent model can produce satisfactory results for analysing the feature of the turbulent viscosity and vorticity. From Figure 3.3.6, one may also notice that the present method with k-ε model seems to considerable underestimate C_D when $Re<=2000$. As indicated in the introduction, the success of RANS on modelling the turbulent flow largely relying on the reliability of the turbulent model on estimating the turbulent viscosity. For the presence of adverse pressure gradient, the performance of the k-ω SST is better than that of k-ε model. The turbulent viscosities demonstrated in in Figure 3.3.5 are those at the same time instant when the vortex is fully developed. It shall be noted that, for the same velocity field, the difference in the turbulent viscosity predicted by using the k-ε model and k-ω SST model may be insignificant; but such small difference may be accumulated in time during the development of the vortex.

The investigation shown above may conclude that the OpenFOAM solver using conventional RANS approach with, k-ω SST can produce satisfactory predictions, which is fairly close to the experimental data within a large range of *Re*. One may agree that the turbulent/eddy viscosity obtained using k-ω SST can satisfactorily reflect the macroscopic representation of the turbulent/flocculating flow field. This will be used in the following sections. As demonstrated in Figure 3.3.5, the turbulent viscosity is only significant in the local area near the cylinder. This means that one can use the RANS without considering the turbulent viscosity (thus without the need of applying the turbulent model to predict the turbulent viscosity) in the area far away from the structures; only in a region near the structure, the turbulent model is necessary. This justifies the hypothesis of the present work on developing the hybrid model, which will be presented in Chapter 4. Systematic investigations will be carried out to analyse the spatial variation of the turbulent viscosity in the cases with single- and two-phase flow,

and, more importantly, to determine a critical zone in which the turbulent viscosity plays an important role.

3.4 Feature of the turbulent viscosity in single phase flow

3.4.1 Turbulent viscosity with a stationary circular cylinder

For the stationary circular, the contour lines of vorticity and turbulent viscosity for the cases with Re=200 and Re=10^6 are given from Figure 3.4.1 to Figure 3.4.4, in addition to the results with Re=1000 (see above Figure 3.3.5(b)). Regarding regimes of flow around circular cylinder, for very small values of Re no separation occurs. The separation first appears when Re becomes 5 and the boundary layer over the cylinder surface will separate due to the adverse pressure gradient imposed by the divergent geometry of the flow environment at the rear side of the cylinder. As a result, a shear layer is formed. As seen from Figures 3.4.1 to Figure 3.4.4, the boundary layer formed along the cylinder contains a significant amount of vorticity. This vorticity is fed into the shear layer formed downstream of the separation point and causes the shear layer to roll up into a vortex with a sign identical to that of the incoming vorticity. The vortex becomes strong enough to draw the opposing vortex across the wake. The former vortex is in the clockwise direction, while that in the later vortex is in the anti-clockwise direction. The approach of vorticity of the opposite sign will then cut off further supply of vorticity to the former vortex from its boundary layer. This is the instant where the former vortex is shed. Being a free vortex, the former vortex is then convected downstream by the flow. With a further increase in Re, however, transition to turbulence occurs in the wake region. The region of transition to turbulence moves towards the cylinder, as Re is increased in the range $200<Re<300$ (see Figure 3.4.1 and Figure 3.4.2). For $Re>300$, the wake is completely turbulent. The boundary layer over the cylinder surface remains laminar, however, for increasing Re over a very wide range of Re, namely $300<Re<3\times10^5$ (see Figure 3.3.5(b)). This regime is known as the subcritical flow regime. With a further increase in Re, transition to turbulence occurs in the boundary layer itself. The transition first takes place at the point where the boundary layer separates, and then the region of transition to turbulence moves upstream over the

cylinder surface towards the stagnation point as *Re* is increased. Figure 3.4.3 and Figure 3.4.4 depict the regime is the so-called supercritical flow regime, where $3.5 \times 10^5 < Re < 1.5 \times 10^6$. In this regime, the boundary layer separation is turbulent on both sides of the cylinder. One may observe that for the relatively high *Re*, i.e. $Re = 10^3$ (see Figure 3.3.5) and $Re = 10^6$ (see Figure 3.4.3), a late separation of the vortex shedding from the surface of the circular cylinder is observed. However, a much early separation in the case with low *Re*, e.g. *Re* =200 (see Figure 3.4.1) is found. The delay is a consequence of the increase of the pressure gradient which is the difference between the minimum pressure and that at the cylinder rear. As the flow accelerates on this side of the cylinder, the process leading to the transition is triggered by the perturbations in the boundary layer.

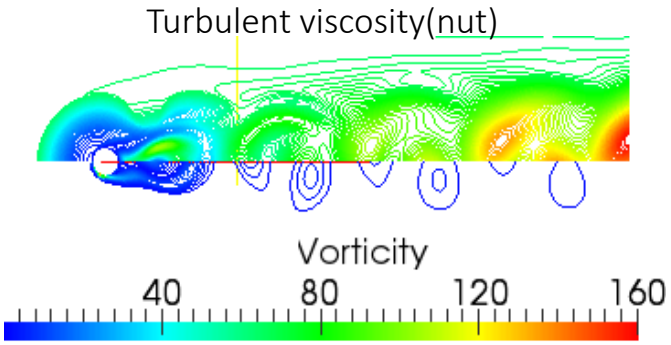

Figure 3.4.1 Spatial distribution of vorticity and turbulent viscosity around the cylinder at *Re* = 200

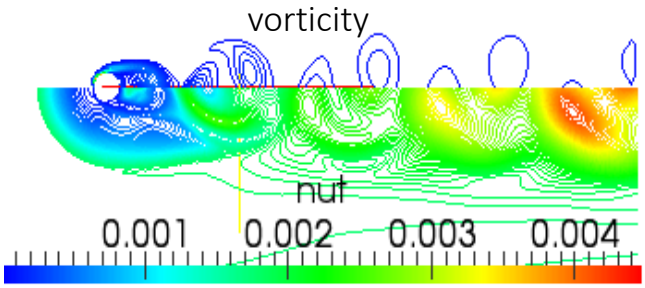

Figure 3.4.2 Spatial distribution of turbulent viscosity and vorticity around the cylinder at *Re* = 200

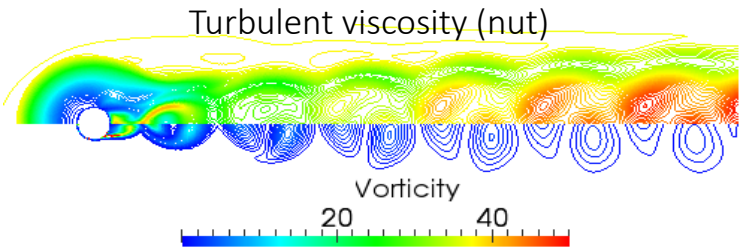

Figure 3.4.3 Spatial distribution of turbulent viscosity and vorticity around the cylinder at $Re = 10^6$

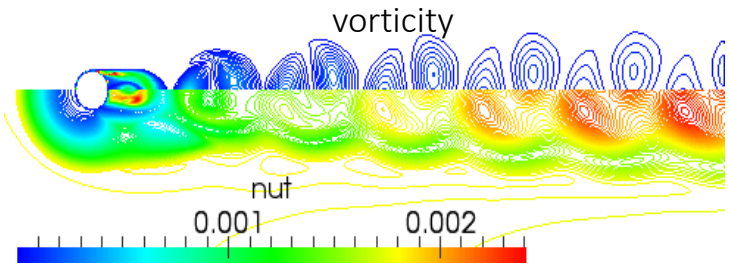

Figure 3.4.4 Spatial distribution of vorticity and turbulent viscosity around the cylinder at $Re = 10^6$

Furthermore, to quantify the size of the region where the turbulent viscosity plays an important role, the profiles of the turbulent viscosity distributions are plotted both along the transverse (e.g., *x=3D*, *x=5D* and *x=8D*) and in-line direction (e.g., *y=3D*, *y=5D* and *y=8D*) at different positions (see Figure 3.4.5). For the stationary cases, the turbulent viscosities profiles are plotted for $Re=10^3$ and 10^4 in Figure 3.4.6 to Figure 3.4.9. One may find that the turbulent viscosity and vorticity are substantial in a confined area around the vortex shedding. This confined area is referred to as the critical area in this thesis.

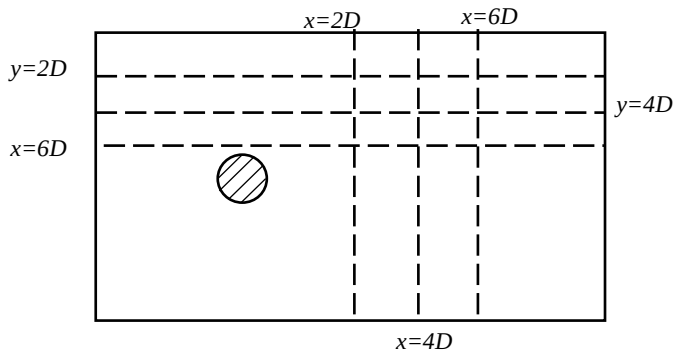

Figure 3.4.5 Sketch shows the positions where the profiles are plotted along the transverse and in-line direction

Firstly, the turbulent viscosity along the transverse direction is plotted in Figure 3.4.6 and Figure 3.4.7, in which the *x*-axis is the normalised *x* coordinate with the circular cylinder located at *y/D*=0, and *y*-axis is eddy viscosity ratio ($v'' = v_T/v$), where v_T is the turbulent viscosity caused by the turbulent effect, v is the molecular viscosity. A critical width can be observed, within which the viscosity experiences significant irregular oscillation. Nevertheless, beyond this critical boundary, the turbulent viscosity is linear and demonstrate a smooth transfer to the far-field boundary. Furthermore, for the viscosity distribution beyond the critical area at different times the vorticity and the turbulent viscosity is insignificant. Comparing profiles of different times (t_1 =25s and t_2 = 30s both after the convergence of the solution) in Figure 3.4.6, almost same critical width is determined, which is around *5D*. To reflect the unsteady behaviour of the vortex shedding, the critical width, *Wc*, in this study is defined as the maximum width of the critical area within one shedding period. The distance from the critical width boundary to the centre of the cylinder is denoted as *D**. It is assumed that the shedding vortex is symmetric to each other and therefore *W*c *=2D**. Furthermore, both Figure 3.4.6 and Figure 3.4.7 reveal that a similar *D** is observed which is approximately *5D*.

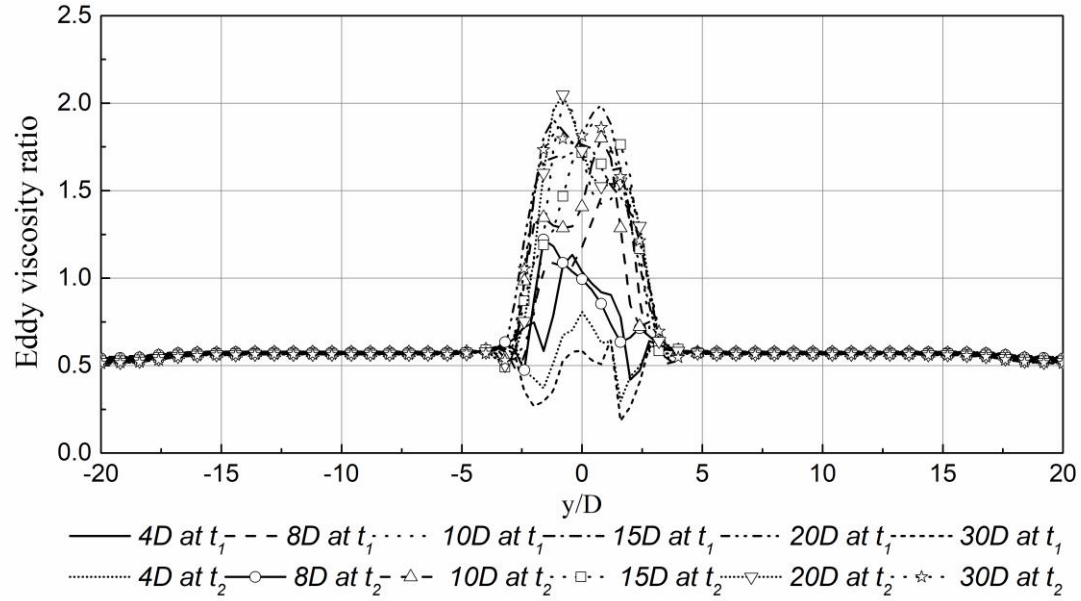

Figure 3.4.6 Turbulent viscosity at *Re*=1000 along the transverse direction

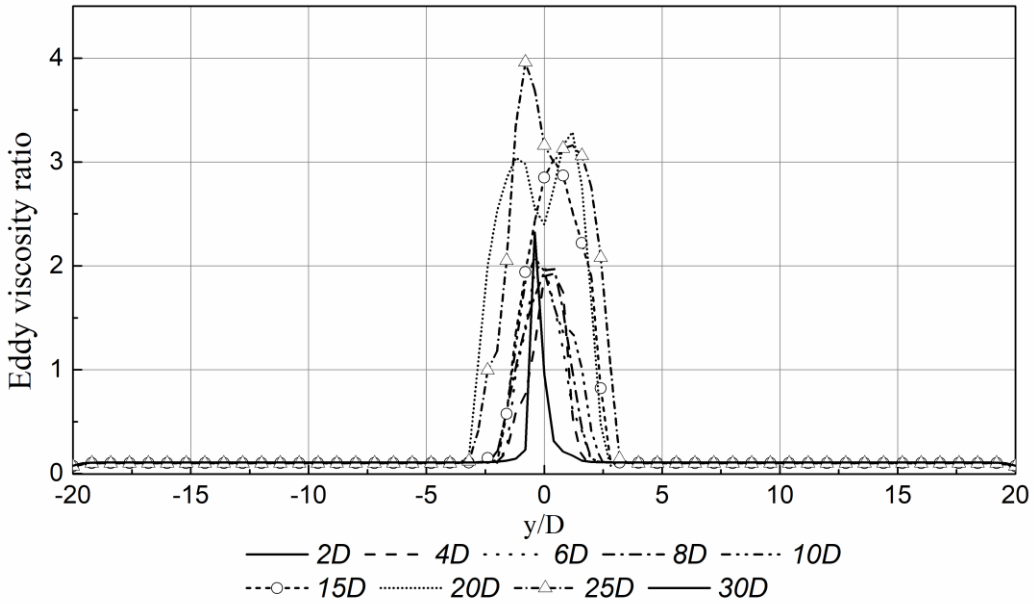

Figure 3.4.7 Turbulent viscosity at *Re*=10000 along the transverse direction

In Figure 3.4.8 and Figure 3.4.9, which the *x*-axis is the normalised *y* coordinate with the circular cylinder located at *x/D*=0, and the *y*-axis is the eddy viscosity ratio. The turbulent viscosity profile along the in-line direction is plotted for *Re*=1000 and *Re*=10000. At the front (upstream) side of the circular cylinder, an insignificant but linearly varying turbulent viscosity is observed. However, significant variation of the viscosity is triggered at the rear (downstream) of the circular cylinder. Comparing the profiles in Figure 3.4.8 and Figure 3.4.9, it can be observed that only beyond *y=7D* (*D*=7D*), the oscillation of the turbulent viscosity may be ignored and a linear distribution of the turbulent viscosity is suggested.

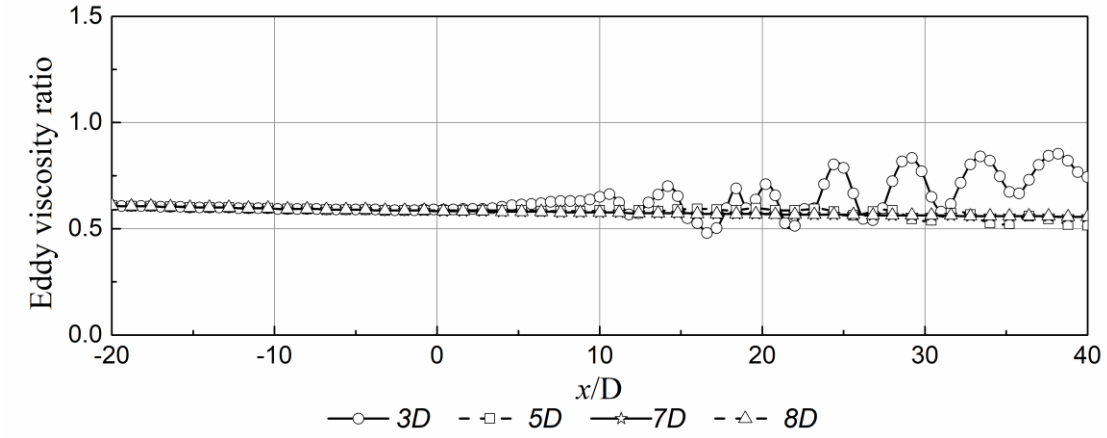

Figure 3.4.8 Turbulent viscosity at *Re*=1000 along the in-line direction

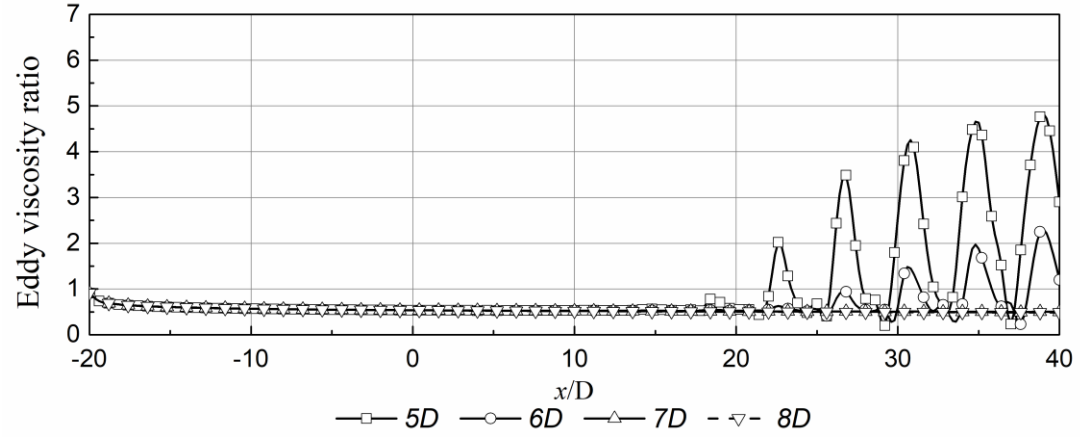

Figure 3.4.9 Turbulent viscosity at *Re*=10000 along the in-line direction

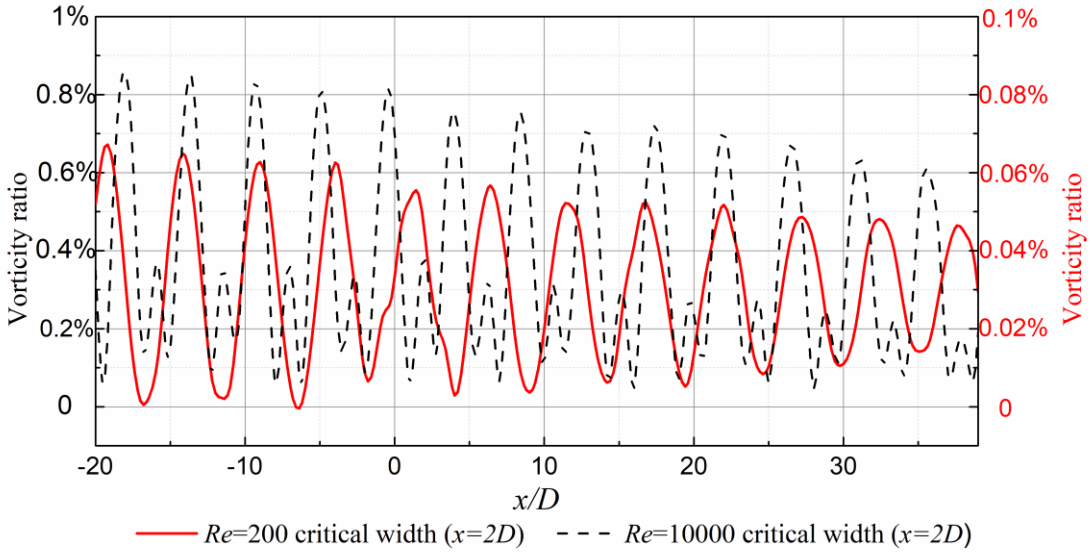

Figure 3.4.10 Longitudinal distribution of vorticity in the cases of Re=200 and 10^4

Figure 3.4.10 demonstrates the vorticity along longitudinal direction at $y = Wc/2$ for the stationary cylinder. The two y-axises are the vorticity ratios which the vorticity normalised by their own maximum vorticity around the circular cylinder. The red line is the case of Re=200, and the black line is Re=1000. It can be found that the vorticity all below the threshold, i.e. 1% of the maximum vorticity on the cylinder for the Reynolds number tested.

3.4.2 Turbulent viscosity of an oscillating circular cylinder

For the cases with an oscillating circular cylinder, the cylinder motion effects on the vortex shedding should be considered. To do so, the cylinder subjected to a forced vibration along the transversal direction with its displacement is given as (Carberry *et al.*, 2005):

$$y(t) = \frac{A}{D} sin(2\pi f_o t) \tag{3.4.1}$$

where A is the amplitude of the oscillation, f_o is the oscillation frequency. Two non-dimensional parameters are introduced: (1) the frequency ratio (Fr) is the oscillation frequency (f_o) normalized by the natural shedding frequency of the weak (f_s) from a stationary cylinder. Fr ranges from 0.8 to 1.1 in this study. (2) the amplitude ratio (A/D)

is the ratio between oscillation amplitude (A) and the diameter of the cylinder (D), which ranges from 0.2D to 0.5D. It is observed that, due to the effect of the exciting frequency, the shedding vortex does not follow the law of Strouhal and shows a non-regular pattern as demonstrated in Figure 3.4.11and Figure 3.4.12 with Fr=0.8 and 1.2, respectively.

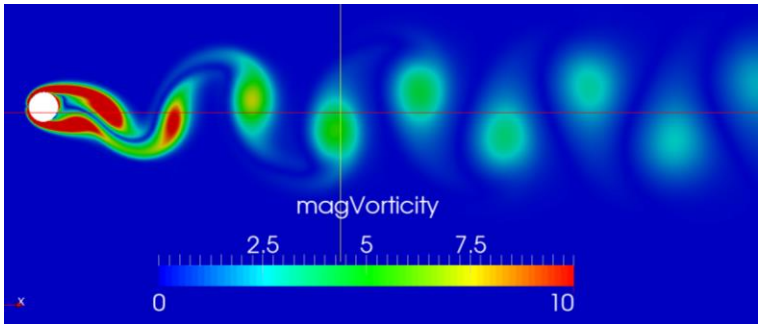

Figure 3.4.11 Vorticity distribution near moving cylinder at Re=185 for Fr=0.8

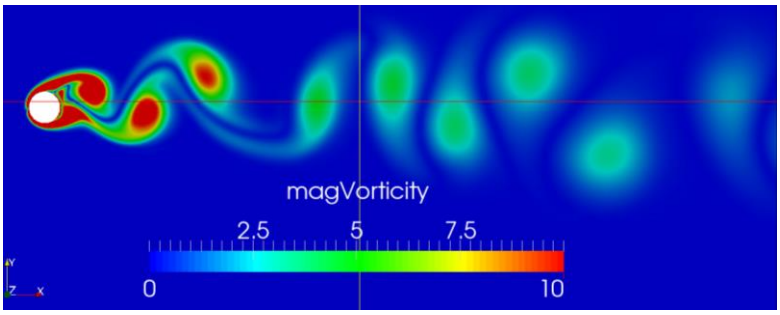

Figure 3.4.12 Vorticity distribution near moving cylinder at Re=185 for Fr=1.1

Regarding the vorticity distribution along the transverse direction, from the Figure 3.4.13 to Figure 3.4.15, it can be observed that the characteristics of viscosity are similar to that of the stationary circular cylinder. A dramatic decrease in the value of the turbulent viscosity is observed. Beyond the critical boundary, the regular and smooth turbulent viscosity is exhibited while within this region, a considerable vibration of the turbulent viscosity is found. In addition, there is no major difference between different Reynolds numbers (e.g., Re=185 and Re=2300). However, the size of the critical region is different from that in the stationary situations. For the cases with oscillating cylinders, the maximum width increases to the *6.5D* (in Figure 3.4.15), which is larger than that in the stationary cylinders.

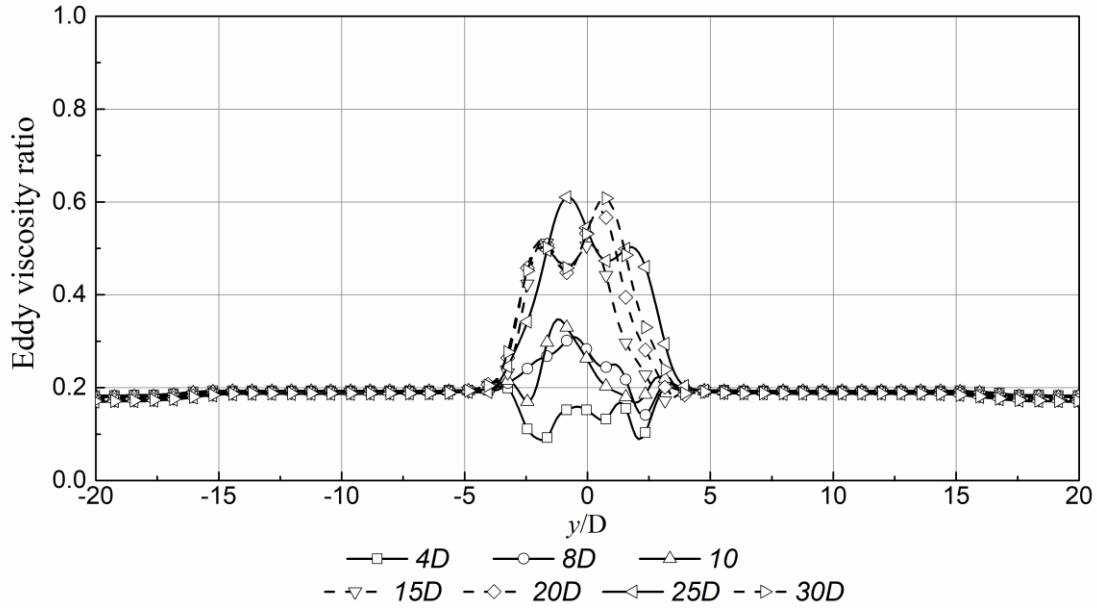

Figure 3.4.13 Eddy viscosity ratio of (*Re, A/D, Fr*) = (185, 0.2, 0.9) along the transverse direction

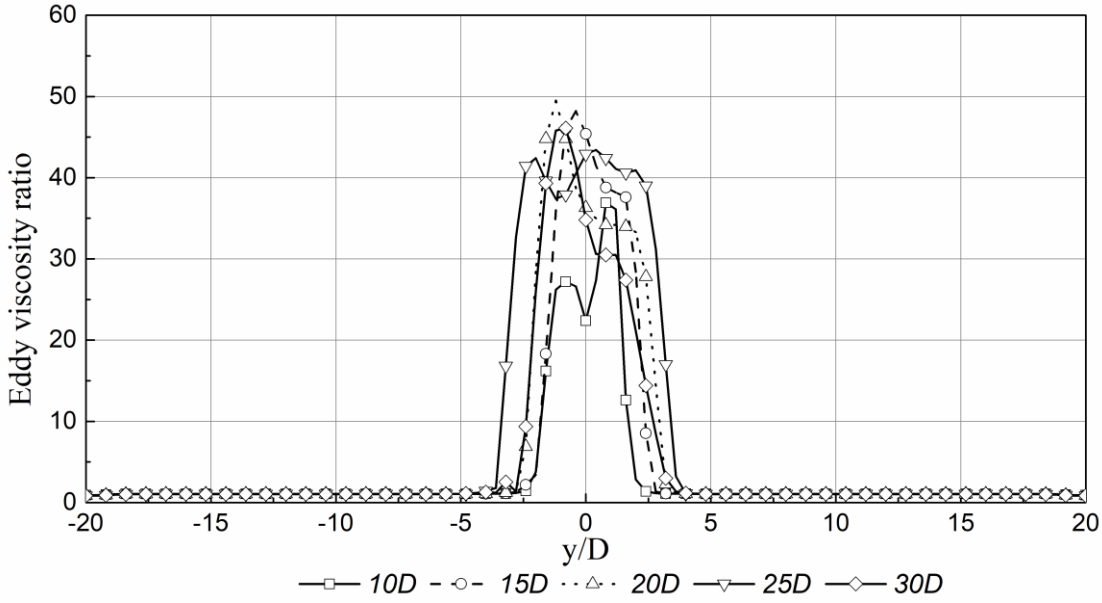

Figure 3.4.14 Eddy viscosity ratio of (*Re, A/D, Fr*) = (2300, 0.2, 1.1) along the transverse direction

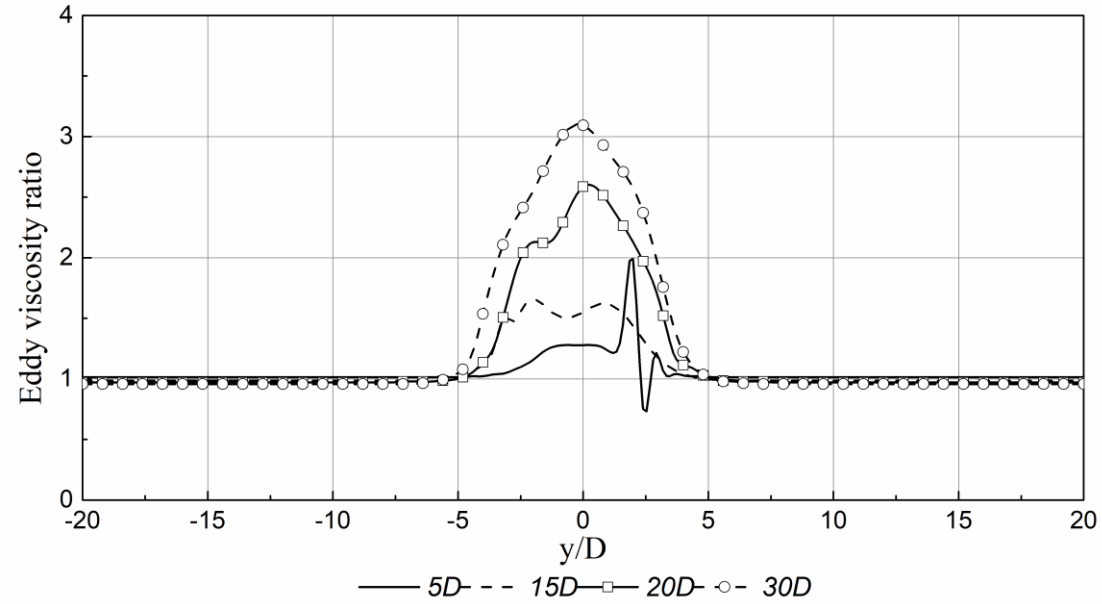

Figure 3.4.15 Eddy viscosity ratio of (*Re, A/D, Fr*) = (2300, 0.5, 0.6) along the transverse direction

Regarding the distribution of the in-line direction from Figure 3.4.16 to Figure 3.4.18, in which *x*-axis is the normalised y coordinate with the circular cylinder located at *x/D*=0, and the *y*-axis is the eddy viscosity ratio. A similar feature of the turbulent viscosity is suggested (see Figure 3.4.8 and Figure 3.4.9). For the case of (*Re, A/D, Fr*) = (2300, 0.2, 1.1) and (2300, 0.5, 0.6), *D*=7D* are observed while for (*Re, A/D, Fr*) = (185, 0.2, 0.9), a smaller critical width is found which is *6D*.

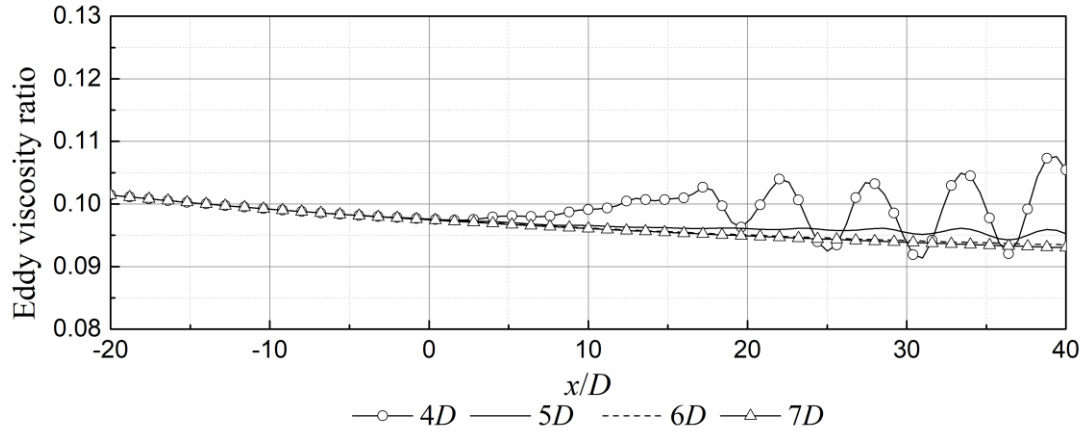

Figure 3.4.16 Eddy viscosity ratio of (*Re, A/D, Fr)* = (185, 0.2, 0.9) along the in-line direction

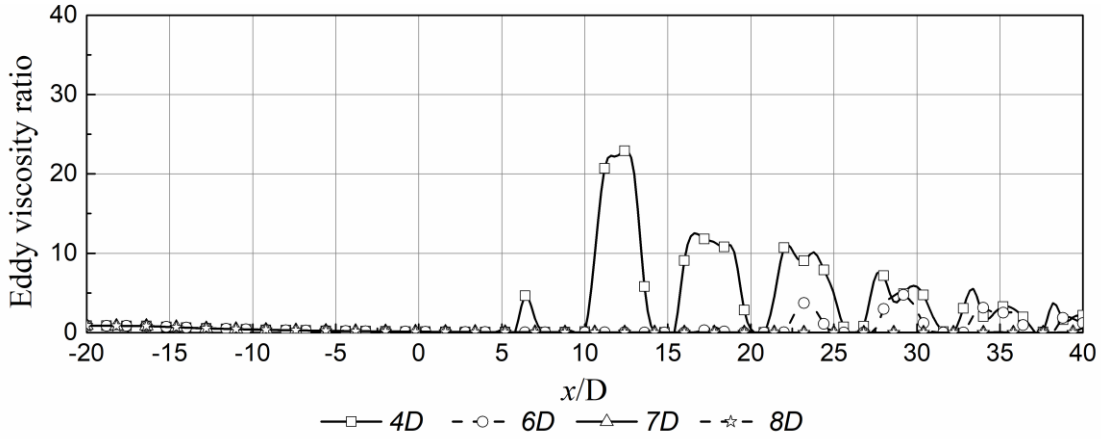

Figure 3.4.17 Turbulent viscosity of (*Re, A/D, Fr*) = (2300, 0.2, 1.1) along the in-line direction

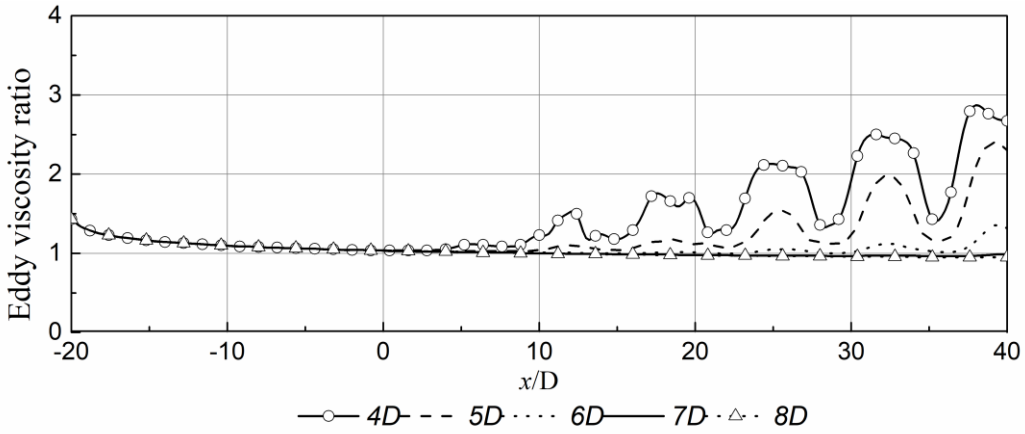

Figure 3.4.18 Turbulent viscosity of (*Re, A/D, Fr*) = (2300, 0.5, 0.6) along the in-line direction

3.4.3 Size of the overlapping domain

According to the investigation of the turbulent viscosity spatial distribution, we understand that: (1) the turbulent viscosity is significant only in a confined area around the vortex shedding (critical area); (2) the motion of the cylinder may affect the spatial distribution of the turbulent viscosity, enlarging the critical area; (3) Figure 3.4.19 illustrates that the width of the critical area varies with the different working conditions, but the variation is between *10-16D* in the cases examined.

Based on the understanding of the spatial distribution of the turbulent viscosity, we can draw the conclusion that there exists one critical width, beyond which the turbulent viscosity is regular and linear. Not like the viscosity within the critical region, which

requires a turbulent model, the far field viscosity can be modelled by a linear function. Finally, in order to make sure the critical region is covered by the residual turbulent model, the critical width adopted in this thesis is fixed to *16D*.

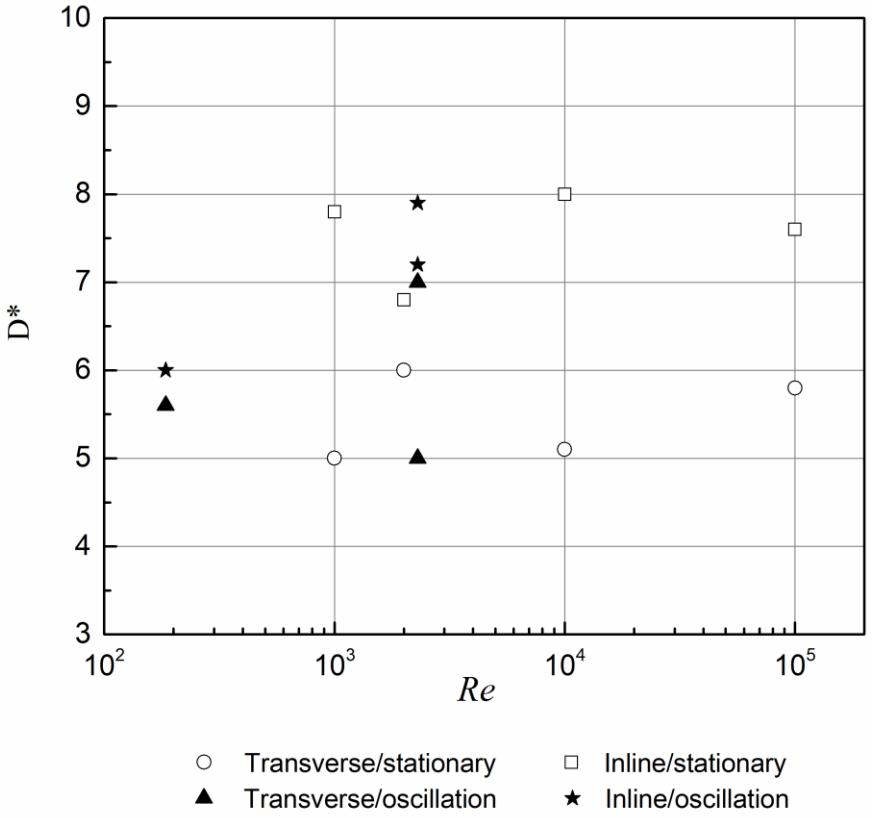

Figure 3.4.19 Range of *D** under different working conditions

3.5 Vortex shedding behaviour in multiphase flow

The feature of turbulent viscosity associated with vortex shedding without the free surface has been studied in the above section. Nevertheless, there are great differences in terms of the spatial variation of the turbulent viscosity between the situation with and without the free surface. Therefore, the question is how the presence of the free surface effect the vortex shedding behaviour, hydrodynamic force coefficient, shedding frequency and flow pattern. There are two main parameters related to the flow past a circular cylinder with the presence of the free surface: (1) $Fr' = U/\sqrt{gD}$,where g is the acceleration due to gravity; U is the upstream velocity, D is the cylinder diameter; (2) and the gap ratio *h/D*, with *h* is the distance between the centre of the cylinder and the

water surface (see Figure 3.5.1). In order to answer the above posed questions, the investigations of the circular cylinder near the free surface is carried out. The main purpose of this study is to assess the impact of the submergence depth (*h/D*), Froude number (Fr') to the vortex shedding behaviour.

The sketch of the problems considered in this study is illustrated in Figure 3.5.1, showing a fixed circular cylinder beneath a free surface, in which ν_a and ν_w is the molecular viscosity of air and water, respectively; ρ_a and ρ_w is the density of air and water, respectively. The working conditions can be summarised as (1) The Froude number ranges from 0.25 to 0.4, which covers the critical Fr' value according to the existing research in the public domain; (2) The submergence depth ranges from *0.2D* to *3D*; (3) Only considering low-*Re* cases, i.e. *Re*=100 and 200 according to previous test without free surface which shows that the *Re* does not significantly affect the size of the critical zone. Such working conditions are illustrated as a matrix in Figure 3.5.2. The discussions of the Froude number, gap ratio and Reynolds number to the lift force, flow properties, shedding frequency and vortex mode are demonstrated below.

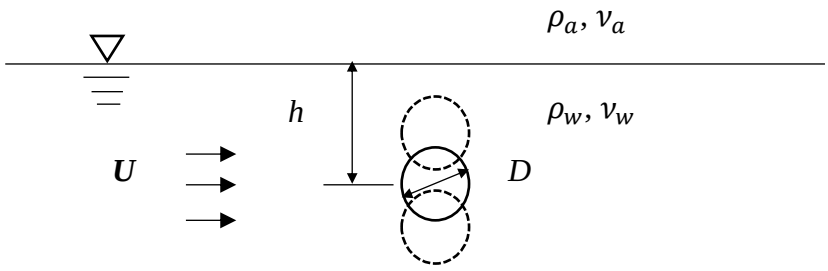

Figure 3.5.1 Sketch of the studied multiphase flow problem

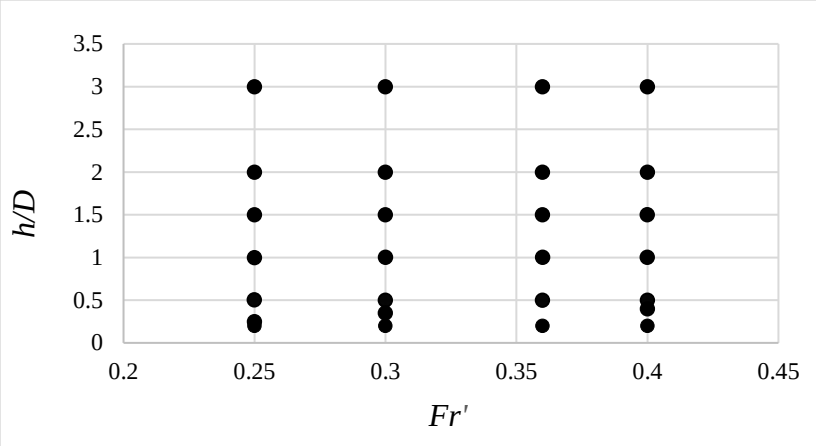

Figure 3.5.2 Working condition matrix for the influential parameters of Froude number and gap ratio

In the present work, a multiphase flow solver in OpenFOAM is used. A domain size of *40D*×*60D* is adopted in which $D_{in} = 20$ and $D_{out} = 40$ (see Figure 3.3.1). The size of D_{out} is relying on the consideration of the fully development of the shedding. A multi-block grid system is adopted this study, in which the mesh is clustered in the boundary layer, weak region and free surface. The mesh configuration is similar to the illustration of the computational mesh shown in Figure 3.3.1. It is also noted that the interfacial region between the air and the water phases is typically smeared over a few grid cells and is therefore highly sensitive to grid resolution. For this reason, a further mesh refinement near the free surface is required. The gird resolution has been carefully and properly chosen for each considered case. The time step is automatically adjusted according to the selected courant number which is around 0.4 in this study. Although the Courant number used in this test is much larger than that used in the cases without free surface, the value has justified in the preliminary convergent study, which also includes the effects of the mesh resolutions on achieving convergent results. The corresponding tests are not presented in this section to save the space.

3.5.1 Effect of Froude number

Not all the cases tested in the working conditions matrix in Figure 3.5.2 will be demonstrated, only the cases with the typical physics are discussed here. Regarding the effect of the Froude number, through the test of the working conditions in the matrix, it is observed that with the Froude number excess the value around 0.3, the surface distortion becomes substantial. Figure 3.5.3 shows the free surface and the vortex street at the wake under different Froude numbers at fixed gap ratio h/D=2. Figure 3.5.3(a) is the results with a small Fr', i.e. 0.25 while Figure 3.5.3(b) with a relatively larger Fr', i.e. 0.36. Comparing the two conditions, it is clearly shown that the water surface sharpening at higher Froude number which also leads to the vortex shedding frequency variation in the wake and even the breaking of the water surface (see Figure 3.5.3 (b)). Furthermore, the water surface sharpening is also associated to the increase of the vorticity at the free surface.

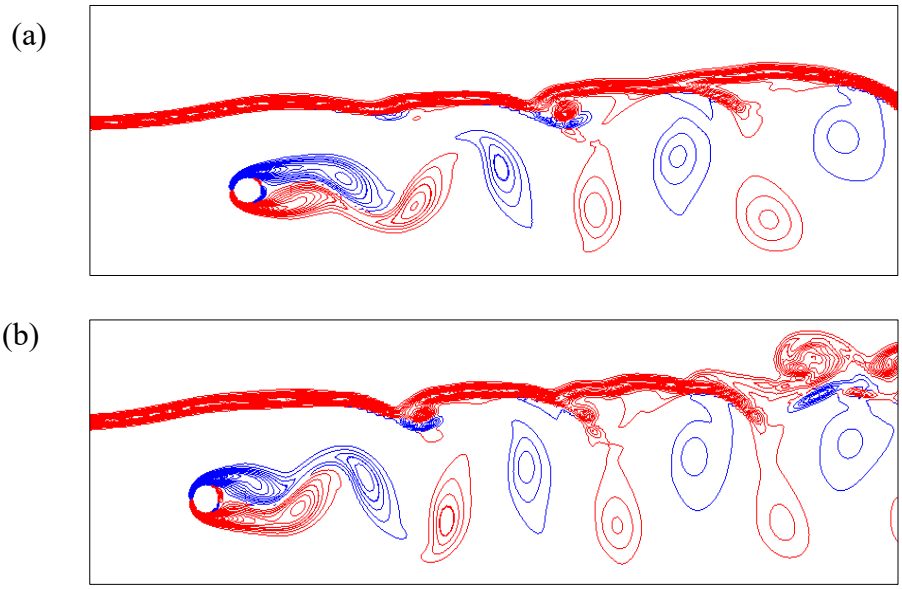

Figure 3.5.3 Vortex shedding and free surface for different Froude numbers (a) Fr'=0.25 (b) Fr'=0.36 at same gap ratio h/D=2.

Figure 3.5.4 demonstrates the time history of the lift coefficient for different Froude number with the fixed gap ratio h/D=1. The frequency of the lift coefficient that associated with the Strouhal number also indicates the variation of the shedding

frequency. The results with Fr'=0.36 in the dashed line show a 12% increase of the Strouhal number compared to the results with lower Froude number. In addition, almost the same amplitude of the lift coefficient is observed in the cases with the two Froude numbers.

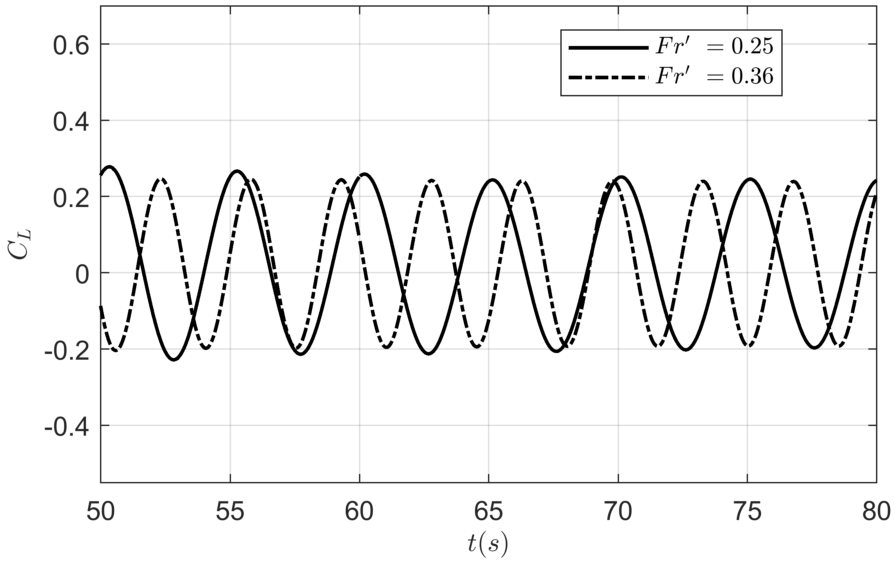

Figure 3.5.4 Time history of C_L for the *h/D*=1 with Fr'=0.25 and Fr'=0.36

3.5.2 Effect of gap ratio

A very similar trend is observed base on the investigation of the gap ratio, which deceases from 3 to 0.2. With the decrease of the gap ratio under specific Froude number, the larger deformation of the free surface is observed. The big surface curvature also leads to the strong interaction between the free surface and the vortex street in the wake of the circular cylinder (see Figure 3.5.5). Additionally, an asymmetric staggered array of vortices at the downstream appears with the decrease of the gap ratio. The attached free surface and vortex street greatly alter the development of the vortex, formation length and shedding frequency, see (b), (c) and (d).

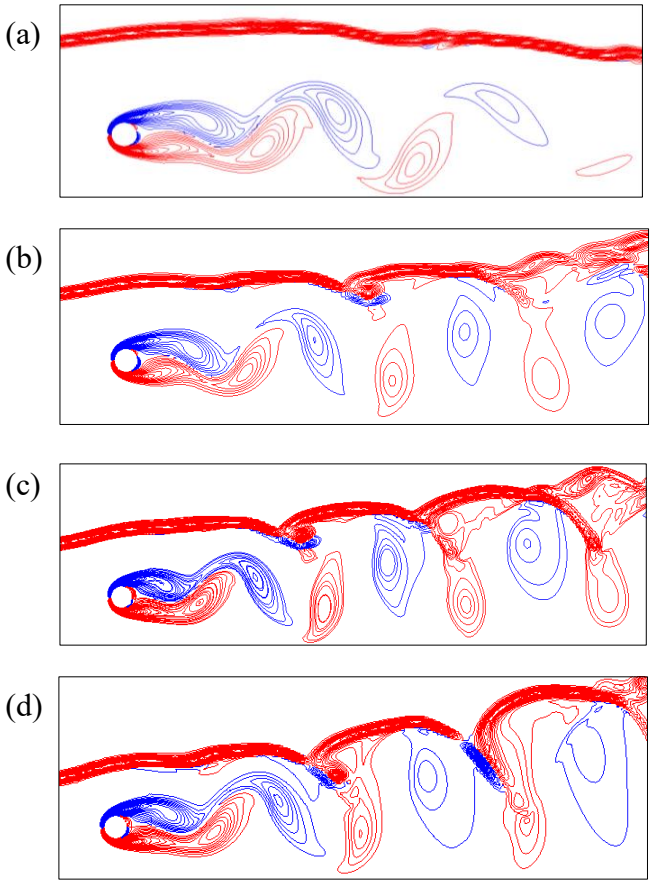

Figure 3.5.5 Vortex shedding and free surface for Fr'=0.25 for a gap ratio of (a) *h/D* =3; (b) *h/D*=2; (c) *h/D*=1; (d) *h/D*= 0.5 for the *Re* =100.

Similarly, in the Figure 3.5.6, the variation of the Strouhal number is also observed with different gap ratios (*h/D*=2.5 and *h/D*=1 with fixed Fr'=0.36). Furthermore, the asymmetric lift coefficient appears in for both tested gap ratio. However, unlike the effect of the Froude number, the amplitude of the lift coefficient shows an approximately 10% reduction comparing the gap ratio *h/D*=0.25 to that of *h/D*=1.

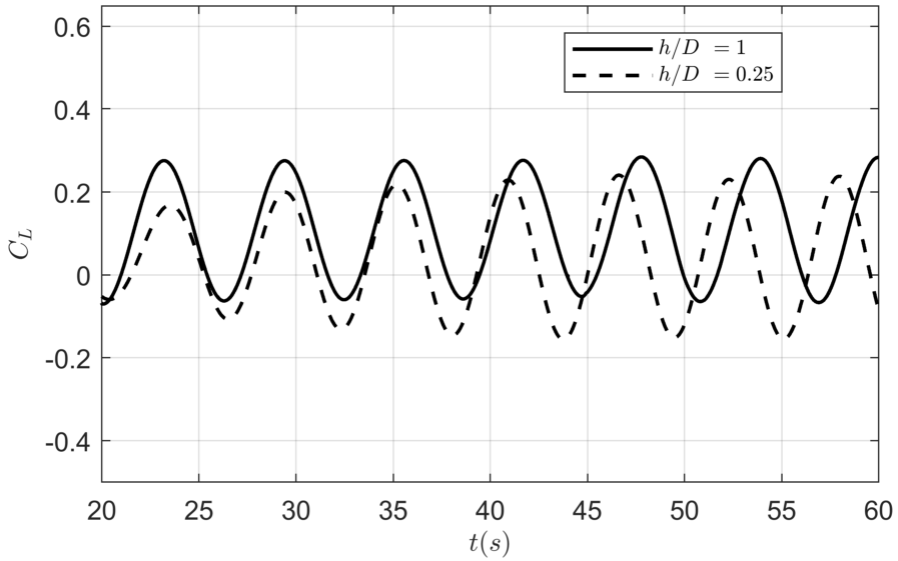

Figure 3.5.6 Time history of C_L for the *Re*=100, Fr'=0.36 with *h/D*=2.5 and *h/D*=1

Figure 3.5.7 gives the time history of lift coefficient for the *Re*=200 subject to Fr'=0.25 and Fr'=0.36 with fixed gap ratio, respectively. Similar to laminar flow case, the Froude number mainly influence the lift frequency which associated with the shedding frequency rather than the amplitude of lift coefficient.

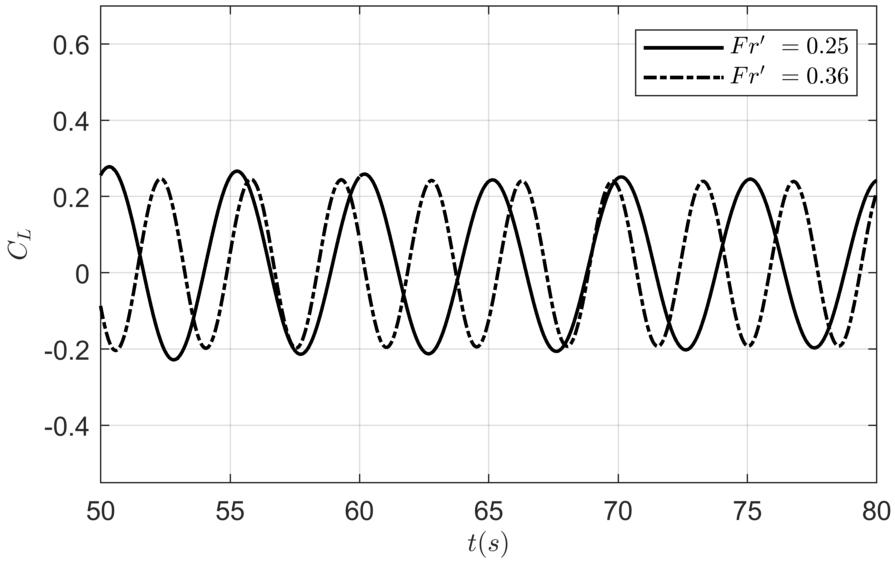

Figure 3.5.7 Time history of C_L for the *Re* =200 with Fr'=0.25 and Fr'=0.36

3.5.3 Conclusions of the investigation

In this study, the lift force on the cylinder and shedding frequency of the structure of the near wake is numerically investigated using a two-phase solver. At both laminar and turbulent Reynolds number, a series of simulations covering various Fr' and h/D are conducted.

The main conclusions of the presented study are as follows: (1) when Froude number exceeds 0.3, the free surface distortion becomes substantial. Lift coefficient keeps the same, but vortex shedding frequency varies. As suggested by Figure 3.5.4, a difference of 12% regarding the frequency of the lift coefficient is observed between Fr'=0.36 and the results with lower Froude number. The similar trend is observed in other Froude number effect test cases as well. (2) The decrease of the gap ratio results in the changes with respect to the development of the vortex, formation length and shedding frequency for both laminar and turbulent flows. An asymmetric array of vortices (see Figure 3.5.5) and different lift coefficient amplitudes (see Figure 3.5.6) are observed in the cases with different gap ratio. (3) The critical boundary is recognized between Zone 1 and Zone 2 in Figure 3.5.8, according to the comparison between cases under the effect of free surface to that of deep water working conditions with respect to the force act on the circular cylinder and shedding frequency.

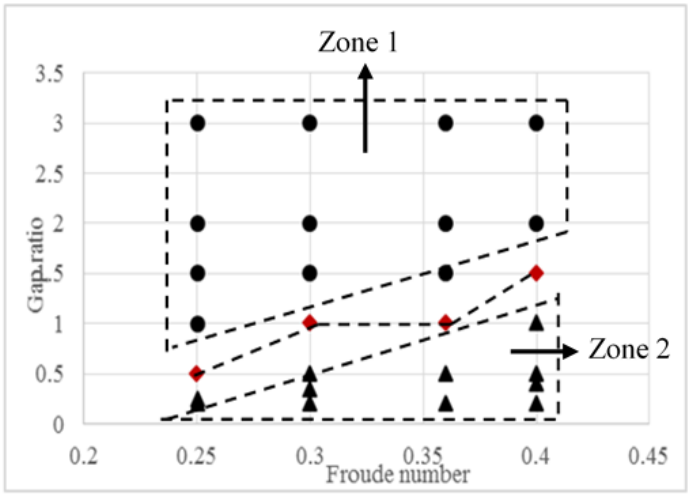

Figure 3.5.8 Zone 1 and Zone 2 for the tested working conditions

Through this investigation, more understandings of this physics and insights into the coupling method with the presence of the free surface is achieved. The recognition of the critical boundary is of great importance for the development of the multiphases hybrid method. (1) For the cases in the Zone 2 (e.g. woking conditions with Fr'=0.35, h/D<1), due to the significance of the vorticity at the free surface, the behaviour of the wake is considerably influenced by the interaction between the free surface and the vortex shedding in Zone 2. Hence, then the free surface cannot be treated as inviscid and applying the simplified solver to obtain the proper solutions. Consequently, different coupling strategy should be applied to deal with the vorticity at the free surface, that is to say, a viscous or turbulent solver is required to capture the turbulent viscosity. (2) For the case belongs to Zone 1 (e.g., cases of Fr'=0.35, h/D>1), the vorticity change caused by the existence of the free surface can be ignored. Therefore, an inviscid solver is accurate enough to achieve the satisfactory solutions.

4

METHODOLOGY AND MATHEMATICAL FORMULATIONS

The preliminary investigations shown in Chapter 3 using the conventional RANS solver with k-ω SST reflects the fact that the turbulent viscosity is only important in the critical region near the cylinder and can be ignored in other area far away from the structures. It also systematically investigates the size of the critical zone under different working conditions. These form the basis of the hybrid model development, i.e. one can use one model without considering the turbulent viscosity outside the critical region and another one with turbulent modelling in the critical zone through fulfilling its theoretical hypothesis. As discussed in Chapter 1 and 2, the two typical approaches i.e. (1) the spatially hierarchical approach (domain splitting or domain decomposition, e.g. (Hafez *et al*., 2006), in which the computational domain is decomposed into two subdomains, the critical regions and the remaining, respectively: in the critical region, RANS with k-ω SST is adopted; in the other, RANS with zero turbulent viscosity is applied; (2) the function splitting (or model/velocity decomposition, e.g. Luquet *et al*., 2007; Kim *et al*., 2005; Edmund 2012), in which a simplified model (i.e. RANS with zero turbulent

viscosity) covers the entire computational domain and a complementary NS model is solved in the critical zone to correct the solution of the simplified models so that within this subdomain, the flow is governed by the RANS with k-ω SST by summing the solution of the simplified model and that of the complementary NS model. This strategy improves the computational efficiency by limiting the computational domain governed by the more time-consuming solver to a considerably smaller area. In this work, the functional splitting approach is applied.

4.1 Methodology of hybrid method for single-phase flow

4.1.1 Functional decomposition approach

In this approach, the velocity and pressure are split into two parts as follows:

$$u_{Ti}(x,t) = u_{si}(x,t) + u_i^*(x,t) \tag{4.1.1}$$

$$p_T(x,t) = p_s(x,t) + p^*(x,t) \tag{4.1.2}$$

In which, $u_{si}(x,t)$ and $p_s(x,t)$ are the velocity and pressure solutions to a relatively simpler solver. $u_i^*(x,t)$ and $p^*(x,t)$ are the residual values between the solutions to the simpler solver and those to the relatively more accurate solution generally obtained by a more complicated and time-consuming solver (Luquet *et al*., 2007). Thus, the desired complete fields $u_{Ti}(x,t)$ and $p_T(x,t)$ can be obtained by summing up the two individual parts together.

It is particularly important to note that for a given total velocity, the decomposition is not unique and therefore, different hybrid models could be developed (Kim *et al*., 2005; Edmund 2012). It is understood that the proper decomposition could result in both a faster convergence of the residual field and a better overall accuracy of the total solution. In this hybrid method, the total velocity and pressure are constructed as

$$u_{Ti}(x,t) = u_{fi}(x,t) + u_i^*(x,t) \qquad (i = 1,2) \tag{4.1.3}$$

$$p_T = p_f(x,t) + p^*(x,t) \tag{4.1.4}$$

where the fields with the subscript f are the solutions of a quasi-turbulent model, which will be described below, while these with superscript * are the residual solutions, which

are the differences between the solutions of the quasi-turbulent model and the total solutions. The configuration of the hybrid models is illustrated in Figure 4.1.1.

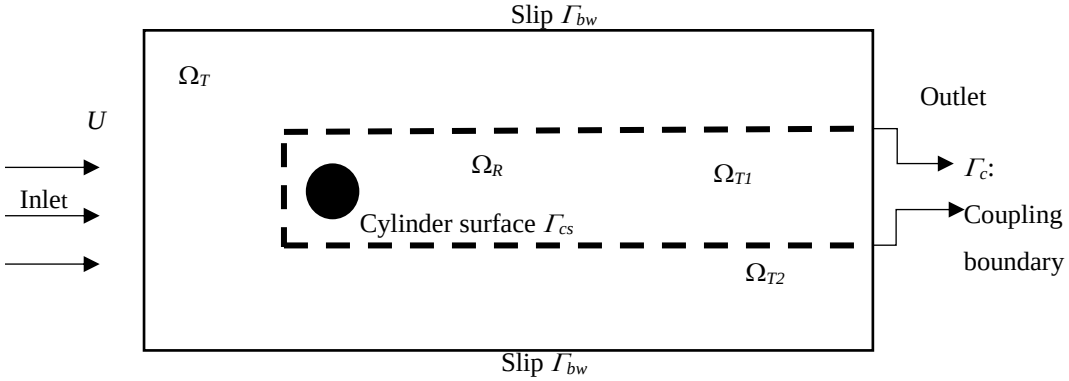

Figure 4.1.1 Sketch of the hybrid method computational domain

Ω_T in the above figure is the entire computational domain, in which the quasi-turbulent solutions are found. This is also called the quasi-turbulent domain hereafter for the convenience. This domain is composed of two parts: $\Omega_T = \Omega_{T1} + \Omega_{T2}$ as shown. Ω_R is a zone near the structure, in which the corresponding residual solutions are sought. The boundary (Γ_c) of Ω_R is denoted by the dashed line. Obviously, Ω_R is overlapping with Ω_T , which size is identical to Ω_{T1} but with different solver applied.

4.1.2 Quasi-turbulent model

In the presented hybrid model, $u_f(x,t)$and $p_f(x,t)$ solved by the quasi-turbulent model satisfy the following incompressible continuity and Navier-Stokes equations for single-phase applications,

$$\frac{\partial u_{fj}}{\partial x_j} = 0 \tag{4.1.5}$$

$$\frac{\partial u_{fi}}{\partial t} + (u_{fj} - u_{bj})\frac{\partial u_{fi}}{\partial x_j} = -\frac{1}{\rho}\frac{\partial p_f}{\partial x_i} + \frac{\partial}{\partial x_j}\left[\nu'\left(\frac{\partial u_{fi}}{\partial x_j} + \frac{\partial u_{fj}}{\partial x_i}\right)\right] \quad (i = 1,2) \tag{4.1.6}$$

where $\nu'(x,y,t)$ is the effective viscosity field. The treatment of this effective viscosity field $\nu'(x,y,t)$ is of vital importance to ensure the robustness and the stability of the hybrid method. As observed, the model seems to be identical to the ALE forms of the conventional RANS model for turbulent flow. However, a considerable difference lies

on the treatment of the $v'(x, y, t)$, which will be discussed in the section of 4.1.5. For convenience and reflecting such difference, the model is referred to as the quasi-turbulent model. The corresponding boundary conditions include:

1) Right end of the domain, i.e. the outlet boundary, where the velocity satisfies the Neumann zero-gradient boundary condition, given by

$$\frac{\partial u_{fi}}{\partial x} = 0, (i = 1) \tag{4.1.7}$$

2) Top and bottom boundaries (Γ_{bw}), where the slip boundary condition is implemented,

$$u_{fn} = 0 \tag{4.1.8}$$

$$\frac{\partial u_{f\tau}}{\partial \tau} = 0 \tag{4.1.9}$$

3) Structure surface (Γ_{cs}), non-slip condition is applied,

$$u_{fi} = u_{csi} \qquad \text{On } \Gamma_{cs} \quad (\text{i} = 1, 2) \tag{4.1.10}$$

where u_{cs} is the velocity of structure surface, which is zero in the cases with stationary structure.

4.1.3 Residual turbulent model

In $\Omega_{R,}$ it is expected that the completed velocity and pressure satisfies the RANS with k-ω SST model for evaluating the effective viscosity. By substituting the decomposition Equation (4.1.3) and Equation (4.1.4) to the Equation (3.2.2), it is not difficult to obtain the continuity and momentum equations for the residual fields as follows:

$$\frac{\partial u_j^*}{\partial x_j} = 0 \tag{4.1.11}$$

$$\frac{\partial u_i^*}{\partial t} + (u_{fj} + u_j^* - u_{bj})\frac{\partial u_i^*}{\partial x_j} = \frac{\partial}{\partial x_j}[\, v_{eff}\left(\frac{\partial u_i^*}{\partial x_j} + \frac{\partial u_j^*}{\partial x_i}\right)] - \frac{1}{\rho}\frac{\partial p^*}{\partial x_i} - S_{fi} \qquad (i = 1, 2) \tag{4.1.12}$$

where

$$S_{fi} = \frac{\partial u_{fi}}{\partial t} + (u_{fj} + u_j^* - u_{bj})\frac{\partial u_{fi}}{\partial x_j} - \frac{\partial}{\partial x_j}\left[\, v_{eff}\left(\frac{\partial u_{fi}}{\partial x_j} + \frac{\partial u_{fj}}{\partial x_i}\right)\right] + \frac{1}{\rho}\frac{\partial p_f}{\partial x_i} \qquad (i = 1, 2) \tag{4.1.13}$$

The above equations are referred to as the residual turbulent model in this work. Clearly, the continuity equation in the residual turbulent model exhibits the same form

as that in the quasi-turbulent model. Nevertheless, there is an extra term S_{fi}introduced in the Equation (4.1.12) comparing to that of the RANS momentum equation. S_f may be treated as an explicit term, if the solution to the quasi-turbulent model is sought at prior at each time step. The values of u* and v_{eff} in Equation (4.1.13) are explicitly guessed by using that in the previous time step. The details of the numerical implementation will be discussed below.

(1) Similarly, the boundary conditions for the residual turbulent model can be derived. On the structure surface (see Figure 4.1.1), the boundary condition for the residual field reads,

$$u_i^* = u_{Ti} - u_{fi} = 0 \qquad on\ \Gamma_{cs}, (i = 1, 2) \tag{4.1.14}$$

(2) The corresponding boundary condition for the outlet satisfies:

$$\frac{\partial u_i^*}{\partial x} = \frac{\partial u_{Ti}}{\partial x} - \frac{\partial u_{fi}}{\partial x} = 0 \quad (i = 1, 2) \tag{4.1.15}$$

(3) On the boundary of the residual turbulent model (Γ_c), it is assumed that $v' = v_{eff}$. Under such assumption, the solutions to the quasi-turbulent model are identical to the conventional RANS model. This means that the residual values should be zero,

$$u_i^* = 0 \qquad on\ the\ \Gamma_c, \ \ (i = 1, 2) \tag{4.1.16}$$

It should be noted that in the PISO algorithm applied in this presented hybrid method, the corrector updating the velocity within each loop is using the pressure gradient rather than the pressure value. It means the pressure gradient boundary condition is numerically more efficient. Additional, the simulations using both the zero-gradient pressure boundary (type 1) and zero pressure (type 2) are conducted which keep the rest of the setting the same. The field profile comparisons between the two types of the boundary conditions are demonstrated in Fig. 4.1.2, in which the *x*-axis is the normalised *x* coordinate with the circular cylinder located at *y/D*=0, and *y*-axis is residual velocity and pressure. From Fig. 4.1.2, it can be observed that same result of the residual velocity and pressure field are yielded. Besides, the residual velocity and pressure fields are gradually approaching the coupling boundary (Γ_c) to zero which also indicates the pressure distribution satisfies the zero-gradient boundary condition.

Therefore, the boundary condition for p^* , can be achieved through Equation (4.1.13) and (4.1.16), adopted in this model is given as follows:

$$\frac{\partial p^*}{\partial n} = 0 \qquad On\ the\ \Gamma_c \tag{4.1.17}$$

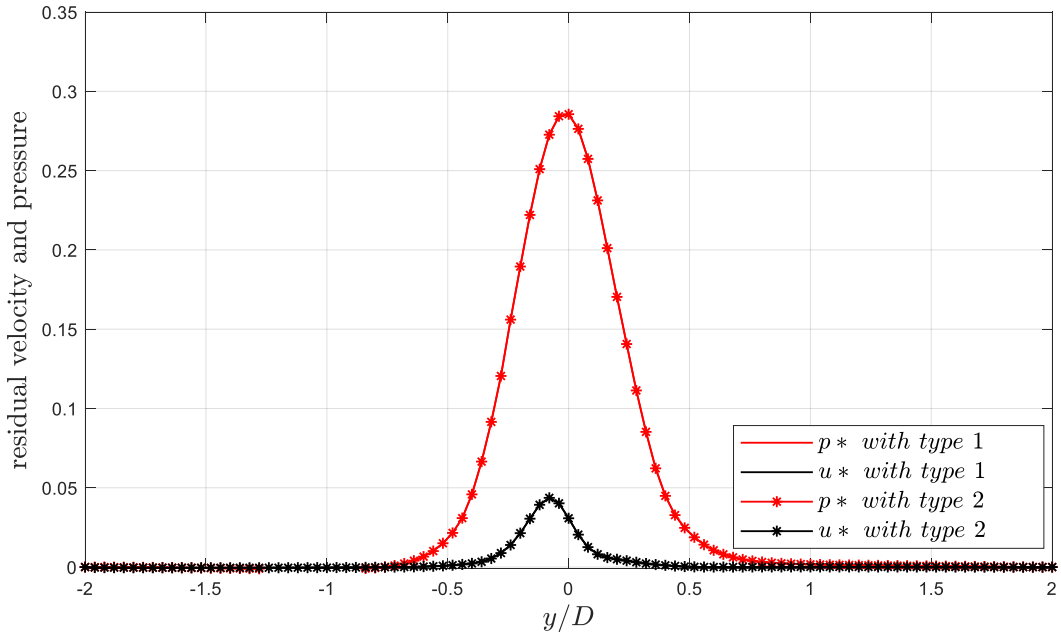

Fig 4.1.2 The field profile comparison between the two types of the boundary conditions

4.1.4 Techniques of turbulent viscosity treatment

It shall be noted that the assumption imposed on Γ_c is only valid if the size of $\Omega_{R,}$ is sufficiently large, consequently, Γ_c falls in the location where the turbulent viscosity is physically insignificant. One may select a large size of $\Omega_{R,}$ e.g. the same size as $\Omega_{T,}$ for guarantee. Nevertheless, as the increase of $\Omega_{R,}$ the computational efficiency of the hybrid model is expected to decrease. This makes the determination of the size of $\Omega_{R,}$ (or the location of Γ_c) becomes critically important. An optimal configuration of $\Omega_{R,}$ largely relies on a good understanding of the spatial distribution of the turbulent viscosity, as discussed in the previous chapter. Such knowledge lead to the determination of the critical region, in which the turbulent viscosity and the vorticity of the fluid are significant. More details will be given here.

In addition to the above-mentioned constraint on assigning $\nu'(x, y, t)$, i.e. $\nu' = \nu_{eff}$ at Γ_c, there is additional constraint in terms of numerical stability and the continuity of the solutions in the entire computational domain. As shown, after the summation of the solutions to the quasi-turbulent and the residual turbulent model in $\Omega_{R,}$ the eventual governing equation in such region is the RANS, where the effective viscosity ν_{eff} is evaluated by using the k-ω SST model. Nevertheless, in other region, i.e. Ω_{T2}, the quasi-turbulent model governs the fluid flow. Comparing the RANS and the quasi-turbulent model, the only difference exhibits in the value of the effective viscosity, i.e, $\nu'(x, y, t)$ and $\nu_{eff}(x, y, t)$ in Ω_{T2} and $\Omega_{R,}$ respectively. In the numerical practices, one needs to ensure a continuity of $\nu'(x, y, t)$ at Γ_c in numerical practices. Otherwise, numerical instability may occur near the boundary Γ_c.

To consider the above two constraints, two techniques are employed to bridge the inconsistency of the effective viscosity between the residual and quasi-turbulent solvers. First, the turbulent viscosity and thus the effective viscosity evaluated by the turbulence model in $\Omega_{R,}$ will be mapped to the same region in the quasi-turbulent domain, i.e. Ω_{T1}, using an appropriate numerical interpolation. Secondly, the smooth transition of the effective viscosity is taken into account from Γ_c extending to other regions in Ω_{T2}. Eventually, the effective viscosity in the quasi-turbulent region is specified by Equation. (4.1.18).

$$\nu'(x, y, t) = \begin{cases} \nu_{eff}(x, y, t) & \Omega_{T1} \\ \nu_{eff}(x_{\Gamma c}, y, t) - \dfrac{\nu_{eff}(x_{\Gamma c}, y, t) - \nu}{x_b - x_{\Gamma c}}(x - x_{\Gamma c}) & \Omega_{T2x} \\ \nu_{eff}(x, y_{\Gamma c+}, t) - \dfrac{\nu_{eff}(x, y_{\Gamma c+}, t) - \nu}{y_{b+} - y_{\Gamma c+}}(y - y_{\Gamma c+}) & \Omega_{T2y+} \\ \nu_{eff}(x, y_{\Gamma c-}, t) - \dfrac{\nu_{eff}(x, y_{\Gamma c-}, t) - \nu}{y_{b-} - y_{\Gamma c-}}(y - y_{\Gamma c-}) & \Omega_{T2y-} \end{cases} \tag{4.1.18}$$

where $\nu'(x, y, t)$ in Ω_{T1} is assigned to be the effective viscosity by the residual solver using the chosen turbulent model, i.e. $\nu_{eff}(\mathrm{x,y,t})$; the domain Ω_{T2} are split into three subregion, i.e. $\Omega_{T2x}, \Omega_{T2y+}$ and Ω_{T2y-}, as illustrated in Figure 4.1.2; x_b and $x_{\Gamma c}$ are the

x-coordinate of the inlet boundary of the quasi-turbulent domain and the left boundary of Ω_{T1}; y_{b+} and $y_{\Gamma c+}$ are the y-coordinates of the upper boundaries of Ω_T and Ω_{T1}, respectively; y_{b-} and $y_{\Gamma c-}$ are the y-coordinates of the lower boundaries of Ω_T and Ω_{T1}, respectively.

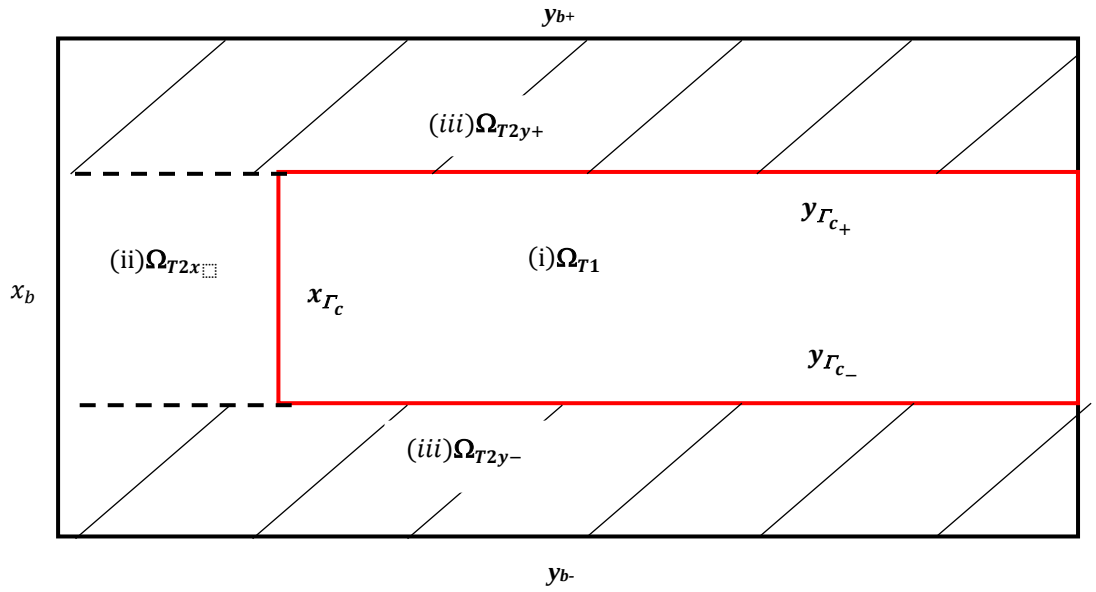

Figure 4.1.2 Variables transfer between the domain of Ω_T and Ω_R

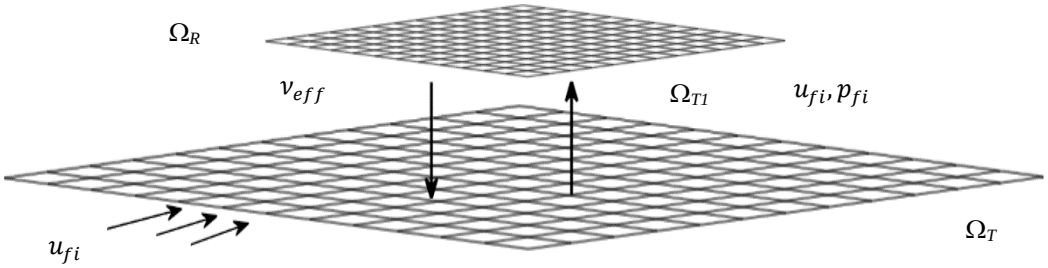

Figure 4.1.3 Sketch of the viscosity fields mapping order

By using this equation, the effective viscosity $\nu'(x,y,t)$ at Γ_c equal to the effective viscosity at the same location evaluated by the turbulence model in Ω_R, i.e. $\nu_{eff}(x,y,t)_{\Gamma c}$; it also changes gradually in x- and y-direction from the effective viscosity $\nu_{eff}(x,y,t)_{\Gamma c}$ at the boundary Γ_c to the molecular viscosity at the outer boundaries of the quasi-turbulent domain , ensuring a continuity of $\nu'(x,y,t)$ at Γ_c .

One may worry about the artificial assignment of $v'(x, y, t)$ in the quasi-turbulent model. In fact, such linear variation of the effective viscosity has been numerically observed in the region outside of the critical region, as evidenced by the preliminary investigation, presented in the previous chapter. Such equation stands if the domain Ω_R and Ω_{T1} are assigned to be consistent with the critical region. Furthermore, what is concerned in this problem is the overall solution in the area near the structure, i.e. Ω_R, where the correction of the solution is sought by using the residual turbulent model. The error caused by the minor incorrection of the effective viscosity in the quasi turbulent model can be corrected by the residual turbulent solver in the area one concerned.

Due to the fact that the computational mesh used in the quasi-turbulent domain is often different from that in the Ω_R. Specifically, in the overlapping region Ω_R and Ω_{T1}, the nodes in the mesh used by the quasi-turbulent model are not consistent with those used by the residual turbulent model as shown in Figure 4.1.2. A mapping of the effective viscosity is required by using the interpolation. The assignment of $v'(x, y, t)$ is conducted by three steps in sequence:

(i) mapping v_{eff} obtained by the turbulence model in the residual turbulent domain to that the nodal positions in Ω_{T1};

(ii) interpolation using $v_{eff}(x_{\Gamma c}, y, t) - \frac{v_{eff}(x_{\Gamma c},\mathrm{y},\mathrm{t})-v}{x_b - x_{\Gamma c}}(x - x_{\Gamma c})$ in Ω_{T2x} ;

(iii)interpolation using $v_{eff}(\mathrm{x}, y_{\Gamma c+}, \mathrm{t}) - \frac{v_{eff}(\mathrm{x},y_{\Gamma c+},\mathrm{t})-v}{y_{b+} - y_{\Gamma c+}}(y - y_{\Gamma c+})$ and $v_{eff}(x, y_{\Gamma c-}, \mathrm{t}) - \frac{v_{eff}(\mathrm{x},y_{\Gamma c-},\mathrm{t})-v}{y_{b-} - y_{\Gamma c-}}(y - y_{\Gamma c-})$ in Ω_{T2y+} and Ω_{T2y-}, respectively. One may find that in sub region of Ω_{T2y+} above Ω_{T2x}, $v_{eff}(\mathrm{x}, y_{\Gamma c+}, \mathrm{t})$ cannot be directly mapped from the solution in Ω_R. Similar issue is found in the sub region of Ω_{T2y-} below Ω_{T2x}. In these regions, $v_{eff}(x, y_{\Gamma c+}, t)$ and $v_{eff}(x, y_{\Gamma c-}, t)$ in Equation (4.1.18) are replaced by the corresponding values of $v'(x, y, t)$ obtained in step (ii), i.e. $v'(x, y_{\Gamma c+}, t)$ and $v'(x, y_{\Gamma c-}, t)$, respectively.

4.1.5 Updating computational mesh

In addition, the computational mesh needs to be adjusted at each time step to conform to the motion of the structure (ensuring the boundary of the structure surface Γ_{cs} to be consistent with the surface of the moving structure). For this purpose, the nodes on Γ_{cs} move together with the motion of the structure, i.e., their velocities are equal to the velocity of the moving boundary at the same points. After applying such condition, the velocities of other nodes are determined by the following diffusion equation.

$$\nabla \cdot (\gamma \nabla u_{bi}) = 0 \qquad (i = 1, 2) \tag{4.1.19}$$

where γ is the diffusion coefficient that is reflecting the resistance of the grid to be deformed. A quadratic distance-based diffusion parameter γ is applied here in order to maintain the mesh quality near the structure (Jasak & Tuković 2006). After the velocities of nodes being determined, the position of every node, x_i, are updated by

$$x_i^{N+1} = x_i^N + u_{bi}\Delta T \qquad (i = 1, 2) \tag{4.1.20}$$

where the superscript '*N* ' indicates n^{th} time step, while '*N+1*' refers to the next time step.

4.2 Methodology of hybrid method for multiphase flow

4.2.1 Volume fraction equation

Attempts to successfully simulate various multiphase flow situations have resulted in a variety of numerical approaches (Prosperetti & Tryggvason 2015). Among them, implicit interface capturing methods VOF proposed by Hirt & Nichols (1981) started a new trend in multiphase flow simulation. It relies on the definition of an indicator function, named volume fraction α. This function allows us to know whether the cell is occupied by the fluid or another, or a mix of both. The traditional way to track the free surface is accomplished by the solution of the volume fraction transport equation. It can be expressed as:

$$\frac{\partial \alpha}{\partial t} + u'_{Tj} \frac{\partial \alpha}{\partial x_j} = 0 \tag{4.2.1}$$

where U_T' represents the total velocity field. The volume fraction α take ranges from 0 to 1 (α = 0 for gas and $\alpha = 1$ for liquid).

A modification of the approach makes use of an artificial compression term, namely ($\nabla \cdot U_c\alpha(1-\alpha)$) (Weller, 2002) to replace the traditional compressing differencing scheme. This approach is conservative and takes non-zero values only at the interface. This yields the final expression:

$$\frac{\partial \alpha}{\partial t} + u'_{Tj}\frac{\partial \alpha}{\partial x_j} + u'_{Tcj}\frac{\partial \alpha(1-\alpha)}{\partial x_j} = 0 \tag{4.2.2}$$

in which u'_{Tc} is the artificial compressive velocity and

$$|\boldsymbol{U}_{TC}| = min[c_\alpha|\boldsymbol{U}_T|, max(|\boldsymbol{U}_T|)] \tag{4.2.3}$$

Accordingly, the gradients of the volume fraction are encountered only in the interfacial region between two fluids, i.e. near the free surface of the water in this study. The compression of the interface is controlled by c_α. This interface compression coefficient is constant at range [0, 2]. The boundedness of such equation is achieved by an especially designed solver called multi-dimensional universal limiter for explicit solution (MULES). A limiter factor is adopted on the fluxes of the discretised divergence term to ensure a final value between 0 and 1.

Two immiscible fluids are considered as one effective fluid throughout the domain, the physical properties of which are calculated as weighted averages based on the distribution of the liquid volume fraction, thus being equal to the properties of each fluid in their corresponding occupied regions and varying only across the interface, which is constructed as:

$$\rho = \rho_w\alpha + \rho_{air}(1-\alpha) \tag{4.2.4}$$

$$\mu = \mu_w\alpha + \mu_{air}(1-\alpha) \tag{4.2.5}$$

where μ_w and μ_{air} are densities and dynamic viscosity of water and air, respectively.

4.2.1.1 Governing equation for multiphase flow

Same to the governing equations for the one-phase flow problem, a finite-volume discretization is used with arbitrary Lagrangian-Eulerian (ALE) formulation to allow for moving and deforming grids. It is given by:

$$\frac{\partial \rho {u_{Tj}}'}{\partial x_j} = 0 \tag{4.2.6}$$

$$\frac{\partial \rho {u_{Ti}}'}{\partial t} + ({u_{Tj}}' - {u_{bi}}')\frac{\partial \rho {u_{Ti}}'}{\partial x_j} = \frac{\partial}{\partial x_j}\left[\mu_{eff}\left(\frac{\partial {u_{Ti}}'}{\partial x_j} + \frac{\partial {u_{Tj}}'}{\partial x_i}\right)\right] - \frac{\partial {p_{fT}}'}{\partial x_i} + \rho g + \sigma \kappa \nabla \alpha$$

$$(i = 1,2) \tag{4.2.7}$$

where ρ is density, $\mu_{eff}(x, y, t)$ is the effective dynamic viscosity, which takes into account the dynamic molecular viscosity plus the turbulent effects: $\mu_{eff} = \mu + \rho \nu_T(x, y, t)$. In the VOF simulation, the body forces include gravity (ρg) and surface tension effects ($\sigma \kappa \nabla \alpha$) at the interface. In which, σ is the surface tension coefficient, κ is the local interfacial curvature is obtained by the volume fractions as follows:

$$\kappa = -\nabla \cdot \left(\frac{\Delta \alpha}{|\Delta \alpha|}\right) \tag{4.2.8}$$

In the present VOF method, the normal component of the pressure gradient at a stationary wall, with a no-slip condition, must be different for each phase due to the hydrostatic component ρg when the phases are separated by the wall. In order to simplify the definition of boundary conditions, it is common to introduce the pseudo-dynamic pressure, p_d. The relationship between the pseudo-dynamic pressure and the pressure is as follows:

$$p_d = p - \rho g \cdot h \tag{4.2.9}$$

$$\nabla p_d = \nabla p - \rho g - g \cdot h \nabla \rho \tag{4.2.10}$$

The solution of the momentum equation is performed by constructing a predicted velocity field and then correcting it using the PISO (Issa 1986) implicit pressure correction procedure to time advance the pressure and velocity fields. The main procedure is the same as that of one phase solver, and the systematic derivation is outlined in Appendix D.

The boundary conditions (see Figure 4.2.1) for the original two-phase flow simulation is described in Table 4.2.1. From this table, one may notice that the main difference of the boundary condition configuration appears on the atmosphere boundary (Γ_A).

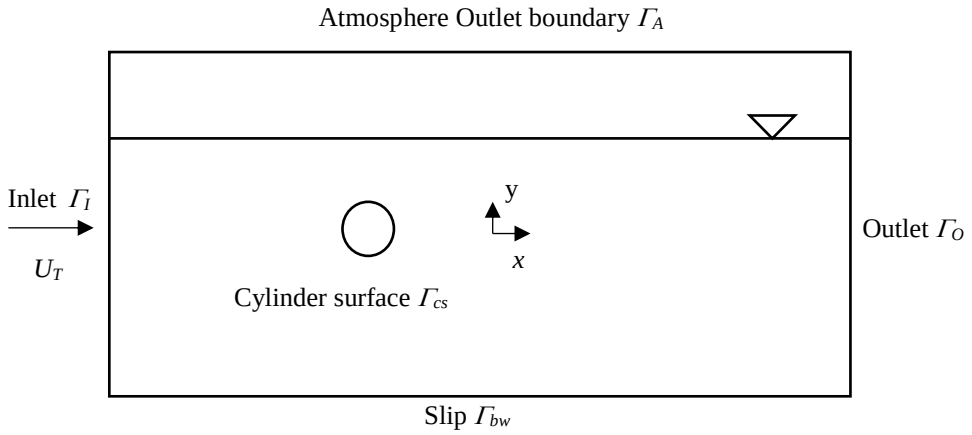

Figure 4.2.1 Sketch of the boundary conditions for the typical two-phase flow past a circular cylinder

Table 4.2.1 Boundary condition configuration

Boundaries	Velocity	Pressure	Alpha (α)
Inlet(Γ_I)	Fixed specific value/wave theory	Fixed pressure flux	Zero gradient
Outlet(Γ_O)	Zero gradient	Zero gradient	Zero gradient
Atmosphere (Γ_A)	Zero gradient	Given total pressure	Fixed value
Bottom(Γ_{bw})	Slip	Zero gradient	Zero gradient
Cylinder (Γ_{cs})	Fixed value	Zero gradient	Zero gradient

At the atmosphere boundary (Γ_A), for the incompressible flow, the static pressure stratifies,

$$P_P + \frac{1}{2}\left|U_p\right|^2 = P_0 \tag{4.2.11}$$

where P_P is the pressure at each atmosphere boundary patch; U_P is the velocity of the boundary patch; a zero-gradient velocity boundary condition is applied. For α, a fixed value zero is adopted.

At the inlet boundary (Γ_I), a modified pressure boundary condition is used where body forces, such as gravity, and surface tension are present. This boundary condition adjusts the pressure gradient which satisfies the pressure-velocity relation, i.e. the momentum equation, through the specified Dirichlet velocity boundary condition.

In this study, the structure is fully submerged in the fluid, i.e. air and water, the boundary condition on the structure surface is the same as that applied to the one-phase problems. Consequently, one can use the same numerical implementations for the structure surface boundary condition as that in the one-phase problems.

4.2.2 Functional decomposition in the multiphase hybrid model

Following the concept of the function splitting presented in Chapter 3, the quasi-turbulent model and the residual turbulent model for two-phase hybrid solver can be derived separately. The total velocity in this proposed hybrid method is constructed as Equation (4.2.12) and Equation (4.2.13),

$$u_{Ti}'(x,t) = u_{fi}'(x,t) + u_i^{*\prime}(x,t),\ (i=1,2) \tag{4.2.12}$$

$$p_T' = p_f'(x,t) + p^{*\prime}(x,t) \tag{4.2.13}$$

where the fields with the subscript *f* are the solutions of the quasi-turbulent model while these with superscript * are the residual solutions.

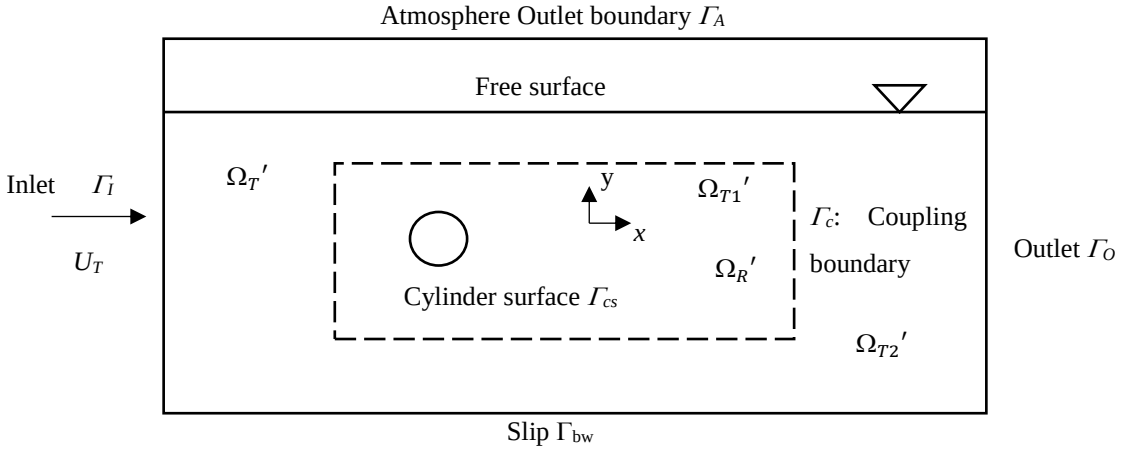

Figure 4.2.2 Sketch of the hybrid method computational domain with the presence of the free surface

The computational domain is illustrated in Figure 4.2.2, where Ω_T' is the entire domain in which the quasi-turbulent solutions are found. This domain is composed of two parts: $\Omega_T' = \Omega_{T1}' + \Omega_{T2}'$ as shown. Ω_{T1}' overlaps with the domain for the corresponding residual model, i.e. Ω_R'. Its boundary (Γ_c) is denoted by the dashed line.

The size of $\Omega_R{}'$ is the same as that of $\Omega_{T1}{}'$. But they are discretised into different meshes. Similar to the one phase hybrid solver, after applying the specific functional decomposition approach, the final solution is composed of two parts, for which (1) the quasi-turbulent solver is used to deal with $u_f{}'(x,t)$ and $p_f{}'(x,t)$; (2) the residual solver aimed to compute $u^{*\prime}(x,t)$ and $p^{*\prime}(x,t)$.

4.2.3 Multiphase quasi-turbulent model

In the quasi-turbulent model, $u_f{}'(x,t)$ and $p_f{}'(x,t)$ satisfy the following incompressible continuity and momentum equations, which are described as:

$$\frac{\partial \rho u_{fj}{}'}{\partial x_j} = 0 \tag{4.2.14}$$

$$\frac{\partial \rho u_{fi}{}'}{\partial t} + (u_{fj}{}' - u_{bi}{}')\frac{\partial \rho u_{fi}{}'}{\partial x_j} = \frac{\partial}{\partial x_j}\left[\mu'_{eff}\left(\frac{\partial u_{fi}{}'}{\partial x_j} + \frac{\partial u_{fj}{}'}{\partial x_i}\right)\right] - \frac{\partial p_f{}'}{\partial x_i} + \rho g + \sigma \kappa \nabla \alpha$$

$$(i = 1, 2) \tag{4.2.15}$$

$$\mu'_{eff} = \mu' + \rho \nu'(x,y,t) \tag{4.2.16}$$

Similar to the one-phase hybrid model, where $u_f{}'$ and $p_f{}'$ are the intimidate velocity and pressure fields; $\mu'_{eff}(x,y,t)$ is the effective dynamic viscosity. Compared to the momentum equation in the single-phase quasi-turbulent model, the main difference is body force term $\rho g + \sigma \kappa \nabla \alpha$ introduced in the right-hand side of Equation (4.2.15), which is evaluated by

$$\frac{\partial \alpha}{\partial t} + u'_{fj}\frac{\partial \alpha}{\partial x_j} + u'_{fcj}\frac{\partial \alpha(1-\alpha)}{\partial x_j} = 0 \tag{4.2.17}$$

in which

$$\left|\boldsymbol{U}'_{fC}\right| = min\left[c_\alpha \left|\boldsymbol{U}'_{\boldsymbol{f}}\right|, max(\left|\boldsymbol{U}'_{\boldsymbol{f}}\right|)\right] \tag{4.2.18}$$

where $\boldsymbol{U}'_{fC}$ is the artificial compressive velocity of the quasi-turbulent domain.

4.2.4 Multiphase residual turbulent model

Substituting Equation (4.2.12) and Equation (4.2.13) into the multiphase continuity equation (4.2.6) and momentum equation (4.2.7) to achieve the two-phase residual turbulent model, which can be expressed as:

$$\frac{\partial \rho u_j^{*\prime}}{\partial x_j} = 0 \tag{4.2.19}$$

$$\frac{\partial \rho u_i^{*\prime}}{\partial t} + (u_{fi}{}' + u_i^{*\prime} - u_{bi}{}') \frac{\partial \rho u_i^{*\prime}}{\partial x_j} = \frac{\partial}{\partial x_j} [\, \mu_{eff} \left(\frac{\partial u_i^{*\prime}}{\partial x_j} + \frac{\partial u_i^{*\prime}}{\partial x_i} \right)] - \frac{\partial p^{*\prime}}{\partial x_i} - S_f' \quad (i = 1, 2) \tag{4.2.20}$$

in which

$$S_f' = \frac{\partial \rho u_{fi}{}'}{\partial t} + (u_{fi}{}' + u_i^{*\prime} - u_{bi}{}') \frac{\partial \rho u_{fi}{}'}{\partial x_j} - \frac{\partial}{\partial x_j} \left[\mu_{eff} \left(\frac{\partial u_{fi}{}'}{\partial x_j} + \frac{\partial u_{fi}{}'}{\partial x_i} \right) \right] + \frac{\partial p_f{}'}{\partial x_i} + \rho g + \sigma \kappa \nabla \alpha \tag{4.2.21}$$

After solving the Equation (4.2.14) to Equation (4.2.15), the intermediate velocity and pressure fields $u_f{}'$ and $p_f{}'$ are known. Therefore, the right-hand side term S_f' can be treated as the explicit term providing an appropriate prediction of $u_i^{*\prime}$. All other terms, such as the temporal term, convection and diffusion term and source term, are treated same as in the one phase hybrid solver. It shall be noted that in the hybrid multi-phase model, the volume fraction α is solved in the quasi-turbulent domain. One may also introduce a similar residual equation to correct the solutions of the transportation Equation (4.2.17) in $\Omega_R{}'$. The numerical validation shown in the following chapter suggests that the present treatment can lead to satisfactory solution for the problem considered in this thesis, partially due to the fact that the non-breaking water wave, so does the volume fraction, is dominated by the gravity. However, if a breaking wave is involved in the future study, the turbulence may significantly affect the wave propagating, and thus a correct of the volume fraction shall be implemented.

4.2.5 Turbulent viscosity treatment in multiphase model

Similar to the single-phase turbulent viscosity transformation, the assignment of $\mu'(x, y, t)$ is conducted by three steps in sequence (see Figure 4.2.3):

(i) transform μ_{eff} obtained by the turbulence model in the residual turbulent domain to that the nodal positions in $\Omega_{T1}{}'$;

(ii) interpolation using $\mu_{eff}(x_{\Gamma c}, y, t) - \frac{\mu_{eff}(x_{\Gamma c}, \mathrm{y}, \mathrm{t}) - \mu}{x_b - x_{\Gamma c}} (x - x_{\Gamma c})$ in $\Omega_{T2x}{}'$;

(iii)interpolation using $\mu_{eff}(x, y_{\Gamma c+}, t) - \frac{\mu_{eff}(x,y_{\Gamma c+},t)-\mu}{y_{b+}-y_{\Gamma c+}}(y - y_{\Gamma c+})$ and $\mu_{eff}(x, y_{\Gamma c-}, t) - \frac{\mu_{eff}(x,y_{\Gamma c-},t)}{y_{b-}-y_{\Gamma c-}}(y - y_{\Gamma c-})$ in $\Omega_{T2y+}{}'$ and $\Omega_{T2y-}{}'$, respectively. (see Equation (4.2.22))

$$\mu'(x,y,t) = \begin{cases} \mu_{eff}(x,y,t) & \Omega_{T1} \\ \mu_{eff}(x_{\Gamma c}, y, t) - \dfrac{\mu_{eff}(x_{\Gamma c}, y, t) - \mu}{x_b - x_{\Gamma c}}(x - x_{\Gamma c}) & \Omega_{T2x} \\ \mu_{eff}(x, y_{\Gamma c+}, t) - \dfrac{\mu_{eff}(x, y_{\Gamma c+}, t) - \mu}{y_{b+} - y_{\Gamma c+}}\left(y - y_{\Gamma c+}\right) & \Omega_{T2y+} \\ \mu_{eff}(x, y_{\Gamma c-}, t) - \dfrac{\mu_{eff}(x, y_{\Gamma c-}, t) - \mu}{y_{b-} - y_{\Gamma c-}}\left(y - y_{\Gamma c-}\right) & \Omega_{T2y-} \end{cases} \quad (4.2.22)$$

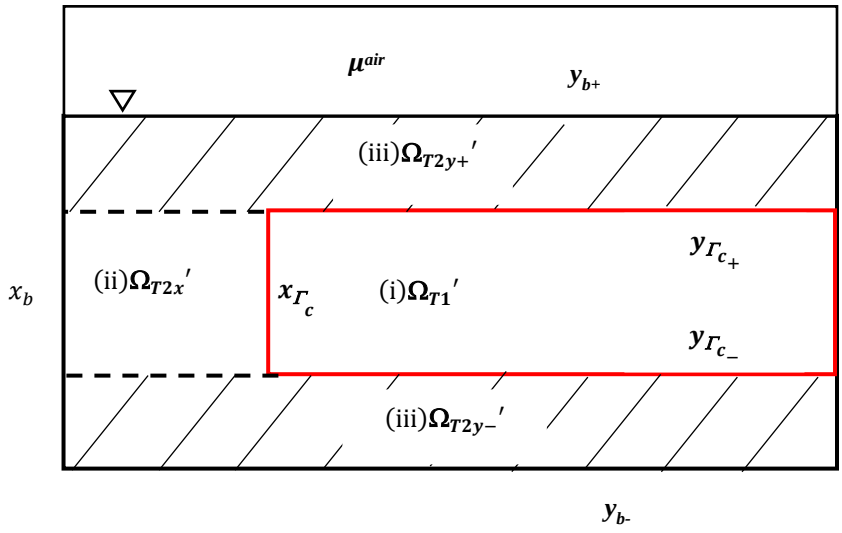

Figure 4.2.3 Sketch of the viscosity fields mapping order for the multiphase solver

5

NUMERICAL IMPLEMENTATION

In the above chapters, the methodologies and important techniques, such as the domain decomposition/specification, boundary coupling and turbulent viscosity transformation, which required in the hybrid method, have been discussed. In this chapter, the details of how the hybrid solver methodology is implemented in the open source OpenFOAM is presented for both single-phase and multiphase flows.

5.1 Techniques of sub-cycle strategy

A key motivation of the hybrid method development is to improve the simulation efficiency for turbulent flow. This target is accomplished by the application of the numerical strategy related to the time step. It is understood that the quasi-turbulent model does not require to solve the turbulent model to acquire the effective viscosity (a formula is suggested to directly estimate it using that predicted in the subdomain for the residual turbulent model) and, therefore, may use coarser mesh resolution compared to the residual turbulent model in the same area near the structure. If the same *Co* is used by both the quasi-turbulent model and the residual turbulent model, the time step requirements for two models are different. The former requires longer time step size (in some case, it is several times of that required by the latter. As indicated in the section

of introduction, compared with the RANS without turbulent model, achieving convergent solutions for the turbulent model, such as the k-ω SST, requires a reduction of the mesh size and time step size at a scale of $Re^{-\frac{3}{4}}$ and $Re^{-\frac{1}{2}}$, respectively. Greater the Reynolds number is, more significant the reduction is. Taking *Re* = 100 as example, solving RANS with turbulent model requires 10% of the time step size for the corresponding RANS without turbulent model. Analogically, one may see a similar difference of the spatial-temporal resolutions (mesh size and time step size) between the quasi-turbulent model, where the turbulent model is not required to be solved, and the residual model, in which *k-ω* SST model is used to resolve the turbulent viscosity. One may use the same time step, i.e. that required by the residual turbulent model, the overall computational efficiency might be relatively low. Before the flow chart of the algorithm and numerical procedure for the hybrid method are presented, the strategy for optimising the time step is introduced. This is referred to as the sub-cycle strategy.

In the proposed sub-cycle strategy, the sub iterative is conducted for the residual solver. This means that within each step of the quasi-turbulent simulation, one needs to conduct *N* steps of the simulation of the residual solver in its domain. Considering the same Courant number (*Co*) being applied, the time steps required by the quasi-turbulent model and the residual model are $(C_o\Delta L)/U_{max}$and $(C_o\Delta L)/U^*_{max}$ respectively, where ΔL and Δl are the minimum mesh sizes in the quasi-turbulent domain and the residual field domain, respectively; U_{max} and U^*_{max} are the maximum velocity magnitude estimated by quasi-turbulent model and the residual model, respectively. Generally speaking, the maximum velocities estimated by two solvers is close. Therefore, the ratio of the time step size for the quasi-turbulent model against that for the residual model is $(U_{max}\Delta L)/(U^*_{max}\Delta l) \approx \Delta L/\Delta l$. For this reason, it is suggested that the sub-cycle number Ns can be selected by

$$Ns = Int\ (\Delta L/\Delta l) \tag{5.1.1}$$

As the increase of the sub-cycle number Ns, it is expected to see a more significant improvement of the computational efficiency of the present hybrid model, compared to the conventional solver. It shall be noted that the minimum mesh size in the current simulation often occur near the structure surface. No matter the mesh is moving or stationary, the ratio $\Delta L/\Delta l$ does not change considerably. Due to this, the sub-cycle

number Ns may only be determined once in the beginning of the simulation after the meshes are generated.

5.2 Numerical procedure for single-phase hybrid solver

After the application of the sub-cycle strategy, the whole framework of the hybrid model is clear. The flow chart of the algorithm is shown in the following Figure 5.2.1.

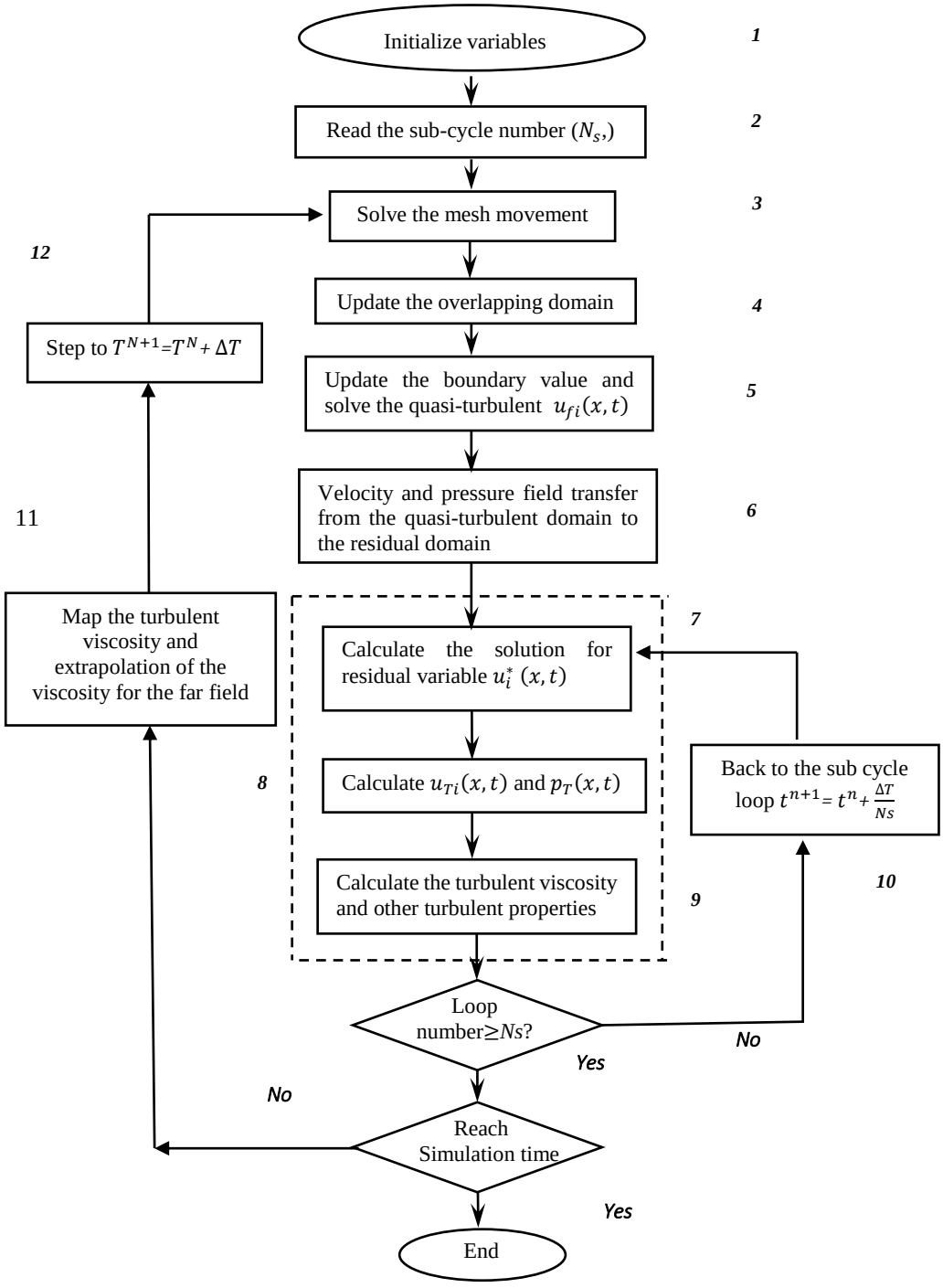

Figure 5.2.1 Flow chart of the hybrid model algorithm

1. Initialize all the variables in the first step.
2. Determine the sub-cycle number (N_s).
3. Move the mesh in the quasi-turbulent domain to conform to the motion of the structure using Equations (4.1.19) and (4.1.20).
4. Calculate the nodal velocities for the mesh used by the residual turbulent model by interpolating the corresponding values in the quasi-turbulent domain, which has been achieved in Step 3.
5. Update the boundary conditions, Equations (4.1.7) to (4.1.10), where the velocity of the structure is required for specifying the structure surface boundary condition; Solve the quasi-turbulent model, i.e. Equation (4.1.5) and (4.1.6), to obtain u_{fi} and p_f .
6. Feed the quasi-turbulent solutions, i.e. u_{fi} and p_f, to the centres of every cell in the computational mesh for the residual solver using numerical interpolation.
7. Solve the residual turbulent model, i.e. Equations (4.1.11) and (4.1.12) with the corresponding boundary conditions, i.e. Equations (4.1.14) to (4.1.17).
8. Sum the residual and quasi-turbulent field to obtain the overall flow fields u_{Ti} and p_T, in the residual domain using Equations (4.1.3) and (4.1.4).
9. Calculate the turbulent viscosity in the residual domain using k-ω SST model and update the effective viscosity in the residual domain using Equation (3.2.3).
10. Go to Step 7, until the number of the sub-cycle steps reaches prescribed number *Ns*.
11. Map the effective viscosity from the residual turbulent domain to the overlap zone of the quasi-turbulent domain using numerical interpolation; Use Equation (4.1.18) to specify the effective viscosity for the quasi-turbulent model;
12. Go to Step 2 for the next time step, until the simulation is terminated.

Both the quasi-turbulent and the residual turbulent models are solved by using the finite volume method. In the finite volume discretization, all the physical quantities are cell centred. The Pressure Implicit with Splitting of Operators (PISO) algorithm (Issa 1986; Ferziger & Peric 2012) is used to decouple the velocity pressure relation.

5.3 Numerical procedure for multiphase hybrid solver

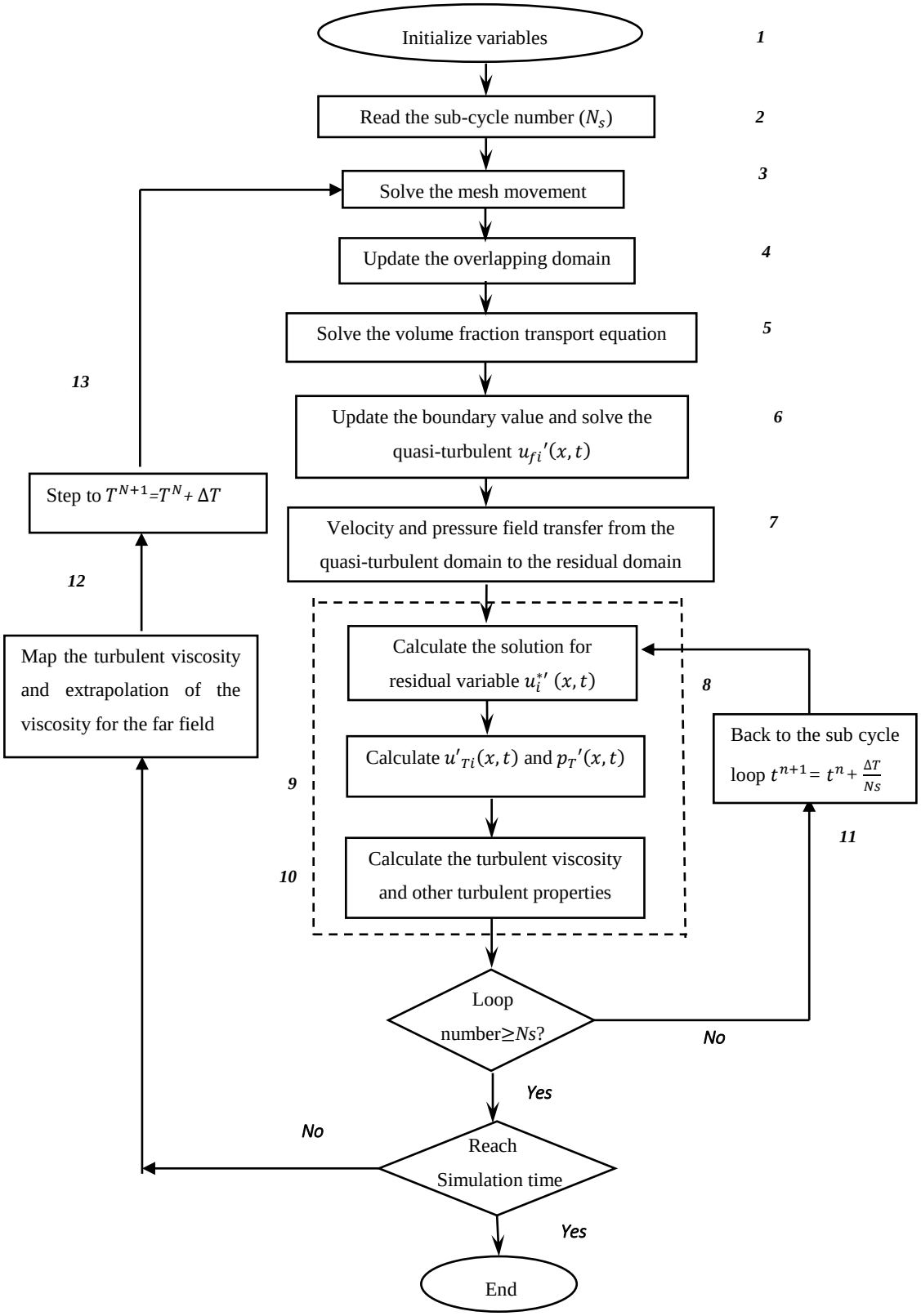

Figure 5.3.1 Flow chart for the two-phase hybrid solver algorithm

The flow chart showing the numerical procedure of the multiphase hybrid model is illustrated in Figure 5.3.1. Compared with the corresponding procedure for the single-phase flow, additional steps are introduced to treat the free surface. In the procedure, Steps 7 and 12 related to the transformation of the variable ($\mu_{eff,}$ u'_{fi} and p_{fi}') between the two domains Ω_R' and Ω_T'.

1. Initialize of all the variables in the first step.
2. Determine the sub-cycle number (N_s).
3. If a moving structure is involved, the dynamic mesh technique shall be applied at prior using Equations (4.1.19) and (4.1.20) for moving the mesh in the quasi-turbulent domain, and the nodal velocity is transferred to the residual domain to update the mesh in the residual domain.
4. Calculate the nodal velocities for the mesh used by the residual turbulent model by interpolating the corresponding values in the quasi-turbulent domain, which has been achieved in Step 3.
5. Solve the volume fraction transportation Equation (4.2.17) in the quasi-turbulent domain.
6. Solve the quasi-turbulent model, Equations (4.2.14) and (4.2.15) to obtain u_{fi}' and p_f' in which the effective viscosity is evaluated using Equation (4.2.22) at prior.
7. Feed the quasi-turbulent solutions, i.e. obtain u_{fi}' and p_f', to the centres of every cell in the computational mesh for the residual solver using numerical interpolation.
8. Solve the residual turbulent model, i.e. Equations (4.2.19) and (4.2.20) with the corresponding boundary conditions.
9. Sum the residual and quasi-turbulent field to obtain the overall flow fields u_{Ti} and p_T, in the residual domain using Equations (4.2.12) and (4.2.13).
10. Calculate the turbulent viscosity in the residual domain using k-ω SST model and update the effective viscosity in the residual domain using Equation (4.2.16).
11. Go to Step 8, until the number of the sub-cycle steps reaches prescribed number N_s.

12. Map the effective viscosity from the residual turbulent domain to the overlap zone of the quasi-turbulent domain using numerical interpolation; Use Equation (4.2.22) to specify the effective viscosity for the quasi-turbulent model;
13. Return to Step 2 for the next time step.

5.4 Finite volume method of governing equations

Within the above numerical procedures, both the quasi-turbulent and residual turbulent model in either the Eulerian form or the ALE form of the governing equations are solved by using the finite volume method (FVM) in the OpenFOAM framework. Details can be found in the relevant user manual of OpenFOAM or relevant references. Only a summary is given below. For clarity, these equations are rewritten to be vector form, where U and U^* are the velocity vectors used by the quasi-turbulent model and the residual turbulent model, respectively. Accordingly, p and p^* are used to replace the pressure in the quasi-turbulent model and the residual turbulent model, respectively. The governing equations are discretized using the finite-volume method for the temporal, convection and Laplacian term with corresponding discretisation schemes. For clarity, only the incompressible momentum equation, which is given in Equation (5.4.1) in a vector form, for the incompressible flow is given as an example.

$$\frac{\partial U}{\partial t} + \nabla \cdot (U \otimes U) = -\nabla p + [\nabla \cdot (\nu \nabla U) + \nabla U \cdot \nabla \nu] \tag{5.4.1}$$

in which the viscous term, ν is the kinematic viscosity,

$$\nabla \cdot (\nu \nabla U + U^T) = \nabla \cdot (\nu \nabla U) + \nabla U \cdot \nabla \nu \tag{5.4.2}$$

Integration of each term in Equation (5.4.1) over the volume corresponding to a computational cell (Ω_i). This yields the equation given by

$$\int_{\Omega_i} \left[\frac{\partial U}{\partial t} + \nabla \cdot (U \otimes U) - \nabla \cdot (\nu \nabla U) - \nabla U \cdot \nabla \nu\right] d\Omega = -\int_{\Omega_i} \nabla p \, d\Omega \tag{5.4.3}$$

The integration of the left side of the equation can be rewritten to

$$\int_{\Omega_i}\left[\frac{\partial U}{\partial t}+\nabla\cdot(U\otimes U)-\nabla\cdot(\nu\nabla U)-\nabla U\cdot\nabla\nu\right]d\Omega \tag{5.4.4}$$

$$=\int_{\Omega_i}\frac{\partial U}{\partial t}\,d\Omega+\int_{\partial\Omega_i}(U\otimes U)\cdot n\;dS-\int_{\partial\Omega_i}(\nu\nabla U)\cdot n\;dS$$

$$-\int_{\Omega_i}\nabla U\cdot\nabla\nu\;d\Omega$$

The interested cell is identified by the subscript *P*, as shown in Figure 5.4.1. Its neighbour is *N*. *f* is the face between *P* and *N* is owned by *N;* length *d* is distance between the centre of the cell *P* and cell *N*, S_f is the face area vector of the cell *P*, which is the product of the outward unit normal vector of the face *f* and the surface area of the face *f*.

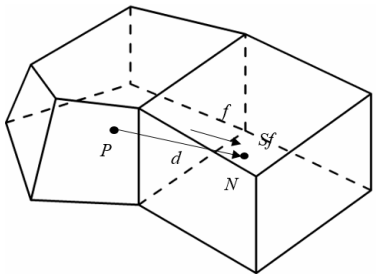

Figure 5.4.1 The face *f* whose owner is *P* and neighbour *N*

where the Gauss theorem is used, and the volume integration is transferred to the surface integration over the surface of the cell $\partial\Omega_i$. According to the Rhie & Chow approach (Rhie, *et al.*, 1982), the pressure term in the right hand side of Equation (5.4.3) is not integrated directly but is replaced by a guessed value, i.e.

$$\frac{U_P^r-U_P^n}{\Delta t}\Omega_P+\sum_{f\in\partial\Omega_i}\phi_f^n\,U_f^{r\prime}-\sum_{f\in\partial\Omega_i}\nu_f^{n+1}\left(\nabla\frac{1}{f}U\right)^{r'}\left|S_f\right|-\nabla U_P^n\cdot\nabla\nu_p^{n+1}\Omega_P$$

in which the integration is conducted; superscripts *n* and *n+1* represent the values at n^{th} and $(n+1)^{\text{th}}$ time step, respectively. U_P^r and U_P^n are the intermediate velocity and the velocity at the n^{th} time step for the cell *P*, ϕ_f^n is the flux of surface *f* at the n^{th} time step, $U_f^{r\prime}$ is the intermediate velocity on the face *f* of the cell *P*; ν_f^{n+1} is the kinematic viscosity on the face *f* of the cell *P* at $(n+1)^{\text{th}}$ time step, $\left(\nabla\frac{1}{f}U\right)^{r'}$ is the surface gradient operator $\nabla\frac{1}{f}$ act on *U*, ν_p^{n+1} is the kinematic viscosity at the centre of the cell *P* at new time step

$(n+1)$, Ω_P is the volume of the cell *P*. It is noted that the pressure value will be corrected after the velocity is sought here using the PISO approach. Eventually, one can rewrite Equation (5.4.3) as

$$\int_{\Omega_i} \frac{\partial U}{\partial t}\, d\Omega + \int_{\partial\Omega_i} (U \otimes U)\cdot n\; dS - \int_{\partial\Omega_i} (\nu \nabla U)\cdot n\; dS - \int_{\Omega_i} \nabla U \cdot \nabla \nu\; d\Omega$$
$$= \frac{U_P^r - U_P^n}{\Delta t}\Omega_P + \sum_{f\in\partial\Omega_i} \phi_f^n\, U_f^{r\prime} - \sum_{f\in\partial\Omega_i} \nu_f^{n+1} \left(\nabla \frac{1}{f} U\right)^{r'} |S_f| - \nabla U_P^n \cdot \nabla \nu_p^{n+1} \Omega_P \tag{5.4.5}$$

For simplification, a linear interpolation scheme is applied here. The intermediate velocity of the face f is linearized as

$$U_f^{r\prime} = \frac{U_P^r}{2}[1 + \Theta(f)] + \frac{U_N^m}{2}[1 - \Theta(f)] \tag{5.4.6}$$

where

$$\Theta(f) = \begin{cases} 1 & \text{for } P \text{ is the owner for face } f \text{ and } N \text{ is the neighbor} \\ -1 & \text{for } N \text{ is the owner for face } f \text{ and } P \text{ is the neghbor} \end{cases}$$

and *m* is the inner iteration number of the PISO procedure. For the diffusive term, the face gradient discretisation is implicit when the length vector *d* between the centre of the cell *P* and cell *N* is orthogonal to the face plane, e.g.

$$\left(\nabla \frac{1}{f} U\right)^{r'} |S_f| = \Theta(f) \frac{U_N^m - U_P^r}{|d|} |S_f| \tag{5.4.7}$$

where $|d|$ is the distance between the centre of cell *P* and the centre of cell *N* (see Figure 5.4.1). In the case of non-orthogonal meshes, an additional explicit term is applied but not presented here to save the space.

Substituting Equations (5.4.6) and (5.4.7) to Equation (5.4.5), it yields

$$A_P U_P^r = \left(\sum_{\forall N} A_N U_N^m + E_P^n\right) = H(U^m) \tag{5.4.8}$$

the parameters A_P, A_N and E_P^n given as:

$$E_P^n = \frac{U_P^n}{\Delta t} + \nabla U_P^n \cdot \nabla \nu_p^{n+1} \tag{5.4.9}$$

$$A_P = \left(\frac{\Omega_P}{\Delta t} + \sum_{f\in\partial\Omega_i} \frac{1}{2}\phi_f^n [1 + \Theta(f)] + \sum_{f\in\partial\Omega_i} \nu_f^{n+1}\, \Theta(f) \frac{|S_f|}{|d|}\right) \frac{1}{\Omega_P} \tag{5.4.10}$$

$$A_N = \left(-\frac{1}{2}\phi_f^n [1 - \Theta(f)] + \nu_f^{n+1} \Theta(f) \frac{|S_f|}{|d|} \right) \frac{1}{\Omega_P} \tag{5.4.11}$$

Because the volume flux $\phi_f^n = (U_P^r)_f \cdot S_f$ and thus,

$$\phi_f^r = \left(\frac{H(U^m)}{A_P} \right)_f \cdot S_f \tag{5.4.12}$$

Equation (5.4.12) completes the predictor step. However, the pressure contribution is not considered until now, after the discretisation the pressure can be treated as follows:

$$\left(\frac{-\nabla p}{A_P} \right)_f \cdot S_f = -\left(\frac{1}{A_P} \right)_f \left(\nabla \frac{1}{f} P^{m+1} \right) |S_f| \tag{5.4.13}$$

The above equation can be rewritten as

$$\phi_f^{m+1} = \phi_f^r - \left(\frac{1}{A_P} \right)_f \left(\nabla \frac{1}{f} P^{m+1} \right) |S_f| \tag{5.4.14}$$

To solve the pressure field p^{m+1}, the law of mass conservation is imposed for the incompressible medium, which is given as

$$\sum_{f \in \partial \Omega_i} \phi_f^{m+1} = 0 \tag{5.4.15}$$

Then, substituting (5.4.14) to (5.4.15), it leads to

$$\sum_{f \in \partial \Omega_i} \left(\frac{1}{A_P} \right)_f \left(\nabla \frac{1}{f} P^{m+1} \right) |S_f| = \sum_{f \in \partial \Omega_i} \phi_f^r \tag{5.4.16}$$

Equation (5.4.16) results in a linear system for P^{m+1}, and can be solved using the preconditioned conjugate gradient (PCG) method. Besides PCG, OpenFOAM provides various other options such as preconditioned biconjugate gradient, generalized geometric–algebraic multi-grid and other smooth solvers, which uses a smoother for convergence (Greenshields 2017). After P^{m+1} is updated using Equation (5.4.16), flux at $(m+1)^{\text{th}}$ iteration step can be calculated at each face by using Equation (5.4.14). The cell centred velocity fields U_p^{m+1} are obtained by reconstructing the face velocity flux using the following expression:

$$U_p^{m+1} = U_P^r + \frac{1}{A_P}\left(\sum_{f\in\partial\Omega_i}\frac{(S_f \otimes S_f)}{|S_f|}\right)^{-1} \cdot \left(\sum_{f\in\partial\Omega_i}\left(\frac{\phi_f^{m+1} - (U_P^r)_f \cdot S_f}{\left(\frac{1}{A_P}\right)_f}\right)\frac{S_f}{|S_f|}\right) \tag{5.4.17}$$

PISO iteration is performed by changing the superscript m to $(m+1)$and updating $H(U_m)$ in Equation (5.4.8) with the velocity obtained from Equation (5.4.17), and solving the equations through Equation (5.4.17), thereby updating P, ϕ_f and U. This procedure is repeated several times to ensure that the velocity and pressure field together satisfy both continuity and momentum equations. At the end of the iteration procedure, the values corresponding to the M th iteration are assigned to the corresponding values at the new time step $(n+1)$,

$$\phi_f^{n+1} = \phi_f^M, U^{n+1} = U^M \text{ and } P^{n+1} = P^M \tag{5.4.18}$$

5.5 Numerical implementation of the boundary conditions

In conjunction with the governing equations, the boundary conditions are required to construct a well-posed mathematical model. This section gives the numerical implementations. Details of how two types of boundary conditions can be built into the algebraic equations are demonstrated. It is important to note that the following numerical implementations can be applied by both the Quasi-turbulent model and the residual turbulent model. Consider the discretisation of the convection and diffusion terms integrated over a control volume and linearized, results in

$$\int_\Omega \nabla\cdot(u\phi)d\Omega = \sum F_f\,\phi_f \tag{5.5.1}$$

$$\int_\Omega \nabla\cdot(\nu\nabla\phi)d\Omega = \sum \nu\, S_A\cdot(\nabla\phi)_f \tag{5.5.2}$$

where the value of a property per unit mass is denoted by ϕ, quantities evaluated at the faces are subscripted by *f*, the face flux F_f assigned by $S_A \cdot u_f{}^{N-1}$.

5.5.1 Dirichlet boundary condition

The Dirichlet boundary condition prescribes the value of ϕ_f at the boundary face f equal to ϕ_b. With respect to the convection term, it can be specified by

$$\int_{\Omega} \nabla \cdot (u^* \phi) d\Omega = \sum_{f \in \partial\Omega_i} F_f \phi_f = \sum_{f \in \partial\Omega_i} F_{nb} \phi_{nb} + \sum_{f \in \partial\Omega_i} F_b \phi_b \tag{5.5.3}$$

where the subscript b and nb denote the boundary faces and non-boundary faces, respectively. For the diffusion term, in which v is the dynamic viscosity of the flow. The face gradient at the boundary face is calculated from the known values at the boundary and the centre of the cell using

$$\int_{\Omega} \nabla \cdot (v \nabla \phi) d\Omega = \sum_{f \in \partial\Omega_i} v\, S_A \cdot (\nabla \phi)_f = \sum_{f \in \partial\Omega_i} v |S_A| \cdot \left(\frac{\phi_b - \phi_P}{|d|}\right) \tag{5.5.4}$$

5.5.2 Neumann boundary condition

For a Neumann boundary condition, the gradient with respect to the unit normal vector of the boundary face is prescribed and numerically implemented using

$$\frac{\phi_b - \phi_P}{|d|} = gb \tag{5.5.5}$$

For the convection term, ϕ_b can be updated by the value at the centre of the cell and the given gradient *gb*, i.e.

$$\int_{\Omega} \nabla \cdot (u^* \phi) d\Omega = \sum_{f \in \partial\Omega_i} F_{nb} \phi_{nb} + \sum_{f \in \partial\Omega_i} F_b (gb|d| + \phi_P) \tag{5.5.6}$$

For the diffusion term, the dot product between the face area vector and $(\nabla\phi)$ is known. This results in

$$\int_{\Omega} \nabla \cdot (v \nabla \phi) d = \sum_{f \in \partial\Omega_i} v\, S_A \cdot (\nabla \phi)_f = \sum_{f \in \partial\Omega_i} v\, S_A \cdot (\nabla \phi)_{nb} + \sum_{f \in \partial\Omega_i} v\, S_A \cdot gb \tag{5.5.7}$$

6

VALIDATION OF THE HYBRID MODEL

A thorough investigation of the hybrid solver proposed in this thesis is conducted, which includes (1) verification tests for the stationary circular cylinder exposed to the laminar and turbulent flows, (2) examinations of the oscillating circular cylinder undergoing various combinations of (*Re, A/D, Fr*) for the laminar and turbulent flows. With respect to (1) and (2), the simulation results of the hybrid model are compared to that of the original RANS solver, and other available experimental observations data. Such data are well documented, e.g., by both physical experiments (Zdravkovich, 1990; Norberg, 1998; 2003b; Norberg, 2003a; Lin, *et al.*, 1995) and numerical simulations (Park, *et al.*, 1998; Bardina, *et al*., 1997; Rahman, *et al*., 2007; Ünal, *et al.*, 2010; Menter, 1994; Ong, *et al.*, 2009; Stringer, *et al.*, 2014; Selvam, 1997).

6.1 Validation of the single-phase hybrid solver

In this subsection, the performance of the single-phase hybrid solver is investigated. Two situations are considered, for flow passing either a stationary or an oscillating cylinder. In the numerical studies, the optimal domain size is generally the balance

between the accuracy and efficiency. The required minimum domain size depends on the factors like flow property, Reynolds number, domain shape and the boundary conditions. The position of the boundaries (see Figure 6.1.1) should be designed carefully, and attention should be paid to: (1) the distance from the inlet boundary to the cylinder axis (D_{in}), (2) the distance from the cylinder axis to the outlet boundary (D_{out}), and (3) the cross-flow direction distance (D_{Tr}). Due to the nature of this proposed hybrid method, the computational domain size for the quasi-turbulent domain is same to that of the original RANS solver while the overlapping domain can be smaller. The position of truncation should be determined in such a way that the resulted computational domain of the residual solver is as small as possible.

The size of computational domain (as shown in Figure 6.1.1) should be large enough so that the artificially-added boundaries, such as inlet and outlet, do not considerably affect computational results, but it should be kept as small as possible to save computational time. Many suggestions have been made on how to determine the size of computational domain. Sohankar, *et al*. (2003b) investigated the minimum D_{in} for the flow around a square-section cylinder at *Re* =100 by using original RANS solver, and they found that D_{in} should be at least ten times larger than the characteristic length of the cylinder (diameter D). With respect to D_{Tr}, Barkley and Henderson (1996) found that D_{Tr} ≥44D was necessary at *Re*=190. Blackburn and Henderson (1999) also used a domain of D_{Tr} =30D in the simulation for an oscillating cylinder at *Re*=500, meanwhile Stringer *et al.* (2014) used a rectangular domain of D_{Tr} =40D for a large range of Reynolds number. In this study, pre-tests are performed by using a rectangular domain with D_{Tr} range from 20D to 40D based on the original RANS solver, and it is found that the solution is not considerably affected only when D_{Tr} ≥32D. When determining the downstream size D_{out} one should ensure that the vortexes are fully developed (Stringer, *et al.*, 2014). Considering the experience given in the reference and based on our own tests (the results are not presented here for saving the space), $D_{out} \geq 40$D is required. Taking all the factors into account, a domain size of 32D×60D is adopted in this study with D_{Tr} =32D, $D_{in} = 20$ and $D_{out} = 40$.

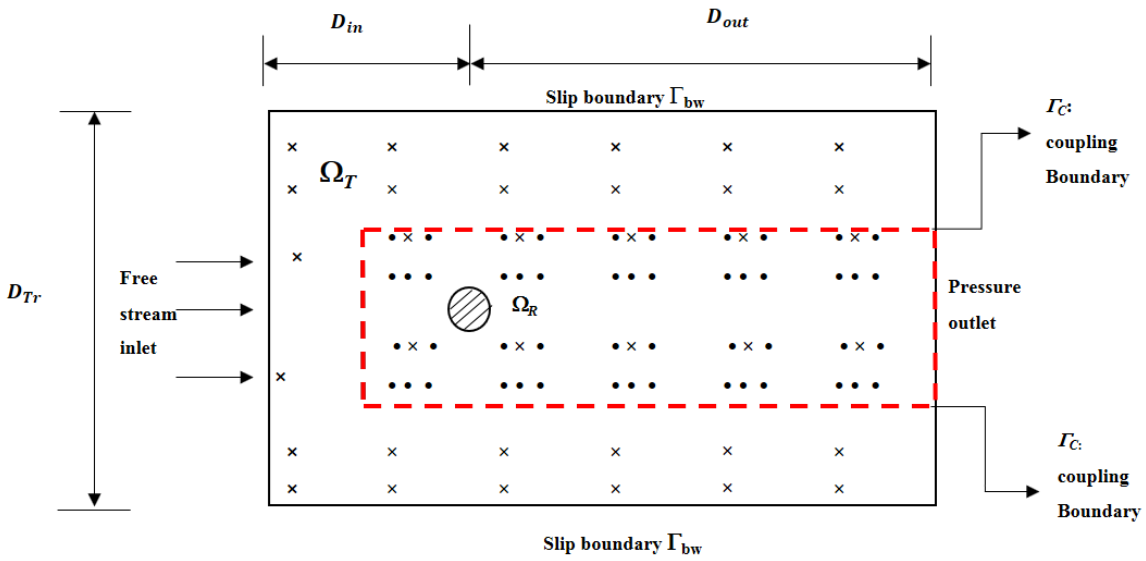

Figure 6.1.1 Sketch of two overlapping meshes (• denotes the cell centre of the truncated overlapping domain mesh; × denotes the cell centre of the quasi-turbulent domain with a coarse mesh)

The results from the hybrid method will be compared with those from the original RANS method. For this purpose, the meshes for both methods are required. For the original method, the outmost circular grid line has a diameter of 3D~4D, depending on if the cylinder is stationary or moving. The thickness of first layer of grids near the cylinder surface is determined by $\Delta L_{min} = 2 * (v_{eff}\ y^+/u_*)$, where u_* is the frictional velocity near the cylinder surface, v_{eff} is the local kinematic viscosity of the fluid and the value of y^+ is chosen as 1.0 in this study. The thickness of the grid layers beyond the first layer is specified by $\delta^{l-1}\Delta L_{min}$, where δ is an expanding factor and *l* refers the layer concerned, e.g., *l*=2 for the second layer from the cylinder surface. According to the numerical tests, δ = 1.1 ~1.2. If δ >1.2, the error is too large while the computation costs too much time if δ <1.1 on the other hand. During the generation of mesh, the aspect ratios of all elements are controlled to be less than 5, where the aspect ratio is defined as the ratio of the largest length to the shortest length of an element.

The mesh for the hybrid method include two parts. The first part covers the overlapping domain (Ω_R) for finding the residual solutions. This part of the mesh is the same as that for the original RANS method in the same area (Ω_{T1}). The second part is the mesh for the quasi-turbulent domain which has the same size as the domain for the original method. The mesh structure of this part is the same as that for the original RANS method but the mesh size is equal to N_s multiplying the mesh size of the latter, so coarser than the former. Figure 6.1.2 shows the mesh for the hybrid method.

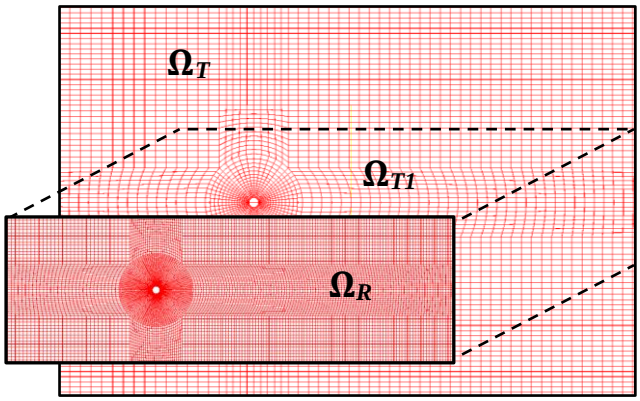

Figure 6.1.2 Sketch of the block mesh configuration for both the quasi-turbulent and the overlapping domains

6.1.1 Validation of flow past a stationary circular cylinder

Firstly, the hybrid solver in this study is validated by simulating a stationary circular cylinder in the flow at Re=1000 and 10000. For the turbulent flow of Re=1000 and 10000, to deal with the turbulent viscosity, the k-ω SST turbulence model is employed following the test result in Chapter 3 and studies by Rahman, *et al.* (2007), Ünal, *et al.* (2010), Stringer, *et al.* (2014) and Robert & Zang (2012). In addition, the same wall boundary treatment method is applied to both the original and hybrid solver. An example of the hybrid solver simulation procedure is given in Figure 6.1.3. Figure 6.1.3. (a) illustrates the velocity field simulated using the quasi-turbulent model in the entire computational domain(Ω_T). The residual velocity field is captured by the residual turbulent model in a truncated domain(Ω_R) in Figure 6.1.3 (b). At the same time, the two-way transformation of the eddy viscosity and quasi-turbulent velocity and pressure

field conducted. The summing of the quasi-turbulent model solution and that of the residual turbulent model leads to the complete solution of the turbulent flow (see Figure 6.1.3 (c)).

The key parameters such as $C_{L\,rms}$, $\overline{C_D}$ and S_t are examined in the validation, where $C_{L\,rms}$ means the root mean square of the lift coefficient, $\overline{C_D}$ is the average value of the drag coefficient, S_t is the strouhal number. The results are presented in Table 6.1.1 and Table 6.1.2. It is found that $C_{L\,rms}$, $\overline{C_D}$ and S_t computed by the hybrid model agree well with that of the original RANS solver. For example, in the case of *Re*=1000 (see Table 6.1.1), the disparity for $C_{L\,rms}$, $\overline{C_D}$ and *St* between the two solvers are 3.6%, 0.2% and 0.5%, respectively. For the case *Re*=10000 (see Table 6.1.2), the relative error of 0.2%, 1.8% and 1.5%, are found for $C_{L\,rms}$, $\overline{C_D}$ and S_t, respectively. Therefore, it can be concluded that the hybrid solver can provide satisfactory results for the cases studies so far. It also indicates that even with a truncated computational domain for the turbulent solver, this hybrid solver can provide solutions with the enough accuracy.

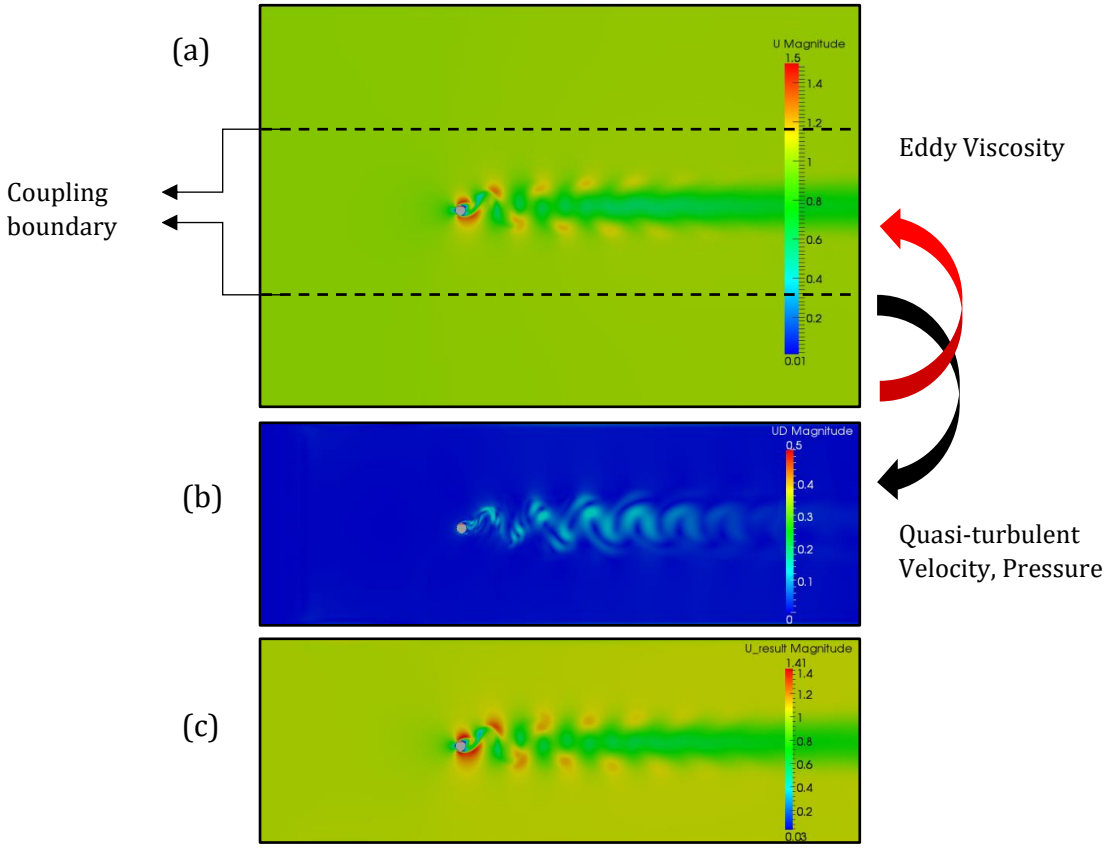

Figure 6.1.3 Procedure of the vortex shedding simulation using the hybrid method

Table 6.1.1 Disparity between the two solvers under *Re*=1000

	(Mesh number, *Co*)	$C_{L\,rms}$	$\overline{C_D}$	*St*
Original solver solution	(197400, 0.3)	0.56	1.019	0.201
Hybrid solver solution	(196792, 0.3)	0.58	1.020	0.202
Disparity (%)		3.6%	0.2%	0.5%

Table 6.1.2 Disparity between the two solvers under *Re*=10000

	(Mesh number, *Co*)	$C_{L\,rms}$	$\overline{C_D}$	*St*
Original solver solution	(1340496. 0.3)	0.639	1.11	0.203
Hybrid solver solution	(1338075. 0.3)	0.6402	1.09	0.206
Disparity (%)		0.2%	1.8%	1.5%

6.1.2 Validation of flow past an oscillating circular cylinder

In this section, the validation of the hybrid model for simulating the controlled vibrating circular cylinder in flow are carried out, where the prescribed transverse oscillation of the cylinder is given as in Equation (3.4.1). Firstly, the case with *Re*=185 is performed, *Fr* is ranging from 0.8 to 1.2 with *A/D* is 0.2 and 0.4, respectively. The lift and drag coefficients for case *A/D*=0.2 and *Fr*=0.9 are depicted in Figure 6.1.4, which shows a good agreement between the hybrid model and original RANS solver. Additionally, comparisons of $\overline{C_D}$ and $C_{L\,rms}$ between the hybrid model and the original RANS solver are given in Table 6.1.3, in which the satisfactory results are achieved with a maximum error of 4%. Comparison of another case with a larger amplitude ratio (*Re, A/D, Fr*) = (185, 0.4, 0.9) is also conducted, as shown in Table 6.1.4. Both $\overline{C_D}$ and $C_{L\,rms}$ from the two solvers suggest a good agreement with the relative errors are 2.2% and 0.87%, respectively.

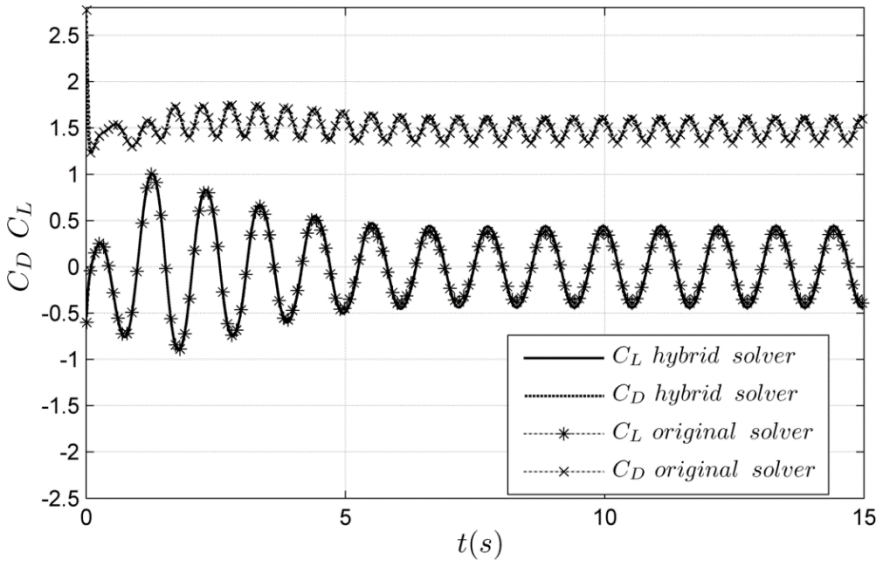

Figure 6.1.4 Time histories of drag and lift coefficients at *Re*=185 with *A/D* =0.2 and *Fr*=0.9

Table 6.1.3 Comparison between the hybrid model and original RANS solver for the case (*Re, A/D, Fr*) = (185, 0.2, 1.2)

	(Mesh number, *Co*)	$C_{L\,rms}$	$\overline{C_D}$
Original solver solution	(124600, 0.4)	0.96	1.372
Hybrid solver solution	(99236, 0.4)	0.92	1.35
Disparity (%)		4%	1.6%

Table 6.1.4 Comparison between the hybrid model and original RANS solver for the case (*Re, A/D, Fr*) = (185, 0.4, 0.9)

	(Mesh number, *Co*)	$C_{L\,rms}$	$\overline{C_D}$
Original solver solution	(189464, 0.4)	0.1546	1.695
Hybrid solver solution	(181616, 0.4)	0.158	1.68
Disparity (%)		2.2%	0.87%

A further comparison of $\overline{C_D}$ and $C_{L\,rms}$ between the hybrid model and original RANS solver in Pham, *et al.* (2010) are presented. $\overline{C_D}$ and $C_{L\,rms}$ as a function of frequency ratio ranging from 0.8 to 1.2 are depicted in Figure 6.1.5 and Figure 6.1.6 with two oscillation amplitudes (A/D=0.2 and A/D=0.4), respectively. It can be observed that for both low (A/D=0.2) and high (A/D=0.4) amplitudes, there are big variations of the force coefficients with the increase of the *Fr*. This trend indicates that the lift amplitude and phase is dominated by the frequency ratio while less related to the amplitude ratio. In addition, for both studied cases, $\overline{C_D}$ is not that sensitive to transition frequency (F_T) and have a wide peak around the transition frequency. However, $C_{L\,rms}$ experience a dramatic jump around the transition frequency which is around 1.0 in this case. The maximum difference between the two data sets with respect to A/D=0.2 are 8.1% and 7.2% at Fr=1.1 for $\overline{C_D}$ and $C_{L\,rms}$, respectively. While for the cases A/D=0.4, the maximum disparities are 7% and 0.2% for $\overline{C_D}$ and $C_{L\,rms}$ at Fr=1.1, respectively.

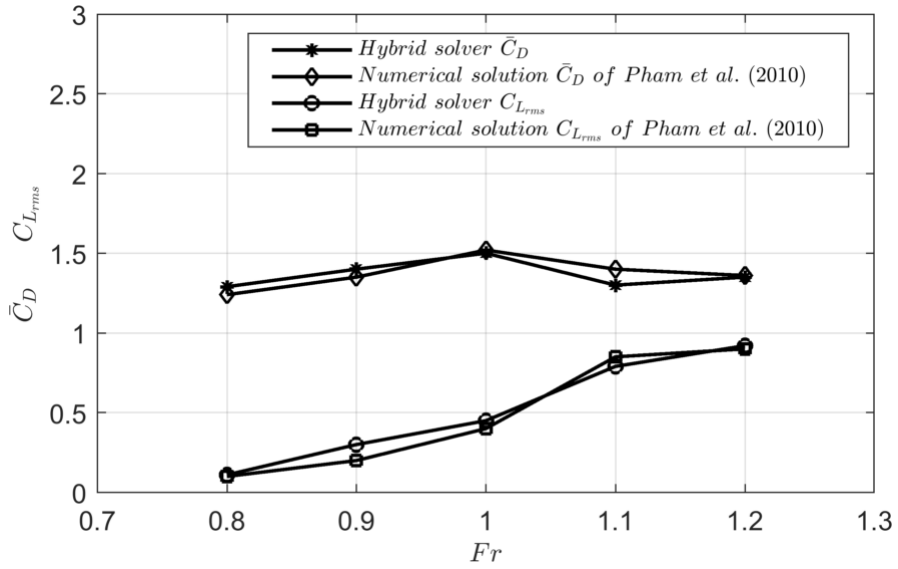

Figure 6.1.5 Comparison of $\overline{C_D}$ and $C_{L\,rms}$ between the hybrid model and original RANS solver for A/D=0.2

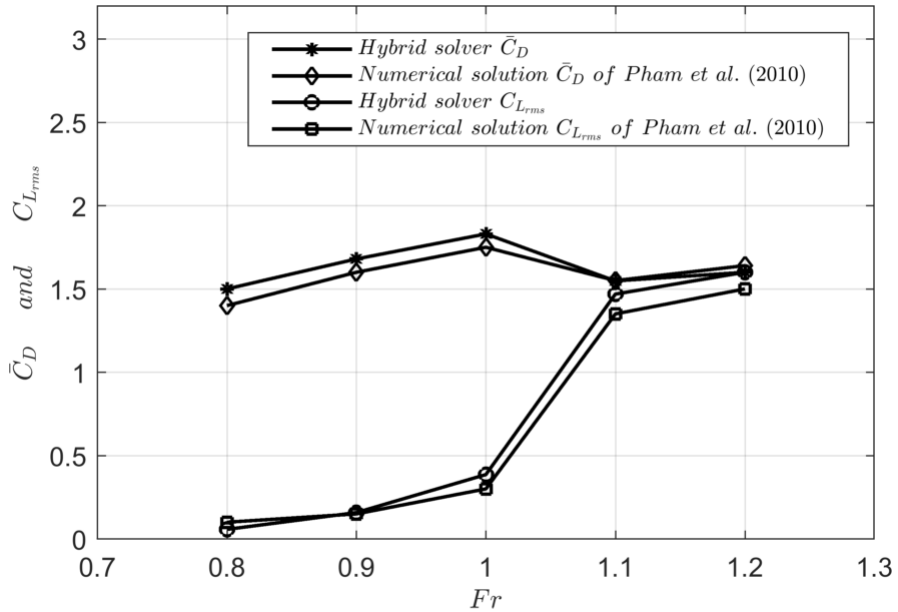

Figure 6.1.6 Comparison of $\overline{C_D}$ and $C_{L\,rms}$ between the hybrid model and original RANS solver for A/D=0.4

Secondly, the cases with higher Reynolds number of *Re*=1000 and *Re*=2300 are considered. Time histories of drag and lift coefficients are exhibited for (*Re, A/D, Fr)* = (1000, 0.2, 1.1) in Figure 6.1.7 and Figure 6.1.8, which demonstrates a good agreement between the two solvers.

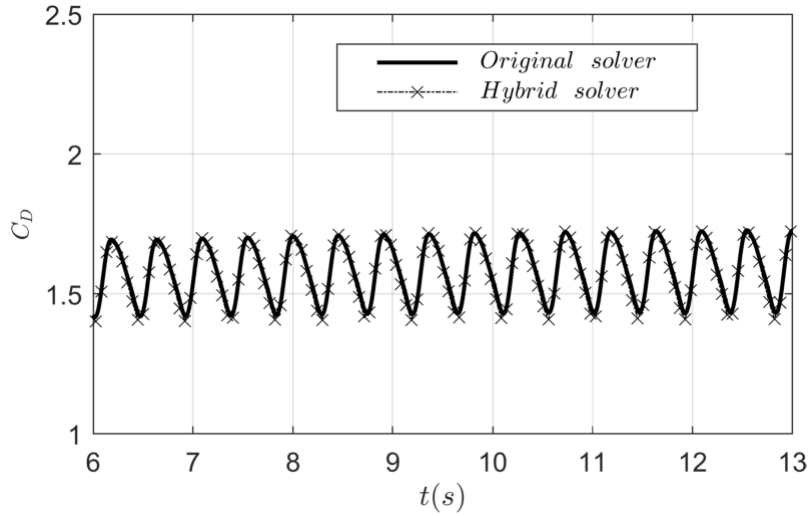

Figure 6.1.7 Time histories of drag coefficients with *Fr*=1.1 and *A/D*=0.2 at *Re*=1000

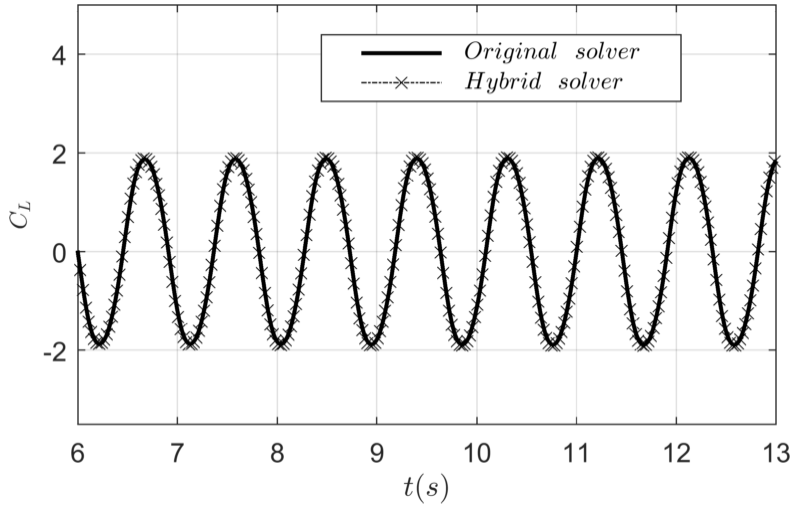

Figure 6.1.8 Time histories of lift coefficients with *Fr*=1.1 and *A/D*=0.2 at *Re*=1000

The disparities between results of the two solvers are given in Table 6.1.5 and Table 6.1.6, in which the maximum disparities are 1% and 3.4% for $C_{L\,rms}$ and $\overline{C_D}$ at (*Re, A/D, Fr*) = (1000, 0.2, 1.1) and (2300, 0.2, 08), respectively. All these

comparisons suggest that the hybrid solver is accurate enough for simulating flow passing an oscillating cylinder.

Table 6.1.5 Comparison between the hybrid model and original RANS solver for the case (*Re, A/D, Fr)* = (1000, 0.2, 1.1)

	(1000, 0.2, 1.1)		
	(Mesh number, *Co*)	$C_{L\,rms}$	$\overline{C_D}$
Original solver solution	(442288,0.2)	1.398	1.579
Hybrid solver solution	(419870,0.2)	1.412	1.593
Absolute disparity (%)		1%	0.88%

Table 6.1.6 Comparison between the hybrid model and original RANS solver for the case (*Re, A/D, Fr*) = (2300, 0.2, 08)

	(2300, 0.2, 08)		
	(Mesh number, *Co*)	$C_{L\,rms}$	$\overline{C_D}$
Original solver solution	(897866,0.2)	0.28	1.1
Hybrid solver solution	(884410,0.2)	0.29	1.077
Absolute disparity (%)		3.4%	2.1%

Furthermore, the results obtained by using the hybrid model are compared to the experimental data from Carberry *et al*. (2005), as shown in Figure 6.1.9 and Figure 6.1.10. The biggest difference between the results of the experiment and the present hybrid model appears at *Fr*=1.0 with a disparity of 13% for the lift coefficient, while 11% for drag coefficient at *Fr*=0.9. The reason that the maximum difference arises around *Fr*=0.9~1.0 is that the frequency transition occurs and the unstable flow may affect both the accuracy of the numerical results and experimental measurements.

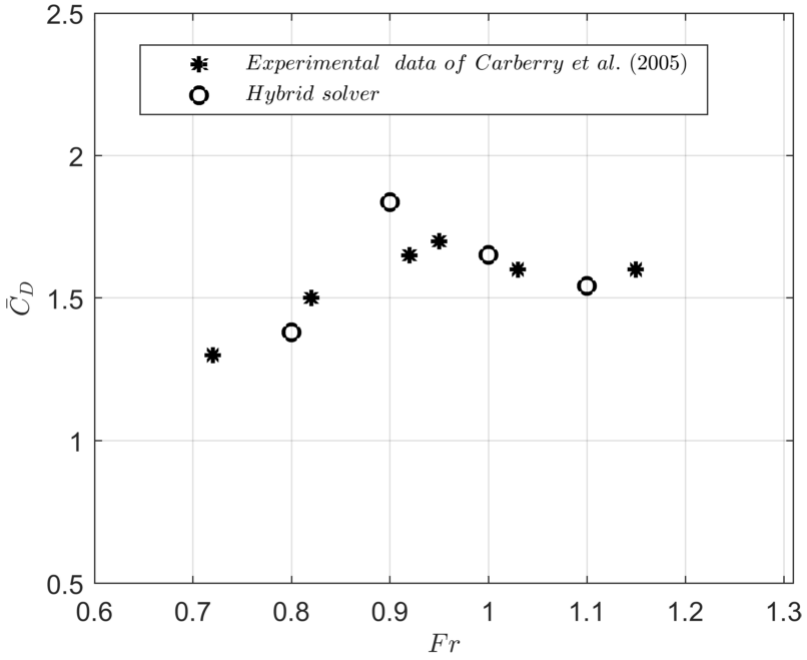

Figure 6.1.9 Comparison of $\overline{C_D}$ as a function of Fr

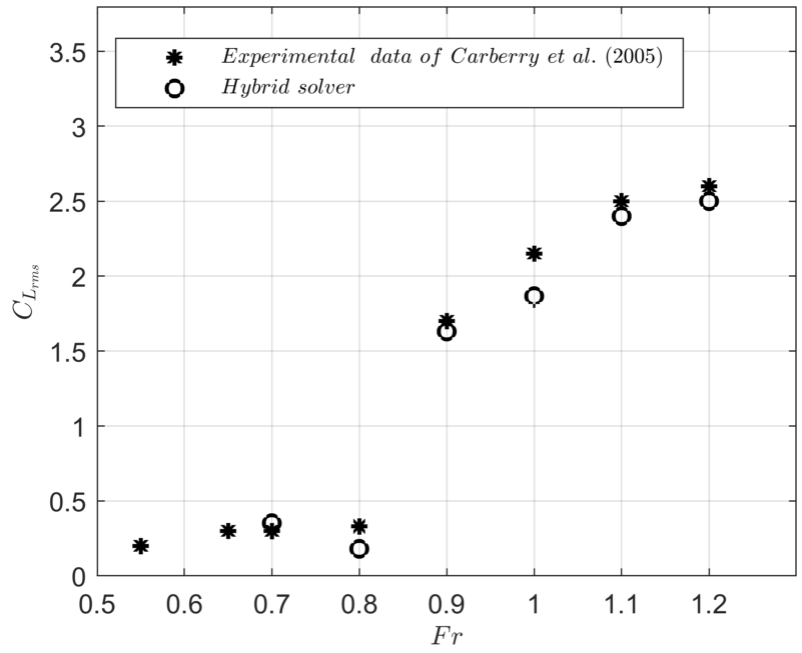

Figure 6.1.10 Comparison of $C_{L\,rms}$ as a function of F_r

6.1.2.1 Validation in frequency domain

To find the frequency of the vortex shedding, the power spectra of the time histories of C_L at different *A/D* and *Fr* are displayed in Figure 6.1.11. In the cases of *Fr* = 0.8, 0.9 and 1.0 (see Figure 6.1.11 (a), (b) and (c)), the frequency corresponding to the peak of the power spectra of C_L in the figure (denoted by f_s) is shown to be the same as that of the cylinder oscillating frequency. While after it exceeds the transition frequency, the spectra broaden and side bands emerged due to nonlinearities (see Figure 6.1.11(d) and (e)). Same spectra analysis results have been found by Pham, *et al.* (2010). This observation also validated the hybrid solver from the spectra domain point of view.

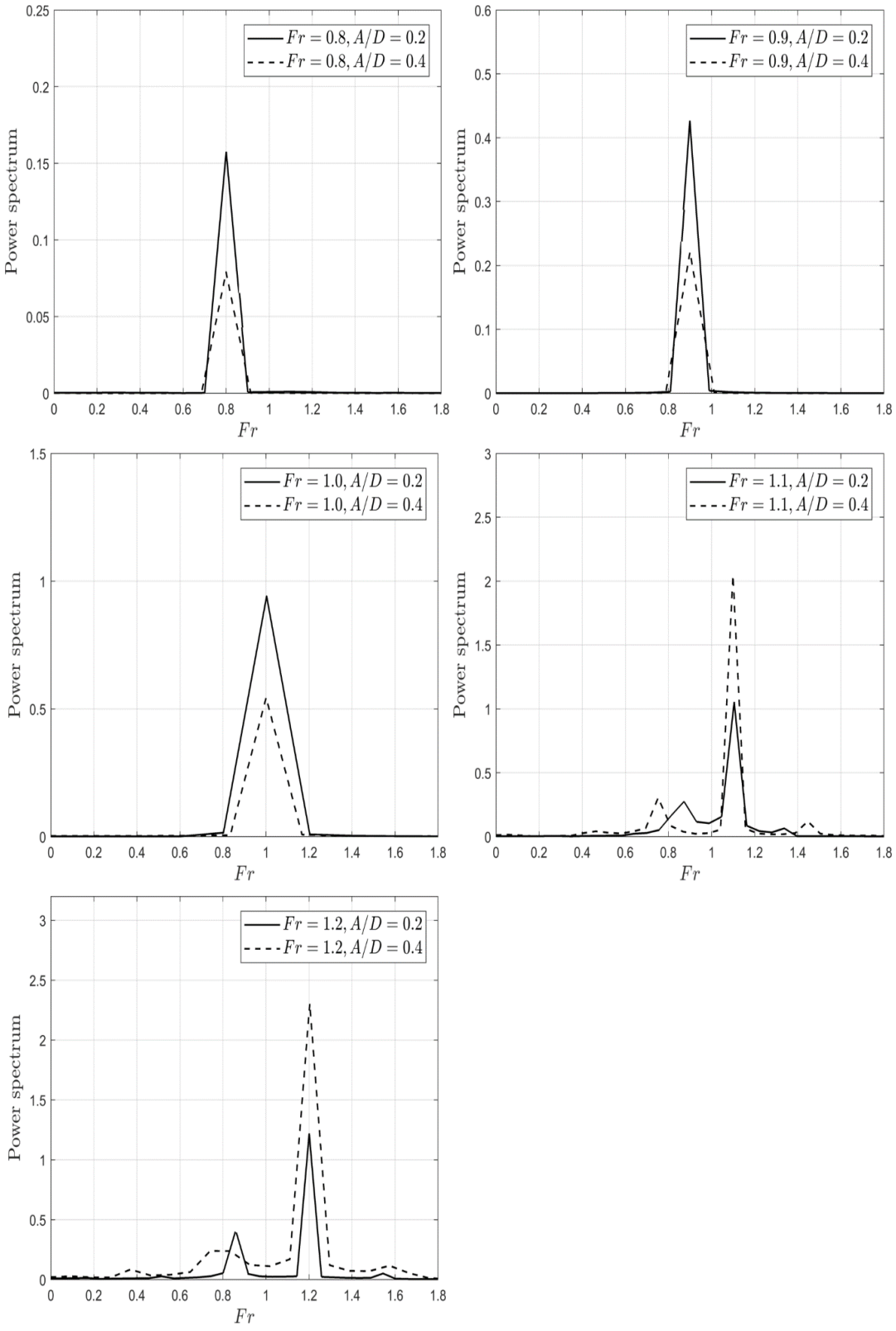

Figure 6.1.11 Power spectra of C_L for: (a) Fr =0.8, (b) Fr =0.9, (c) Fr =1.0, (d) Fr =1.1, (e) Fr =1.2

6.1.2.2 Vortex street behaviour and weak instability

The change of the wake mode is believed closely linked to the forces shift (Blackburn & Henderson, 1999; Williamson & Roshko, 1988; Carberry *et al*., 2004). Hence, an accurate representation of the crucial features of the wake mode is desired. This section highlights the comparison of the hybrid model result and the experimental data regarding the wake mode. The hybrid model is also capable of capturing the details of the development of the wake shedding during the oscillation period. The wake shedding mode is represented by plotting the instantaneous vorticity contours. The red colour denotes the positive vorticity while the negative vorticity is in blue.

Figure 6.1.12 and Figure 6.1.13 show the instantaneous vorticity contours when the cylinder is at different positions (see (a)-(b)-(c)-(d)) during one oscillation period. In Figure 6.1.12, two vortices are generated per oscillation cycle which is represent the high-frequency stage, this *2S* mode shed a positive vorticity structure to the near wake, and the attached vorticity wraps tightly around the base of the cylinder. In the *2P* mode, two vortex pairs are formed per cycle with long attached shear layers (see Figure 6.1.13). This stage is corresponding to the low-frequency stage whose vortex shedding phase is different to that of *2S* mode which shedding a negative shedding in the near wake. The changing of the wake mode is linked to the shift of the lift phase and amplitude. A dramatic increase of the lift coefficient can be observed when comparing Figure 6.1.12 (e) and Figure 6.1.13 (e). The same wake feature is also captured by the DPIV data of Govardhan & Williamson (2000) and RANS model simulation by Pan *et al*. (2007).

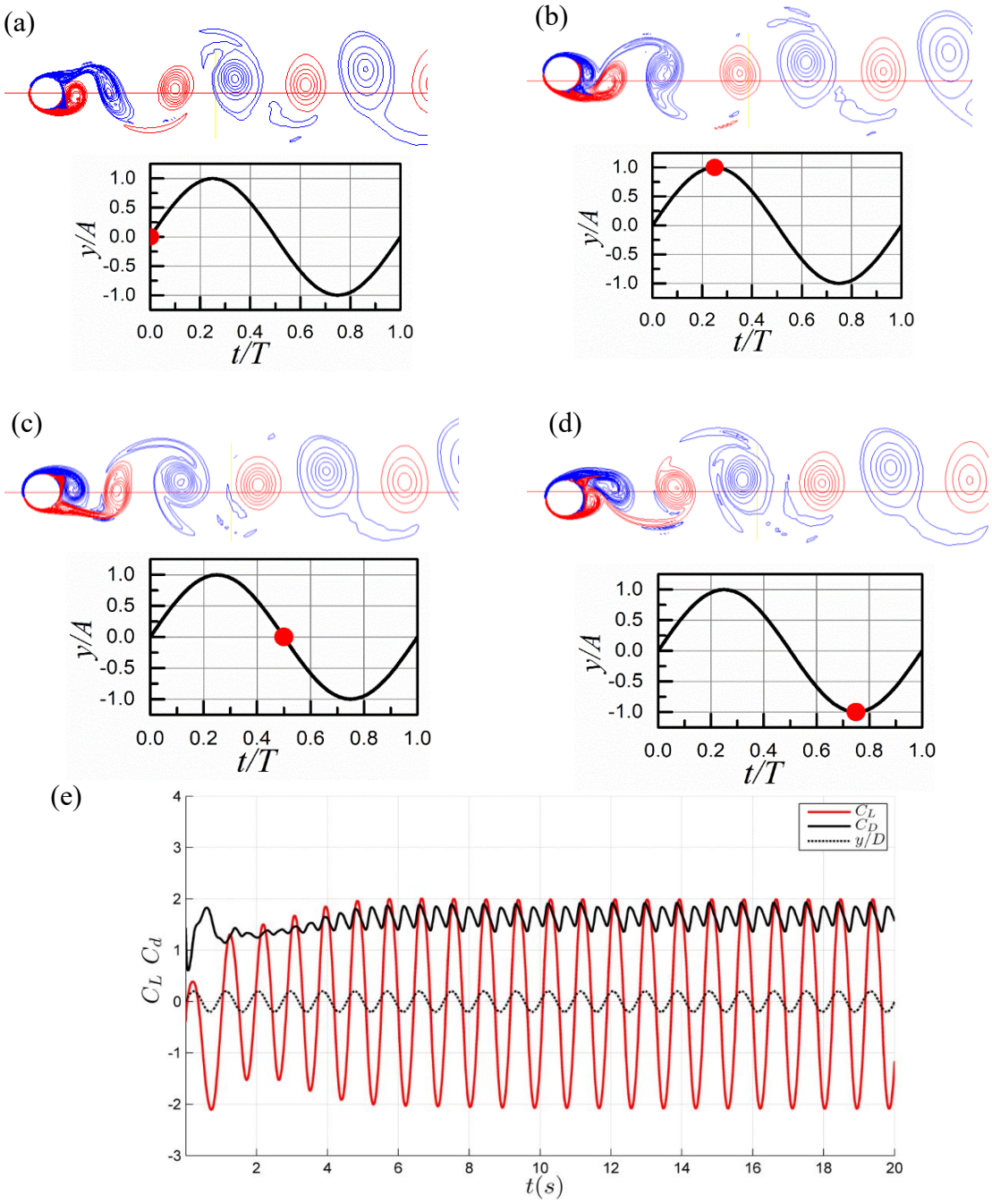

Figure 6.1.12 Instantaneous vorticity contours in one period (from (a) to (d)) for cases at low-frequency stage with a *2S* mode; (e) time history of lift and drag coefficient for the same case

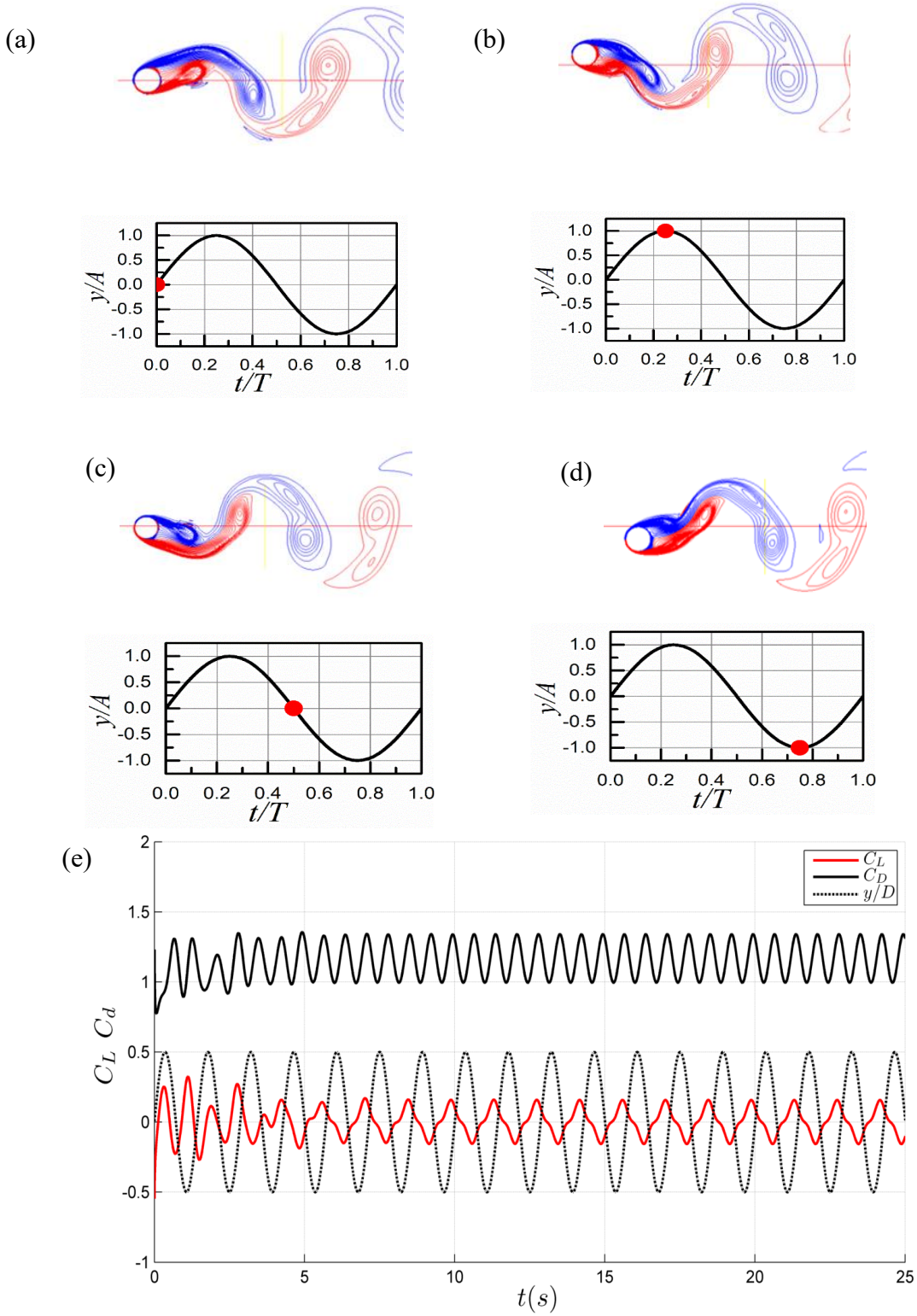

Figure 6.1.13 Instantaneous vorticity contours in one period (from (a) to (d)) for cases at low-frequency stage with a *2P* mode; (e) time history of lift and drag coefficient for the same case

6.2 Validation of the multiphase hybrid solver

The case studied in this section is the interaction between a horizontal submerged cylinder and regular surface waves. The validations of the multiphase hybrid solver are carried out by comparing its results with both experimental data (Conde *et al*., 2009) and numerical simulation solution (Teixeira 2009).

In this studied case, the diameter of the cylinder is 0.05m, which is horizontally placed at x_c=0 with its axis placed at a depth of 0.015m. Under this condition, the submergence gap ratio between the water level and the cylinder surface is equal to *3D*. In the numerical wave tank, the circular cylinder is located 2m away from inlet wave generation and 3.6m from the outlet boundary. The total length of the numerical tank is 5.6m with the water depth is 0.425m. The locations of four gauges (x-x_c)/λ are equal to -0.503, 0.0692, 0.509 and 1.264. The wave parameters used in the investigation are given by table 6.2.1.

Different configuration of the domain size, mesh number and absorption zone size are considered (see Table 6.2.2) in the convergence tests. The 2nd setup (30 cells per wave height and 80 cells per wave length with the absorption zone is $L' = 1.2\lambda$) is adopted in the following simulation which is found to be less expensive while can maintain good accuracy. The courant number for both the volume fraction equation and the momentum equation are set as 0.25. For validation purpose, the size of the overlapping domain is the same with the quasi-turbulent domain to explore the accuracy, but will be reduced later to test the efficiency of the hybrid solver.

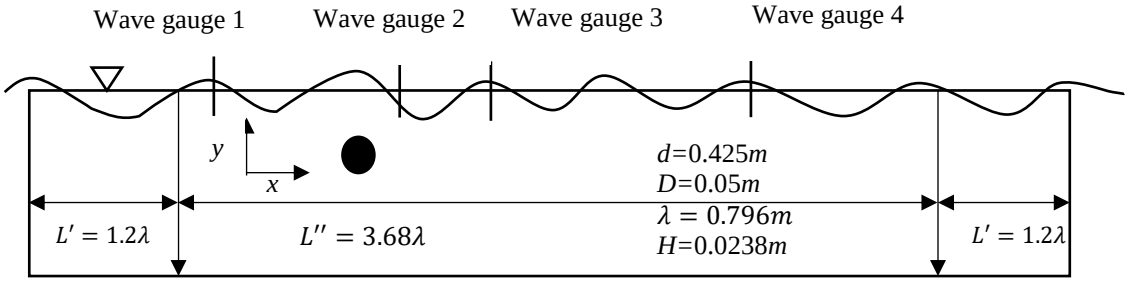

Figure 6.2.1 Configuration of the numerical wave tank

Table 6.2.1 Wave parameters

Wave parameters	Value
Wave number, k	7.9064m
Wave height, $H=2a$	0.0238m
Wave length, λ	0.796m
Wave frequency, f	$1.4s^{-1}$

Table 6.2.2 Mesh generation configuration

	Simulation *No*		
	1	2	3
Wave tank length, x-direction, *L(m)*	4	5.6	7.8
Wave tank height, y-direction, *d(m)*	0.425	0.425	0.425
Wave absorption zone length(m)	λ	1.2 λ	1.5 λ
Cell per wavelength, *cpw* [cells/ λ]	60	80	110
Cell per wave height, *cpw* [cells/ H]	20	30	35

The normalized free surface elevation is plotted in Figure 6.2.2, in which the result from the hybrid solver is compared to the experimental data and other numerical simulation. Figure 6.2.2 shows that the two numerical simulation results generally agree with each other. The largest gap between the experimental and numerical simulation occurs at $(x\text{-}xc)/\lambda=2$, where the experimental data captures a larger amplitude around 1.2a. However, a smaller amplitude is predicted by both the hybrid solver and the numerical simulation of Teixeira (2009).

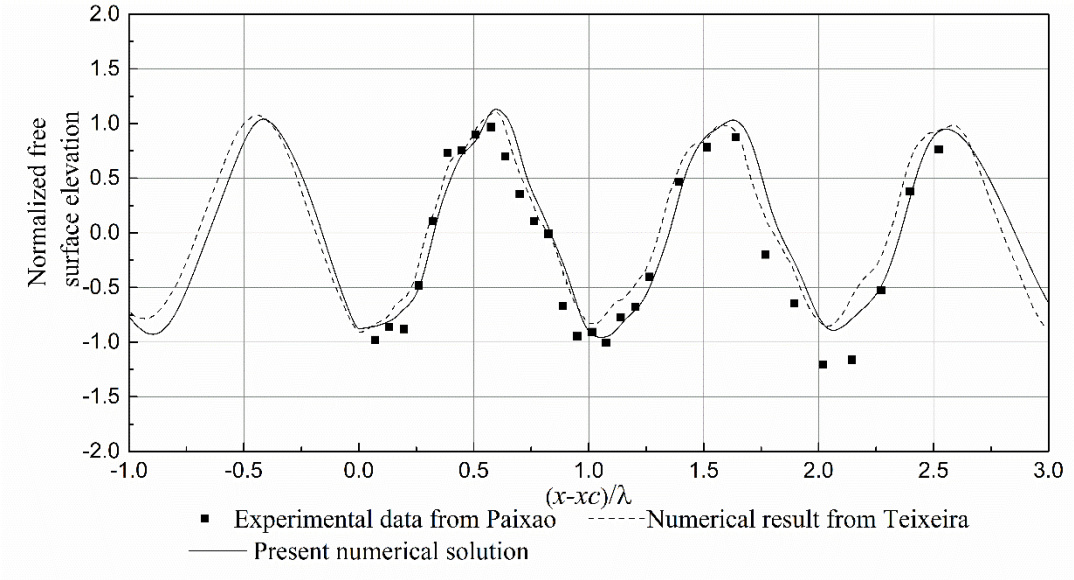

Figure 6.2.2 Comparison of the wave surface elevation profiles

The free surface time histories at different gauges, i.e., $(x\text{-}xc)/\lambda$ = -0.4, 0.055, 0.4052 and 1.006, are also compared, as shown from Figure 6.2.3 to Figure 6.2.6. Figure 6.2.3 only presents the result obtained by numerical simulations since experimental data is not available at guage1. Good agreement is observed between the present hybrid model and that of Teixeira (2009) in literature, which implies that the hybrid solver can give an accurate prediction of the free surface in the tested case.

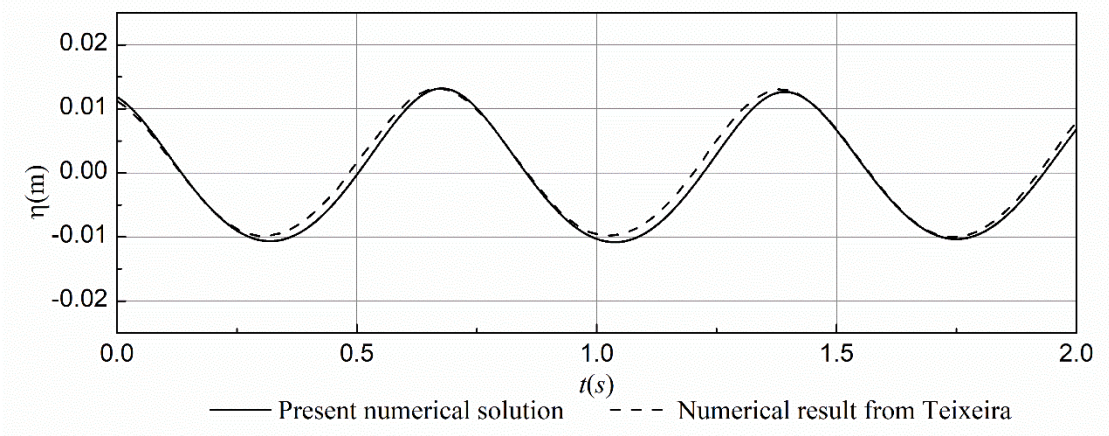

Figure 6.2.3 Free surface time history at $(x\text{-}xc)/\lambda$ = -0.4

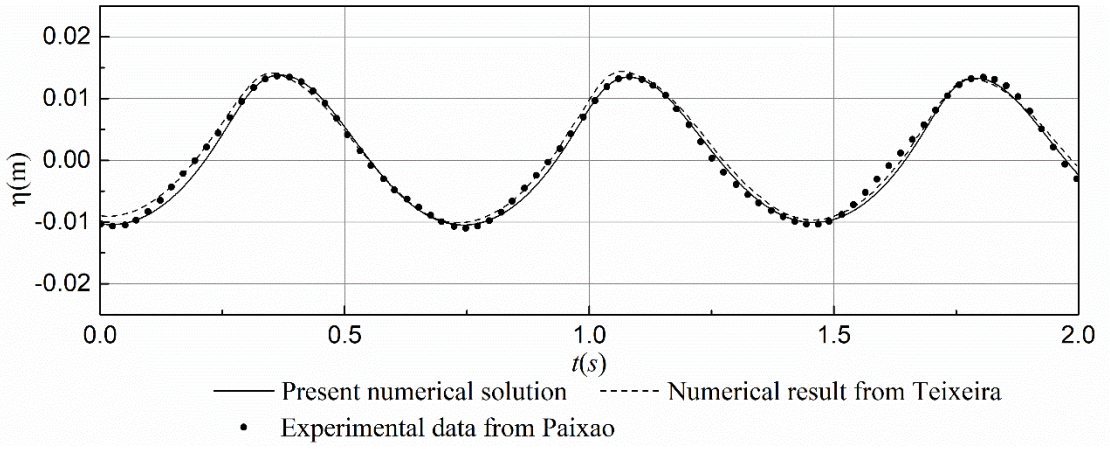

Figure 6.2.4 Free surface time history at $(x\text{-}xc)/\lambda$ =0.055

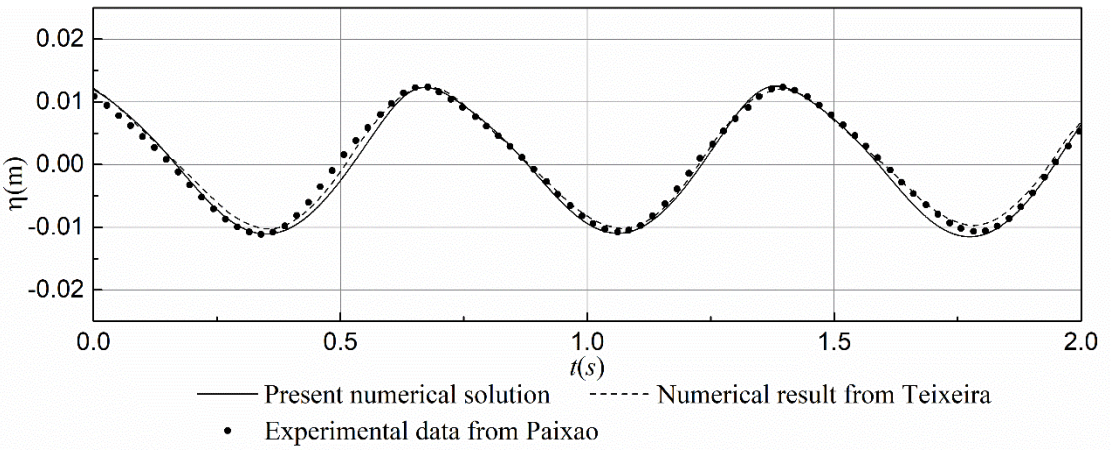

Figure 6.2.5 Free surface time history at $(x\text{-}xc)/\lambda$ =0.4052

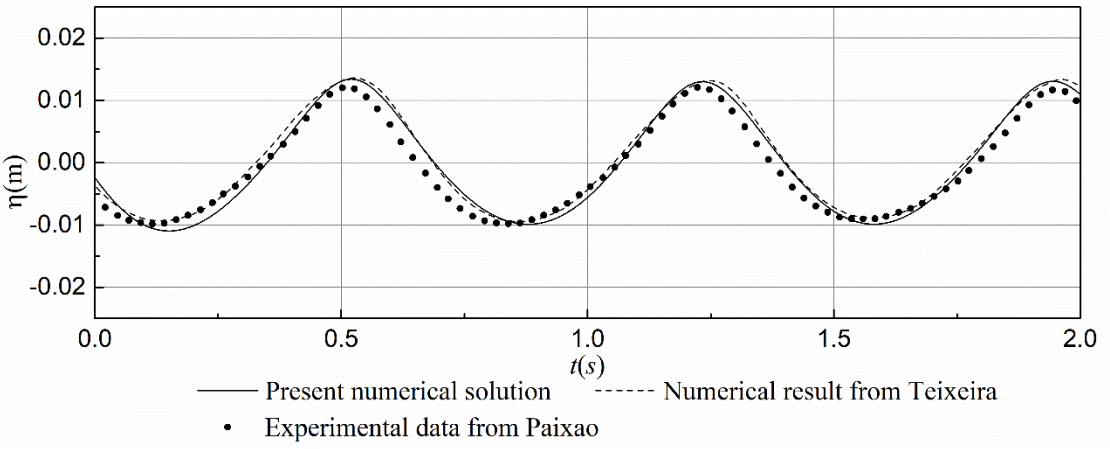

Figure 6.2.6 Free surface time history at $(x\text{-}xc)/\lambda$ =1.006

6.3 Discussion

The validation cases of the hybrid model presented in this chapter illustrate that the hybrid model can give satisfactory results in terms of accuracy for both single- and multi-phase flow, in comparison with the original RANS solver, experimental data and other numerical solutions. It indicates that the present hybrid model provides a good alternative to be employed to simulate turbulent flow. In the next chapter, further numerical tests will be carried out to investigate its efficiency.

7

CASE STUDY OF THE IMPROVEMENT ON EFFICIENCY

7.1 Efficiency test of the single-phase hybrid model

As the main purpose of the proposed hybrid model, the efficiency of the model, especially with the sub-cycle strategy is tested in this section. For this purpose, flows past both the stationary and vibrating circular cylinder are simulated with different sub-cycle numbers (*Ns*). Then the comparison of the performance, i.e., CPU time, between the hybrid solver and the original RANS solver are presented. In addition, all the studied cases are tested on the workstation equipped with the Intel Xeon E5-2660 v3 (Intel Corporation, Santa Clara, CA, USA) of a 2.6GHz processor.

7.1.1 Test on flow passing a stationary cylinder

It should be noted that in the following simulations of the flow passing a stationary circular cylinder with different *Ns*, the minimum domain size and cell number are

adopted based on the conclusions from the convergence tests. The details of how to generate the mesh for both the original RANS solver and hybrid model are explained in Chapter 6.

The CPU time for the simulations is demonstrated in Table.7.1.1, including the mesh number in both the quasi-turbulent domain (Ω_T) and the residual turbulent domain (Ω_R). It should be noted that in terms of the sub-cycle number (*Ns*), there exists a critical sub-cycle number (N_C) which is the maximum value of *Ns* to obtain the acceptable solution. The selection of N_C subject to the concerns of stability and efficiency: (1) the bigger *Ns* generally means larger time step for the quasi-turbulent solver within each time step. Even though an implicit time scheme like backward Euler is applied in the simulation, too large time step may have the difficulty of converging reliably. (2) When a bigger *Ns* is applied, more iterations are taken to achieve the solution satisfies the residual requirement in each loop. Take the cases in Table 7.1.1 with N_C= 5 and 10 for example, larger *Ns* beyond N_C leads to a larger time step in the quasi-turbulent solver and it indicates that more iterations are taken in each loop to satisfy the prescribed residual requirement and therefore, time saving is not demonstrated. Another consequence is that the relative error between the two solvers are beyond the acceptable criteria.

Furthermore, from Table 7.1.1, we can see, an improvement of 44% is achieved by N_C=5 for *Re*=1000. The trend observed is that with the increase of the Reynolds number, the further improvement is achieved, e.g., for the case of *Re*=10000, a 69% saving of the CPU time is achieved with N_C=10 while the corresponding maximum relative error between the two solvers are 4.5% for $\overline{C_D}$ and 1.97% for *St*, respectively.

Table 7.1.1 Comparison of efficiency between the two solvers with a stationary cylinder

Test case	Solver	Sub-cycle number *N*	$C_{L\,rms}$	$\overline{C_D}$	*St*	CPU time (hour)	Mesh cell number
Re=1000 (*Co*=0.3)	Original solver	None sub-cycle	0.5611	1.019	0.201	49.63	197400
	Hybrid solver	*Ns*=2	0.5616	1.021	0.202	33.82	Ω_R : 127400
							Ω_T : 71500
		N_C=5	0.5626	1.025	0.202	28.27	Ω_R : 127400
							Ω_T : 58088
Re=10000 (*Co*=0.3)	Original solver	None sub-cycle	0.639	1.11	0.203	97.95	1340496
	Hybrid solver	*Ns*=2	0.640	1.0	0.205	68.21	Ω_R : 897664
							Ω_T : 595253
		Ns=5	0.637	1.11	0.204	43.14	Ω_R : 897664
							Ω_T : 290535
		N_C=10	0.71	1.06	0.207	29.90	Ω_R : 897664
							Ω_T : 102100
	Max CPU time-saving					69%	

7.1.2 Test on flow passing an oscillating cylinder

In this subsection, two cases of flow passing an oscillating cylinder are considered, (*Re*, *A/D*, *Fr*) = (1000, 0.2, 0.8) and (2300, 0.5, 0.8). The relative error between the original solver and hybrid solver for the two cases are analysed in Table 7.1.2. Apparent efficiency improvement is exhibited, particularly with the increase of the Reynolds number, sub-cycle number and the amplitude ratio. Comparing to the stationary cases, a further improvement of the efficiency is found with a maximum saving of 80% at (*Re*, *A/D*, *Fr*) = (2300, 0.5, 0.8) with N_C=15. The maximum differences between the two solvers are 4.8% for $C_{L\,rms}$ and 2.3% for $\overline{C_D}$, respectively.

Table 7.1.2 Comparison between the two solvers with an oscillating cylinder

Test case (*Re, A/D, Fr*)	Solver	Sub-cycle number N	$C_{L\,rms}$	$\overline{C_D}$	CPU time (hour)	Mesh number
(1000, 0.2,0.8) *Co*=0.2	Original solver	No sub-cycle	0.9000	1.3293	243.21	442288
	Hybrid solver	*Ns*=2	0.9002	1.3290	205.68	Ω_R : 298911
						Ω_T : 203377
		Ns=8	0.9004	1.3293	120.05	Ω_R :298911
						Ω_T : 13965
		Ns=10	0.9006	1.3293	91.77	Ω_R : 298911
						Ω_T : 97656
		N_C=15	0.9005	1.3293	69.64	Ω_R : 298911
						Ω_T : 84502
(2300,0.5, 0.8) *Co*=0.2	Original solver	No sub-cycle	1.89	1.54	609.51	1109520
	Hybrid solver	*Ns*=2	1.89	1.54	452.44	Ω_R : 557396
						Ω_T : 449621
		Ns=6	1.891	1.544	256.92	Ω_R : 557396
						Ω_T : 277644
		Ns=10	1.897	1.55	189.31	Ω_R : 557396
						Ω_T : 103298
		N_C=15	1.98	1.575	120.1	Ω_R : 557396
						Ω_T : 95630
	Max CPU time-saving				80%	

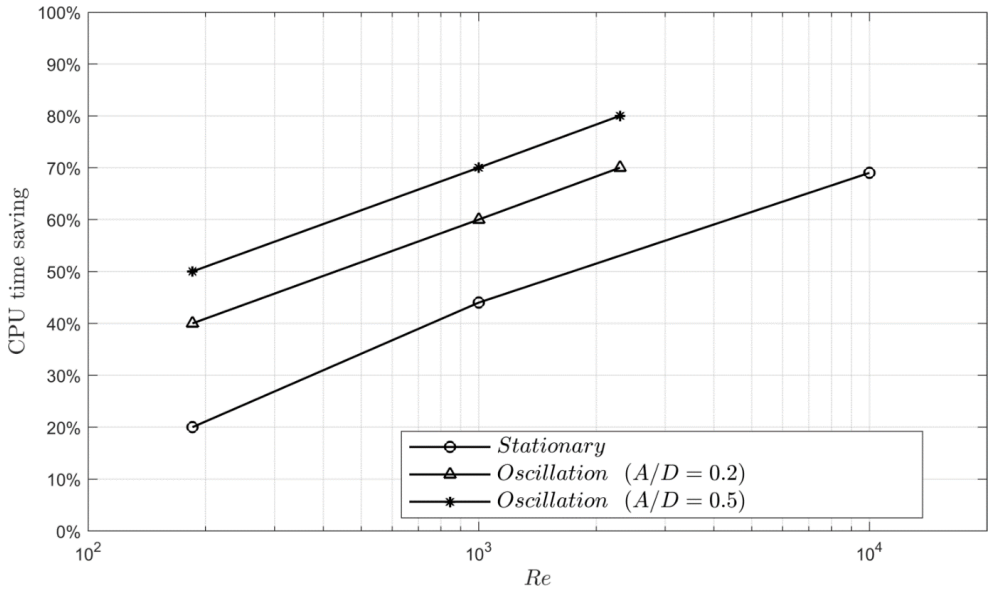

Figure 7.1.1 CPU time saving against the Reynolds number for the studies cases

The CPU time savings as the function of Reynolds number are plotted in the Figure 7.1.1, for both the stationary and oscillating cases. From this figure, we can see, the CPU time-saving is proportional to the Reynolds number. In addition, more time saving is found comparing the low oscillation amplitude cases (*A/D=0.2*) cases with the high oscillation amplitude cases (*A/D=0.5*). The largest CPU time saving can be up to 80% for the cases studies so far. Through the above tests, it can be concluded that the main factors for the selection of proper maximum sub-cycle number (N_C) are: (1) for flow passing the stationary circular cylinder, the Reynolds number is the main factor determining N_C; (2) regarding the flow with an oscillating circular cylinder, the higher Reynolds number and amplitude ratio are both leading to the increase of the CPU time-saving.

7.2 Efficiency test of the multiphase hybrid model

The efficiency test is also conducted for the multiphase hybrid solver with the sub-cycle strategy. The details of the tested wave parameters are given in Table 6.2.1. The size of the quasi-turbulent domain used is 5.6m×0.425m. However, the selection of the overlapping residual turbulent domain size in the multiphase hybrid model is different

to that in the single-phase model. In the multiphase model, there are two characteristic lengths related to the size of the residual turbulent domain: the wave length (λ) and the diameter of the circular cylinder (D). It should be addressed that it is different to the single-phase flow which only has one characteristic length D, e.g., an overlapping domain of $16D \times 50D$ is adopted in the above single-phase cases. Two figures below show the streamlines of the velocity distribution for a circular cylinder subject to either multiphase flow or single-phase flow. In Figure 7.2.1, the separation at downstream caused by the viscous effect cannot be observed, which is different to the velocity streamline in the single-phase flow (see Figure 7.2.2). It also can be observed that the flow acceleration near the cylinder because of the boundary layer effect and due to the oscillatory flow behaviour, there is no recirculation production. The differences between the two illustrated streamlines suggest that the roles played by the viscous effect are different. For the multiphase flow case in Figure 7.2.1, the viscous effect is weak. However, the viscous effect is dominant in the single-phase case in Figure 7.2.2. That is to say, the size of the overlapping zone which close related to the spatial distribution and degree of the viscosity for single phase case cannot be directly employed for the multi-phase case. Moreover, the wavelength should also be taken into consideration. Through the investigations using various domain length, here from 1λ to 4.6λ, it is found that 3λ is enough to obtain the satisfactory result. Therefore, the overlapping domain size finally adopt in this case is $3\lambda \times \mathrm{d} = 2.4m \times 0.425\mathrm{m}$, where d is the water depth.

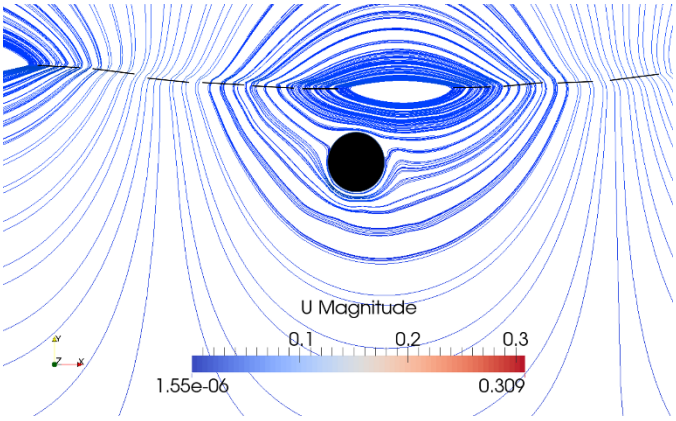

Figure 7.2.1 Streamlines of velocity in the multiphase flow with the dashed line representing the free surface

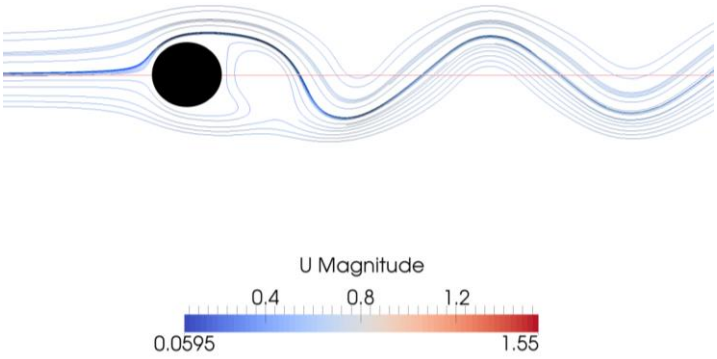

Figure 7.2.2 Streamlines of velocity in the single-phase flow with *Re*=1000

Similar to the single-phase solver efficiency test, different sub-cycle numbers are examined for the multiphase flow using the hybrid model. The CPU time and mesh cell numbers for both the original RANS solver and the hybrid solver with different sub-cycle numbers are demonstrated in Table 7.2.1. With the increase of sub-cycle number, the amount of cell in the overlapping domain does not change (69377) while the cell number in the quasi-turbulent domain decreases (e.g., from 74560 to 44731). The critical sub-cycle number N_C for this case is 5, which means with $N_C \geq 6$ there is no further CPU time saving and meanwhile the relative error between the two solvers is beyond the acceptable criteria. Regarding the efficiency, a 64% CPU time saving is achieved comparing to that of the original RANS solver.

Table 7.2.1 Comparison of efficiency between two solvers

Solver	Sub-cycle number N	CPU time (hour)	Mesh cell number
Original RANS solver	None sub-cycle	39.64	153800
Multiphase hybrid solver	N=2	25.67	Ω_R': 69377
			Ω_T': 74560
	N=3	20.2	Ω_R': 69377
			Ω_T': 59848
	N=4	16.77	Ω_R': 69377
			Ω_T': 53192
	N_C=5	14.25	Ω_R': 69377
			Ω_T': 44731
CPU time saving		64%	

7.3 Conclusion of efficiency tests

The test of efficiency for various working conditions using both the single-phase or the multiphase hybrid solver are performed in this chapter. With the help of a two-way variables transformation technique together with the domain truncation in the spatial point of view and the sub-cycle in the temporal point of review, the primary purpose of the proposed hybrid model is achieved, which is efficiency improvement for simulating the turbulent flow meanwhile maintain good accuracy. Furthermore, it is observed that (1) for the flow past a stationary cylinder, the main influential parameter on the efficiency is the Reynolds number. (2) For the oscillating cylinder, besides the Reynolds number, the amplitude ratio also affects the efficiency of the hybrid solver. The CPU time saving is proportional to both the amplitude ration and Reynolds number. (3) The maximum CPU time saving can be up to 80% compared to the original RANS solver.

8

CONCLUSIONS AND RECOMMENDATIONS

8.1 Conclusions

In this thesis, a new hybrid model coupling the quasi-turbulent model and the residual turbulent model is proposed, which is capable of simulating both single phase and multiphase vortex shedding problem. A functional decomposition approach is adopted in the hybrid model. In the approach, the physical variables are split into two parts. One part is solved by the quasi-turbulent model in the whole domain without solving the equations for turbulence while the second part is solved by using the residual turbulent model in a smaller domain. For this new formulation, the quasi-turbulent model can adopt a much coarser mesh and smaller time step than the residual turbulent model. Therefore, one can use the sub-cycle strategy, in which a number of time steps are marched in the residual turbulent model for one step of the quasi-turbulent model. With the help of the techniques, the efficiency for simulating both single and multiphase turbulent flows associated with vortex shedding is dramatically accelerated.

In addition, some more specific conclusions of this work are summarized as follows:

(1) First of all, both the single and the multiphase hybrid models proposed in this thesis are validated. Extensive tests of the hybrid solver simulation are conducted for single-phase flow around either stationary or vibration cylinder and multiphase flows past stationary circular cylinder near the free surface. The hybrid model solutions are compared to that of the original OpenFOAM and other experimental or numerical data. The agreement of the results from the hybrid model with other available solutions indicates that the accuracy of the proposed hybrid method is sufficient.

(2) In the hybrid method, a two-way variables transformation technique is developed in the coupling of the quasi-turbulent and residual turbulent model. Numerical tests have been demonstrated that this transformation technique can ensure the consistency of fields in the two coupled models and increase the stability of the numerical algorithm. In addition, techniques such as domain truncation in the spatial point of view and the sub-cycle in the temporal point of review are adopted to enhance the efficiency of the proposed hybrid method. The validation conducted in Chapter 6 indicates that the hybrid method using a truncated overlapping domain and the sub-cycle strategy can provide accurate and reliable solutions as the original OpenFOAM solver.

(3) The hybrid method can save significant computational time compared with original OpenFOAM to obtain the similar results for the same cases. It is observed that 80% of the CPU time can be saved, e.g., in the case of an oscillating circular cylinder with (*Re, Fr, A/D*) = (2300, 0.5, 0.9).

8.2 Recommendations

Although a complete hybrid model is suggested in this thesis, there are still some issues that need to be considered in the future work.

1) The RANS turbulent model used here may be replaced by others. Due to the fact that both the RANS and LES models give the turbulent viscosity $\nu_T(x,t)$ required in the momentum equations, the same idea behind this hybrid model could be applied to the LES turbulent model.

$$\frac{\partial u_i}{\partial t} + \left(u_j - u_{bj}\right)\frac{\partial u_i}{\partial x_j} = \frac{\partial}{\partial x_j}\left[\left[\nu + \nu_T(x,t)\right]\left(\frac{\partial u_i}{\partial x_j} + \frac{\partial u_j}{\partial x_i}\right)\right] - \frac{1}{\rho}\frac{\partial p}{\partial x_i} \qquad (i = 1,2)$$

(8.2.1)

Smagorinsky SGS mode: $\nu_T(x,t) = (C_S \Delta f)^2 |\bar{S}|$ (8.2.2)

in which, Δf is the grid filter width; $|\bar{S}|$ is the magnitude of the strain rate tensor; C_S is the Smagorinsky coefficient.

2) At this stage, only two-dimensional model is considered. The methodology employed here can be extended to three-dimensional cases. Furthermore, at this stage, only controlled vibration of the circular cylinder is considered. The free vibration case study should be carried out in the further study as well. Most importantly, a full understanding of the physics of wave-current structure interaction is desired. The hybrid method proposed in the thesis provides an efficient way to achieve more understandings of the interaction between them.
3) Furthermore, the proposed hybrid model provides a principle for coupling with other models. The further attempts can be made to extend the current model to be coupled with the models like potential or viscous potential solver in the far field to deal with more complex issues, e.g., in the following figure. With such more advanced models, more complicated scenarios, like wave-current-structure interactions can be studied. In such cases, larger computational domain is required because the wave propagation simulation generally needs ten wave lengths at least. If the hybrid model is coupled with the potential model, it becomes possible to simulate the complex cases, which is very difficult to be done using the existing method (e.g. OpenFOAM) as they are very time-consuming.

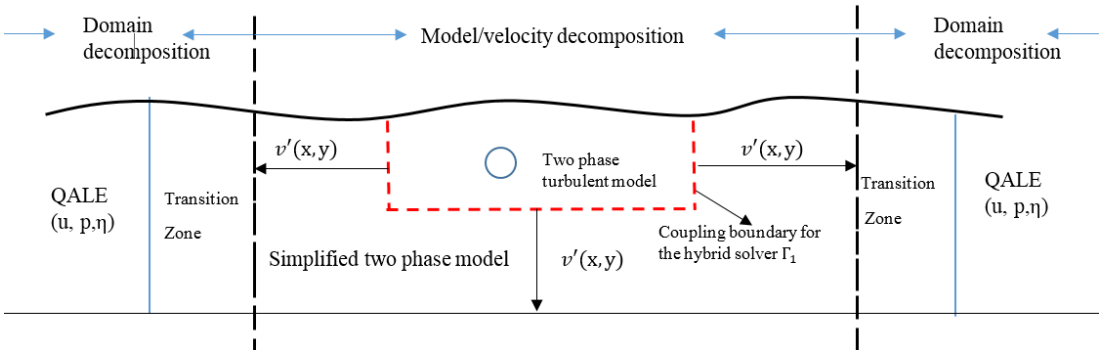

Figure 8.2.1 Sketch of the hybrid model deals with different flow properties with different models

REFERENCES

Al-Jamal, H. & Dalton, C., 2004. Vortex induced vibrations using Large Eddy Simulation at a moderate Reynolds number. *Journal of Fluids and Structures*, 19(1), pp.73–92.

Al-Mdallal, Q.M., Lawrence, K.P. & Kocabiyik, S., 2007. Forced streamwise oscillations of a circular cylinder: Locked-on modes and resulting fluid forces. *Journal of Fluids and Structures*, 23(5), pp.681–701.

Bao, Y. et al., 2016. Generalized thick strip modelling for vortex-induced vibration of long flexible cylinders. *Journal of Computational Physics*, 321(800), pp.1079–1097.

Bardina, J.E., Huang, P.G. & Coakley, T.J., 1997. Turbulence modeling validation, testing, and development. *Nasa Technical Memorandum*, 110446(April), pp.8–20.

Barkley, D. & Henderson, R.D., 1996. Three-dimensional Floquet stability analysis of the wake of a circular cylinder. *Journal of Fluid Mechanics*, 322, pp.215–241.

Bearman, P.W., Graham, J.M.R. & Obasaju, E.D., 1984. A model equation for the transverse forces on cylinders in oscillatory flows. *Applied Ocean Research*, 6(3), pp.166–172.

Bishop, R.E.D. & Hassan, A.Y.Y., 1964. The lift and drag forces on a circular cylinder

oscillating in a flowing fluid. *Proceedings of the Royal Society A: Mathematical, Physical and Engineering Sciences*, 277(1368), pp.51–75.

Blackburn, H.M. & Henderson, R.D., 1999. A study of two-dimensional flow past an oscillating cylinder(261). *Journal of Fluid Mechanics*, 385, pp.255–286.

Blackburn, H.M. & Williamson, 2001. A complementary numerical and physical investigation of vortex-induced vibration. *Journal of Fluids and Structures*, 16(15), pp.399–413.

Blev1ns, R.D. & Burton, T.E., 1976. Fluid forces induced by vortex shedding. *Journal of Fluids Engineering*, (75), pp.19–24.

Breuer, M., 2000. A challenging test case for large eddy simulation: High Reynolds number circular cylinder flow. *International Journal of Heat and Fluid Flow*, 21(5), pp.648–654.

Brika, D., 1995. An experimental study of the aeolian vibrations of a flexible circular cylinder at different incidences. *Journal of Fluids and Structures*, 9(4), pp.371–391.

Brika, D. & Laneville, A., 1993. Vortex-induced vibrations of a long flexible circular cylinder. *Journal of Fluid Mechanics*, 250, pp.481–508.

Carberry, J., Govardhan, R., Sheridan, R., Rockwell, D.,Williamson, C.H.K., 2004. Wake states and response branches of forced and freely oscillating cylinders. *European Journal of Mechanics, B/Fluids*, 23(1), pp.89–97.

Carberry, J., Sheridan, J. & Rockwell, D., 2005. Controlled oscillations of a cylinder: forces and wake modes. *Journal of Fluid Mechanics*, 538(1), p.31.

Carberry, J., Sheridan, J. & Rockwell, D., 2003. Controlled oscillations of a cylinder: A new wake state. *Journal of Fluids and Structures*, 17(2), pp.337–343.

Catalano, P., Wang, M., Iaccarino, G., Moin, P., 2003. Numerical simulation of the flow

around a circular cylinder at high Reynolds numbers. *International Journal of Heat and Fluid Flow*, 24(4), pp.463–469.

Chen, H.C., Lee, S.K., 1996. Interactive RANS/Laplace method for nonlinear free surface flows , *J.Eng. Mech*. 122(February), pp.153–162.

Chen, H.C., Member, A., Lee, S.K., 1999. RANS/Laplace calculations of nonlinear waves induced by surface-piercing bodies. *Journal of Engineering Mechanics*, 125(November), pp.1231–1242.

Chung, M.H., 2016. Two-degree-of-freedom vortex induced vibration of low-mass horizontal circular cylinder near a free surface at low Reynolds number. *International Journal of Heat and Fluid Flow*, 57, pp.58–78.

Coleman, G.N. & Sandberg, R.D., 2010. A primer on direct numerical simulation of turbulence - methods, procedures and guidelines. *Technical Report*, pp.1–21.

Dong, S., Karniadakis1, G.E., Ekmekci, A,. Rockwell, D., 2006. A combined Direct Numerical Simulation–particle image velocimetry study of the turbulent near wake. *Journal of Fluid Mechanics*, 569, pp.185–207.

Dong, S. & Karniadakis, G.E., 2005. DNS of flow past a stationary and oscillating cylinder at Re = 10000. *Journal of Fluids and Structures*, 20(4 SPEC. ISS.), pp.519–531.

Ducrozet, G., Babarit, A. & Gentaz, L., 2011. RANS simulations of a calm buoy in regular and irregular seas using the SWENSE method., 7(May 2016), pp.678–685.

Edmund, D.O., 2012. A Velocity decomposition method for efficient numerical computation of steady external flows, PhD thesis.The University of Michigan.

Edmund, D.O., Maki, K.J. & Beck, R.F., 2013. A velocity-decomposition formulation for the incompressible Navier-Stokes equations. *Computational Mechanics*, 52(3), pp.669–680.

Fan, Z., Zheng, Z.H., Wang, L., Ding, H.X., Cheng, L.J., 2017. Numerical studies of 2D supersonic reactive mixing layer using hybrid RANS/LES method. 21st AIAA *International Space Planes and Hypersonics Technologies Conference*, (March), pp.1–8.

Feng, C. C., 1968. The measurement of vortex–induced effects in flow past stationary and oscillating circular and D-section cylinders. MASc Thesis, University of British Columbia.

Ferrant, P,. Gentaz, L., Monroy, C., Luquet, R., Ducrozet, G., Alessandrini, B., Jacquin, E., Drouet,A., 2007. Recent advances towards the viscous flow simulation of ships manoeuvering in waves. *Ocean Engineering*, (2005), pp.2005–2008.

Ferrant P, Gentaz L, Alessandrini B, L.T. & D., E., 2003. A potential/RANSE approach for regular water wave diffraction about 2-d structures. *Ship Technology Research*, (50), p.50:165–171.

Ferziger, J. & Peric, M., 2012. Computational methods for fluid dynamics. Stanford.University. Springer.

Fröhlich, J. & Rodi, W., 2002. Introduction to large eddy simulation of turbulent flows, Cambridge. Cambridge University Press.

Girimaji, S. & Abdol-Hamid, K., 2005. Partially-Averaged Navier Stokes model for turbulence: implementation and validation. *43rd AIAA Aerospace Sciences Meeting and Exhibit*, (January), pp.1–14.

Gopalan, H., Heinz, S. & Stöllinger, M.K., 2013. A unified RANS-LES model: Computational development, accuracy and cost. *Journal of Computational Physics*, 249, pp.249–274.

Gopalkrishnan, R., 1993. Vortex induced forces on oscillating bluff cylinders. PhD thesis. Cambridge, Massachusetts USA. Department of Ocean Engineering, Massachusetts Institute of Technology.

Gopalkrishnan, R., Triantafyllou, M.S., Triantafyllou G.S,. Barrett, D., 1994. Active vorticity control in a shear flow using a flapping foil. *Journal of Fluid Mechanics*, 274(1), pp.1-21.

Govardhan, R. & Williamson, C.H.K., 2000. Modes of vortex formation and frequency response of a freely vibrating cylinder. *Journal of Fluid Mechanics*, 420, pp.85–130.

Greenshields, C.J., 2017. OpenFOAM. , (July), pp.1–235.

Greenshields, C.J., 2015. OpenFOAM programmer's guide, (December), p.100.

Griffin, O.M. & Ramberg, S.E., 1982. Some Recent Studies of Vortex Shedding With Application to Marine Tubulars and Risers. *Journal of Energy Resources Technology*, 104(1), pp.2–13.

Griffin, O.M. & Ramberg, S.E., 1974. The vortex-street wakes of vibrating cylinders. *Journal of Fluid Mechanics*, 66(3), pp.553-576.

Guilmineau, E. & Queutey, P., 2004. Numerical simulation of vortex-induced vibration of a circular cylinder with low mass-damping in a turbulent flow. *Journal of Fluids and Structures*, 19(4), pp.449–466.

Hafez, M., Shatalov, A. & Nakajima, M., 2009. Improved numerical simulations of incompressible flows based on viscous/inviscid interaction procedures. *Computational Fluid Dynamics 2006 - Proceedings of the Fourth International Conference on Computational Fluid Dynamics*, ICCFD 2006, 36, pp.309–314.

Hafez, M., Shatalov, A. & Wahba, E., 2006. Numerical simulations of incompressible aerodynamic flows using viscous/ inviscid interaction procedures. *Computer Methods in Applied Mechanics and Engineering*, 195(23–24), pp.3110–3127.

Hirt, C.W. & Nichols, B.D., 1981. Volume of fluid (VOF) method for the dynamics of free boundaries. *Journal of Computational Physics*, 39(1), pp.201–225.

Holmes, S., Oakley, O.H. & Constantinides, Y., 2006. Simulation of riser VIV using fully three dimensional CFD simulations. In *Proceedings of OMAE2006 25th International Conference on Offshore Mechanics and Arctic Engineering*. pp. 563–570.

Holzmann, T., 2016. Mathematics, Numerics, Derivations and OpenFOAM®.

Hover, F.S., Miller, S.N. & Triantafyllou, M.S., 1997. Vortex-induced vibration of marine cables: Experiments using force feedback. *Journal of Fluids and Structures*, 11(3), pp.307–326.

Hover, F.S., Techet, A. H. & Triantafyllou, M.S., 1998. Forces on oscillating uniform and tapered cylinders in cross flow. *Journal of Fluid Mechanics*, 363, pp.97–114.

Hover, F.S., Tvedt, H. & Triantafyllou, M.S., 2001. Vortex-induced vibrations of a cylinder with tripping wires. *Journal of Fluid Mechanics*, 448, pp.175–195.

Issa, R.I., 1986. Solution of the implicitly discretised fluid flow equations by operator-splitting. *Journal of Computational Physics*, 62(1), pp.40–65.

Jasak, H. & Tuković, Ž., 2006. *Automatic mesh motion for the unstructured Finite Volume Method.* Transactions of Famena. 30(2):1–18.

Khalak, A. & Williamson, C.H.K., 1997. Fluid forces and dynamics of a hydroelastic structure with very low mass and damping. *Journal of Fluids and Structures*, 11(8), pp.973–982.

Kim, K., 2004. *A viscous-inviscid interaction study using complementary RANS equations*. PhD thesis.The Univerisity of Michigan.

Kim, K., Sirviente, A.I. & Beck, R.F., 2005. The complementary RANS equations for the simulation of viscous flows. *International Journal for Numerical Methods in Fluids*, 48(2), pp.199–229.

Kim, S., 2014. Large eddy simulation of forces and wake modes of an oscillating cylinder. PhD thesis. University of Southampton.

Kocutar, P., Škerget, L. & Ravnik, J., 2015. Hybrid LES/URANS simulation of turbulent natural convection by BEM. *Engineering Analysis with Boundary Elements*, 61, pp.16–26.

Leonard, A., 1975. Energy cascade in large-eddy simulations of turbulent fluid flows. *Turbulent Diffusion in Environmental Pollution Proceedings of a Symposium held at Charlottesville*, Volume 18, pp.237–248.

Li, Q., Ma, Q.W. & Yan, S., 2015. Investigations on the feature of turbulent viscosity associated with vortex shedding. *Procedia Engineering*, 126, pp.73–77.

Lighthill, M.J., 1958. On displacement thickness. *Journal of Fluid Mechanics,* 4(4), p.383-392.

Lin, J.C. & Rockwell, D., 1996. Force identification by vorticity fields:techniques based on flow imaging. *Journal of Fluids and Structures*, 10(6), pp.663–668.

Lin, J.C., Towfighi, J. & Rockwell, D., 1995. Instantaneous structure of the near-wake of a circular cylinder : on the effect of Reynolds number. *Journal of Fluids and Structures*, 9, pp.409–418.

Low, H.T., Chew, Y.T. & Tan, K.T., 1989. Fluid forces on a cylinder oscillating in line with a uniform flow. *Ocean Engineering*, 16(3), pp.307–318.

Luquet, R. et al., 2007. Simulation of a TLP in waves using the SWENSE scheme. *Proceedings of the International Offshore and Polar Engineering Conference*, pp.1916–1922.

Lynett, K.I.S. and P.J. & Coastal, 2010. Multi-scale simulation with a hybrid Boussinesq-RANS hydrodynamic model. *International Journal For Numerical Methods In Fluids*, (October 2007), pp.601–629.

Martínez Ferrer, P.J. et al., 2016. A multi-region coupling scheme for compressible and incompressible flow solvers for two-phase flow in a numerical wave tank. *Computers and Fluids*, 125, pp.116–129.

Menter, F., 1993. Zonal two equation k-w turbulence models for aerodynamic flows. In 23rd Fluid Dynamics, Plasmadynamics and Lasers Conference. AIAA-93-2906.pp.1-22.

Menter, F., Kuntz, M. & Bender, R., 2003. A Scale-Adaptive Simulation Model for Turbulent Flow Predictions. *AIAA Paper*, 2003–767(January).

Menter, F.R., 1994. Two-equation eddy-viscosity turbulence models for engineering applications. *AIAA journal*, 32(8), pp.1598–1605.

Monroy, C. & Ducrozet, G., 2009. Simulations of Ship motins in regular and irregular Head Seas using the SWENSE Method. *Proceedings of the Nineteenth (2009) International Offshore and Polar Engineering Conference*, pp.458–465.

Moreau, F. & Huang, S., 2010. Model testing on cross-flow vortex-induced vibration in combined in-line current and oscillatory flows. *OMAE2010*, pp.1–6.

Morse, T.L. & Williamson, C.H.K., 2009. Prediction of vortex-induced vibration response by employing controlled motion. *Journal of Fluid Mechanics*, 634, pp.5-39.

Narayanaswamy, M. et al., 2010. Hybrid model for coastal wave propagation. *Journal of Hydraulic Research*, 48(SUPPL. 1), pp.85–93.

Noca, F., Shiels, D. & Jeon, D., 1999. A comparison of methods for evaluating time-dependent fluid dynamic forces on bodies, using only velocity fields and their derivatives. *Journal of Fluids and Structures*, 13, pp.551–578.

Norberg, C., 2003a. Fluctuating lift on a circular cylinder: review and new measurements. *Journal of Fluids and Structures*, 17(1), pp.57–96.

Norberg, C., 2003b. Fluctuating lift on a circular cylinder: review and new measurements. *Journal of Fluids and Structures*, 17(1), pp.57–96.

Norberg, C., 1998. LDV-measurements in the near wake of a circular cylinder. *Advances in understanding of bluff body wakes and vortex-induced vibration*, Washington *DC* (June), pp.1–12.

Ong, M.C., Utnes.T., Holmedal, L.E., Myrhaug, D., Pettersen, B., 2009. Numerical simulation of flow around a smooth circular cylinder at very high Reynolds numbers. *Marine Structures*, 22(2), pp.142–153.

Ongoren, A. & Rockwell, D., 1988. Flow structure from an oscillating cylinder Part 2. Mode competition in the near wake. *Journal of Fluid Mechanics*, 191(1), p.225-245.

Paixão Conde, J.M., 2009. Nonlinear wave diffraction by submerged horizontal circular cylinder. *International Journal of Offshore and Polar Engineering*, 19(3), pp.198–205.

Pan, Z.Y., Cui, W.C. & Miao, Q.M., 2007. Numerical simulation of vortex-induced vibration of a circular cylinder at low mass-damping using RANS code. *Journal of Fluids and Structures*, 23(1), pp.23–37.

Park, J., Kwon, K. & Choi, H., 1998. Numerical solutions of flow past a circular cylinder at Reynolds numbers up to 160. *KSME International Journal*, 12(6), pp.1200–1205.

Parnaudeau, P., Carlier, J., Heitz, D., Lamballais, E., 2008. Experimental and numerical studies of the flow over a circular cylinder at Reynolds number 3900. *Physics of Fluids*, 20(8),pp.85-101.

Pham, A.H., Lee, C.Y., Seo, J.H., Chun, H.H., Kim, H.J., Yoon, H.S., Kim, J.H., Park, D.W., Park, R.I., 2010. Laminar flow past an oscillating circular cylinder in cross flow. *Journal of Marine Science and Technology*, 18(3), pp.361–368.

Pope, S.B., 2000. *Turbulent Flows*, Cambridge University Press.

Prosperetti, A. & Tryggvason, G., 2015. *Computational Methods for Multiphase Flow*, Cambridge. Cambridge University Press.

Quéméré, P. & Sagaut, P., 2002. Zonal multi-domain RANS/LES simulations of turbulent flows. *International Journal for Numerical Methods in Fluids*, 40(7), pp.903–925.

Quéméré, P., Sagaut, P. & Couailler, V., 2001. A new multi-domain/multi-resolution method for large-eddy simulation. *International Journal for Numerical Methods in Fluids*, 36(4), pp.391–416.

Rahman, M.M., Karim, M.M. & Alim, M.A., 2007. Numerical investigation of unsteady flow past a circular cylinder using 2-D finite volume method. *Journal of Naval Architecture and Marine Engineering*, 4(1), pp.27–42.

Rhie, C.M., 1982. A numerical study of the turbulent flow past an isolated airfoil with trailing edge separation. AIAA/ASME 3rd Joint *Thermophysics,Fluids,Plasma and Heat Transfer Conference*.pp.1-12.

Robert, S. & Zang, J., 2012. Evaluation of urans solvers for cylindrical structures in tidal flow. *the validation of all kinds of turbulence model in OpenFOAM*, 4, pp.703–708.

Rodi, W., 1997. Comparison of LES and RANS calculations of the flow around bluff bodies. *Journal of Wind Engineering and Industrial Aerodynamics*, 69–71, pp.55–75.

Rosemurgy, W.J. Edmund, D.O., Maki, K.J., Beck, R.F.,2012. A velocity decomposition approach for steady free-surface flow. 29th Symposium on Naval Hydrodynamics, pp.26–31.

Sajjadi, H., Salmanzadeh, M., Ahmadi, G., Jafari, S., 2017. Turbulent indoor airflow simulation using hybrid LES / RANS model utilizing Lattice Boltzmann method. *Computers and Fluids*, 150, pp.66–73.

Sarpkaya, T., 2003. A critical review of the intrinsic nature of vortex induced vibrations. *J Fluid Struct*, 19(June), pp.389–447.

Schewe, G., 1983. On the force fluctuations acting on a circular cylinder in crossflow from subcritical up to transcritical Reynolds numbers. *Journal of Fluid Mechanics*, 133(1), pp.265-285.

Schulz, K.W. & Trond S. Meling, 2004. Multi-strip numerical analysis for flexible riser response. In *Proceedings of OMAE 23rd International Conference on Offshore Mechanics and Arctic Engineering Proceedings of OMAE04*. pp. 2–7.

Selvam, R.P., 1997. Finite element modelling of flow around a circular cylinder using LES. *Journal of Wind Engineering and Industrial Aerodynamics*, 67–68, pp.129–139.

Sheridan, J., Carberry, J.,1998. On the near-wake topology of an oscillating cylinder. *Journal of Fluids and Structures.*, 12, pp.215–220.

Spalart, P.R. Zhou, W.H., Strelets, M., Allmaras, S.R., 1997. Comments on the feasibility of LES for wings and on a hybrid RANS/LES approach. *Advances in DNS/LES*, 1(January), pp.4–8.

Spalart, P.R., 2000. Strategies for turbulence modelling and simulations. *International Journal of Heat and Fluid Flow*, 21(3), pp.252–263.

Sriram, V., Ma, Q.W. & Schlurmann, T., 2014. A hybrid method for modelling two dimensional non-breaking and breaking waves. *Journal of Computational Physics*, 272, pp.429–454.

Staubli, T., 1983. Calculation of the vibration of an elastically mounted cylinder using experimental data from forced oscillation. *Journal of Fluid Engineering*, 105, pp.225–229.

Stern, F., Yoo, S.Y. & Patel, V.C., 1988. Interactive and large-domain solutions of

higher-order viscous-flow equations. *AIAA Journal*, 26(9), pp.1052–1060.

Stringer, R.M., Zang, J. & Hillis, a. J., 2014. Unsteady RANS computations of flow around a circular cylinder for a wide range of Reynolds numbers. *Ocean Engineering*, 87, pp.1–9.

Sumer, B.M. & Fredsoe, J., 2006. *Hydrodynamics Around Cylindrical structures*. Technical University of Denmark, Denmark. World Scientific Publishing.

Teixeira, P.R.D.F., 2009. Numerical simulation of the interaction of a regular wave and a submerged cylinder. *Proceedings 2009 3rd Southern Conference on Computational Modeling, MCSUL 2009*, 8(June), pp.43–48.

Ünal, U.O., Atlar, M. & Gören, Ö., 2010. Effect of turbulence modelling on the computation of the near-wake flow of a circular cylinder. *Ocean Engineering*, 37(4), pp.387–399.

Utyuzhnikov, S. V, 2005. Generalized wall functions and their application for simulation of turbulent flows. *International Journal For Numerical Methods In Fluids*, 47, pp.1323–1328.

Vecchi, A., 2009. Wake dynamics of flow past a curved circular cross-section body under cross-flow vibration, PhD thesis. Imperial College London.

Verley, R.L.P., 1982. A simple model of vortex-induced forces in waves and oscillating currents. *Applied Ocean Research*, 4(2), pp.117–120.

Wang, B.M. & Catalano, P., 2001. Prediction of high Reynolds number flow over a circular cylinder using LES with wall modeling. *Center for Turbulence Research Annual Research Briefs*, pp.45–50.

Wang, J., 2016. A hybrid model for large scale simulation of unsteady nonlinear waves. PhD thesis. London, City, University of London.

Wang, J., Ma, Q.W. & Yan, S., 2016. A hybrid model for simulating rogue waves in random seas on a large temporal and spatial scale. *Journal of Computational Physics*, 313(February), pp.279–309.

Wei, Q., Chen, H. & Ma, Z., 2016. A hybrid RANS/LES model for simulation of complex turbulent flow. *Journal of Hydrodynamics, Ser. B*, 28(5), pp.811–820.

Weller, H.G. & Tabor, G., 1998. A tensorial approach to computational continuum mechanics using object-oriented techniques. *Computers in Physics*, 12(6), pp.620–631.

Williamson, C.H.K. & Roshko, A., 1988. Vortex formation in the wake of an oscillating cylinder. *Journal of Fluids and Structures*, 2(4), pp.355–381.

Xiao, H. & Jenny, P., 2012. A consistent dual-mesh framework for hybrid LES/RANS modeling. *Journal of Computational Physics*, 231(4), pp.1848–1865.

Yan, S. & Ma, Q., 2017. A hybrid approach coupling MLPG-R with QALE-FEM for modelling fully nonlinear water waves. In *Proceedings of the Twenty-seventh (2017) International Ocean and Polar Engineering Conference San*. pp. 654–661.

Yokoi, Y. & Kamemoto, K., 1994. Vortex shedding from an oscillating circular cylinder in a uniform flow. *Experimental Thermal and Fluid Science*, 8(2), pp.121–127.

Zdero, R., Turan, Ö. & Havard, D.G., 1995. Toward understanding galloping: Near-wake study of oscillating smooth and stranded circular cylinders in forced motion. *Experimental Thermal and Fluid Science*, 10(1), pp.28–43.

Zdravkovich, M.M., 1990. Conceptual overview of laminar and turbulent flows past smooth and rough circular cylinders, *J.of Wind Engineering* No,37, pp.53–62.

APPENDIX A

The shear -rate/viscous stress tensor $\boldsymbol{\tau}$ for Newtonian fluids is described as:

$$\boldsymbol{\tau} = 2v\boldsymbol{D} - [\frac{2}{3}\boldsymbol{v} + \kappa](\nabla \cdot \boldsymbol{U})\boldsymbol{I} \tag{a. 1}$$

In which $\boldsymbol{D}$ is the deformation rate/strain-rate tensor, it can be obtained by

$$\boldsymbol{D} = \frac{1}{2}[\nabla \otimes \bar{U} + (\nabla \otimes \bar{U})^T] = \frac{1}{2}\left[\frac{\partial \bar{u}_i}{\partial x_j} + \frac{\partial \bar{u}_j}{\partial x_i}\right] \tag{a. 2}$$

where T stands for the transpose operation. Further simplifications conducted by using the continuity equation $\nabla \cdot \bar{\boldsymbol{U}} = 0$ into Equation (a.1), the simplified shear-rate tensor can be obtained as

$$\boldsymbol{\tau} = 2v\boldsymbol{D} \tag{a. 3}$$

The deviatoric part of a matrix is calculated by

$$\boldsymbol{A^{dev}} = \boldsymbol{A} - \boldsymbol{A^{hyd}} = \boldsymbol{A} - \frac{1}{3}\mathrm{tr}(\boldsymbol{A})\boldsymbol{I} \tag{a. 4}$$

where

$$\boldsymbol{A} = [grad(\bar{U})]^{\boldsymbol{T}} = (\nabla \otimes \bar{U})^{\boldsymbol{T}} \tag{a. 5}$$

The function in OpenFOAM (Holzmann 2016) used to deal with this term is similar to substitute the above into Equation (a.4), one has

$$dev[\nabla \otimes \bar{U}]^{\boldsymbol{T}} = [\nabla \otimes \bar{U}]^{\boldsymbol{T}} - \frac{1}{3}\mathrm{tr}\big((\nabla \otimes \bar{U})^{\boldsymbol{T}}\big)\boldsymbol{I} \tag{a. 6}$$

Finally, put everything together, and it ends up with:

$$-\nabla \cdot \overline{\boldsymbol{\tau_{eff}}} = -\nabla \cdot (v_{eff}(\nabla \otimes \bar{U})) - \nabla \cdot \left\{v_{eff}[(\nabla \otimes \bar{U})^{\boldsymbol{T}} - \frac{1}{3}\mathrm{tr}\big((\nabla \otimes \bar{U})^{\boldsymbol{T}}\big)\boldsymbol{I}]\right\} \tag{a. 7}$$

Rearranging the equation yields

$$-\nabla \cdot \overline{\boldsymbol{\tau_{eff}}} = -\nabla \cdot \left\{ v_{eff}(\nabla \otimes \bar{U}) + v_{eff}[\nabla \otimes \bar{U}]^{\boldsymbol{T}} - \frac{1}{3} tr\left((\nabla \otimes \bar{U})^{\boldsymbol{T}}\right) \boldsymbol{I} \right\} \quad \text{(a. 8)}$$

Rewrite the last term by using the relation $\nabla \cdot \boldsymbol{U} = tr(\boldsymbol{D})$, thus

$$-\nabla \cdot \overline{\boldsymbol{\tau_{eff}}} = -\nabla \cdot \left\{ v_{eff}(\nabla \otimes \bar{U}) + (v_{eff}(\nabla \otimes \bar{U})^{\boldsymbol{T}} - \frac{1}{3}\left(v_{eff}(\nabla \cdot \bar{U})\right) \boldsymbol{I} \right\} \quad \text{(a. 9)}$$

The last term is zero due to the continuity of the flow. Therefore, the effective shear rate tensor $\overline{\boldsymbol{\tau_{eff}}}$ for the incompressible fluids can be described as:

$$\begin{aligned} -\nabla \cdot \overline{\boldsymbol{\tau_{eff}}} &= -\nabla \cdot \left(v_{eff}(\nabla \otimes \bar{U})\right) + (v_{eff}(\nabla \otimes \bar{U})^{\boldsymbol{T}}) \\ &= -\nabla \cdot \left(2v_{eff}\left[\frac{1}{2}\{(\nabla \otimes \bar{U}) + (\nabla \otimes \bar{U})^{\boldsymbol{T}}\}\right]\right) \\ &= -\nabla \cdot (2v_{eff}\bar{\boldsymbol{D}}) \end{aligned} \quad \text{(a. 10)}$$

Regarding the influence of turbulence models, as we saw in the section above, the equations for full resolved eddies, Reynolds-Averaged flow field are identical. The only difference is related to the viscosity. Hence, if the turbulence model is not employed, the contribution of the turbulent viscosity v_t is zero, which follows as

$$v_{eff} = v \quad \text{(a. 11)}$$

The most common hypothesis is the theory postulated by Boussinesq (1879) that simply relates the turbulence of a flow to a higher fluid viscosity. The thought behind is as follows: If we have a higher turbulence flow, the flow gets more chaotic and a lot of vortexes that can transport. Therefore, to achieve that one can increase the diffusion coefficient (the viscosity in the momentum equation) and keep the rest as it is. In other words, the molecular viscosity is increased by the so-called eddy or turbulent viscosity.

This assumption provides the possibility to model the smallest vortexes by using correlations and approximations and only resolve the larger eddies. Boussinesq (1879) related the Reynold stresses $-\rho\overline{u_i' u_j'}$ to the mean values of the velocity and the kinetic energy of the turbulence *k* as

$$-\overline{u_i' u_j'} = \nu_T\left(\frac{\partial \bar{u}_i}{\partial x_j} + \frac{\partial \bar{u}_j}{\partial x_i} - \frac{2}{3}(\nabla \cdot \bar{U})\delta_{ij}\right) - \frac{2}{3}\kappa\delta_{ij} \quad \text{(a. 12)}$$

There are a lot of confusion about the term $-\frac{2}{3}k\delta_{ij}$, this term is put into a modified pressure. If compare the term $\frac{2}{3}k\delta_{ij}$ seems to behave like a pressure term. Within the OpenFOAM toolbox, the term of $\frac{2}{3}k\delta_{ij}$ is put into a modified pressure, which is introduced as $p^* = p + \frac{2}{3}\kappa$.

APPENDIX B

With respect to the flow subject to the volume change, there is one additional rate of change term appears. This term is handled automatically for it is naturally satisfied. Mesh motion flux that accounts for the grid convective in all convective terms and needs to be accounted for algorithmically. The relationship between the volume change rate and the grid velocity is governed by the space conservation law, i.e.

$$\eta \frac{d}{dt} \int_{\Omega_i} d\Omega - \oint_S u_b \cdot dS = 0 \qquad \text{(c. 1)}$$

While Equation (c. *1*) is always satisfied in the integral form, it also needs to be preserved in the discrete form in Equation (c. 2)

$$\frac{V_p^{N+1} - V_P^N}{\Delta t} - \sum_f F_s = 0 \qquad \text{(c. 2)}$$

For this reason, the mesh motion flux F_s is calculated as the volume swept by the face *f* in the motion during the current time step rather than from the grid velocity u_b, to be consistent with the cell volume calculation.

APPENDIX C

It is well known that turbulence vanishes near a wall due to the no-slip boundary condition for the velocity as well as the blocking effect caused by the wall. In the vicinity of the wall, there is a thin sublayer with predominantly molecular diffusion.

The total shear stress is the sum of the viscous stress and the Reynolds stress. Right at the wall, the no-slip boundary condition $u_i = 0$ implies that all Reynolds stresses are zero. Hence, all the wall shear stress is due to the viscous contribution. This contrasts with the free shear flows where the viscous stresses are everywhere negligible compared with the Reynolds stresses. Consequently, close to walls the viscosity and the wall shear stress are important parameters. The viscous scales are defined by appropriate velocity and length scales in the near wall region. These are the friction velocity

$$u_\tau = \sqrt{\frac{\tau_w}{\rho}} \tag{d. 1}$$

In addition, the viscous length scale is given as

$$\delta_\nu = \nu \sqrt{\frac{\rho}{\tau_w}} = \frac{\nu}{u_\tau} \tag{d. 2}$$

The distance from the wall measured in viscous lengths or wall units is defined as

$$y^+ = \frac{y}{\delta_\nu} = \frac{u_* y}{\nu} \tag{d. 3}$$

where y^+ is the non-dimensional wall distance for a wall-bounded flow; u_* is the friction velocity at the nearest wall; y is the distance from the first cell to the wall; ν is the kinematic viscosity of the flow. Different regions in the near wall flow are defined based on the magnitude of y^+. In the viscous wall region $y^+ < 50$, the viscosity contributes to the shear stress. Outside this region, the effect of viscosity is negligible. In the viscous sublayer$y^+ < 5$, the Reynolds shear stress is negligible compared with the viscous stress. Various wall treatment based on different y^+ are illustrated in Figure 8.2.1.

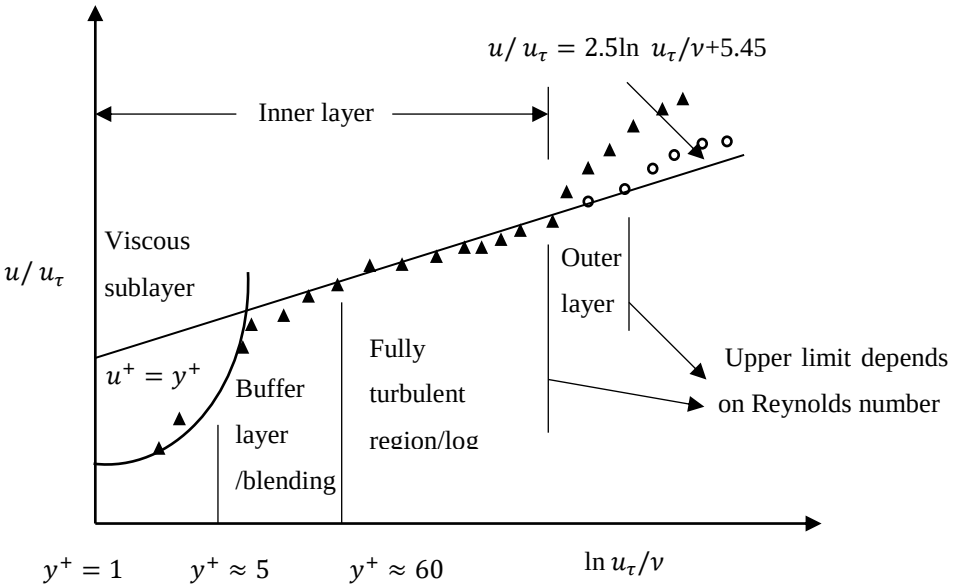

Figure 8.2.1 Various wall treatment based on different y^+

APPENDIX D

How the single-phase quasi-turbulent and residual turbulent model to be solved numerically using the finite volume method have been demonstrated in section 5.4. In this Appendix, the numerical implementation of the multiphase governing equation in OpenFOAM will be introduced.

For clarity, these equations are rewritten to be vector form, where *U* and *U** are the velocity vectors used by the multiphase quasi-turbulent model and the residual turbulent model, respectively. Accordingly, p and p^* are used to replace the pressure in the multiphase quasi-turbulent model and the residual turbulent model, respectively. The governing equations are discretized using the finite-volume method for the temporal, convection, Laplacian, surface tension and gravity force term with corresponding discretisation schemes.

The discretization procedure is same to the single-phase momentum equation, and the equation obtained after the discretization is given by

$$\frac{\rho_P^{n+1}U_P^r - \rho^n U_P^n}{\Delta t}\Omega_P + \sum_{f\in\partial\Omega_i}\rho^f\phi_f^n U_f^{r\prime} = \sum_{f\in\partial\Omega_i}\mu_f^{n+1}\left(\nabla\frac{1}{f}U\right)^{r'}\left|S_f\right| + \nabla U_P^n\cdot\nabla\mu_p^{n+1}\Omega_P \tag{e. 1}$$

in which, ρ^f is density on the face f; ρ_P is the density at cell P; μ_P is the dynamic viscosity at cell *P*. In the multiphase flow, the density and dynamic viscosity are given by

$$\rho = \rho_w\alpha + \rho_{air}(1-\alpha) \tag{e. 2}$$

$$\mu = \mu_w\alpha + \mu_{air}(1-\alpha) \tag{e. 3}$$

where μ_w and μ_{air} are densities of water and air, respectively. Because the update of α is before solving the momentum equation and therefore, the density and dynamic viscosity fields are known in advance.

Same to the single-phase momentum equation, a matrix is finally obtained after the discretisation, i.e.,

$$A_P U_P^r = \left(\sum_{\forall N} A_N U_N^m + E_P^n \right) = H(U^m) \tag{e.4}$$

The quantities of A_P, A_N and E_P have the same form as these in the single-phase equation, but the difference is the multiphase equation includes the effect of surface tension and gravity forces, which given as

$$\phi_f^r = \left(\frac{H(U^m)}{A_P} \right)_f \cdot S_f + \left(\left(\frac{1}{A_P} \right)_f (\sigma\kappa)_f^{n+1} \left(\nabla \frac{1}{f} \alpha \right)^{n+1} \right) |S_f| - \left(\left(\frac{1}{A_P} \right)_f (g \cdot x)_f^{n+1} \left(\nabla \frac{1}{f} \rho \right)^{n+1} |S_f| \right) \tag{e.5}$$

where the surface gradient operator has been adopted, i.e.,

$$(\nabla \alpha)_f^{n+1} \cdot S_f = \left(\nabla \frac{1}{f} \alpha \right)^{n+1} |S_f|$$

and

$$\phi_f^{m+1} = \phi_f^r - \left(\frac{1}{A_P} \right)_f \left(\nabla \frac{1}{f} p_d^{m+1} \right) |S_f| \tag{e. 6}$$

To solve the pressure field p_d^{m+1}, the law of mass conservation is used for the incompressible flow, which is given as

$$\sum_{f \in \partial\Omega_i} \phi_f^{m+1} = 0 \tag{e. 7}$$

Then, substituting (e. 6) to (e. 7), it leads to

$$\sum_{f \in \partial\Omega_i} \left(\frac{1}{A_P} \right)_f \left(\nabla \frac{1}{f} p_d^{m+1} \right) |S_f| = \sum_{f \in \partial\Omega_i} \phi_f^r \tag{e.8}$$

Same to the single-phase solver, a linear system for p_d^{m+1} can be achieved and solved. Therefore, ϕ_f^{m+1} can be updated then. Finally, U_p^{m+1} can be updated by the following equation which shares a same form with the single-phase solver.

$$U_p^{m+1} = U_P^r + \frac{1}{A_P}\left(\sum_{f\in\partial\Omega_i}\frac{\left(S_f \otimes S_f\right)}{|S_f|}\right)^{-1} \cdot \left(\sum_{f\in\partial\Omega_i}\left(\frac{\phi_f^{m+1} - (U_P^r)_f \cdot S_f}{\left(\frac{1}{A_P}\right)_f}\right)\frac{S_f}{|S_f|}\right) \tag{e.9}$$

This procedure is repeated several times to ensure that the velocity and pressure field together satisfy both continuity and momentum equations. At the end of the iteration procedure, the values corresponding to the M^{th} iteration are assigned to the corresponding values at the new time step $(n+1)$, i.e.,

$$\phi_f^{n+1} = \phi_f^M,\ U^{n+1} = U^M \text{ and } P^{n+1} = P^M \tag{e.10}$$

APPENDIX E

The predicted flux to be compensated by the pressure gradient is evaluated as $(\phi_{H/A} - \phi)$, both of which are searched from the database, as the pressure diffusivity used to calculate the gradient

$$\nabla(p) = \frac{\phi_{H/A} - \phi}{|S_f| D_p} \quad \text{(f. 1)}$$

where ϕ is the flow flux, D_p is the pressure diffusivity, S_f is the patch face areas.

APPENDIX F

The author's publications by the date of submitting this thesis are listed below:

[1] Qian Li, Q.W. Ma, S. Yan, *2015.* Investigations on The Feature of Turbulent Viscosity Associated with Vortex Shedding, *Procedia Engineering*, volume 126, pp.73-77.

[2] Q. Li, Q.W. Ma, S. Yan, 2017. Vortex Shedding Behaviour of a Horizontal Circular Cylinder near the Free Surface with Different Submerged Depths. *Proceedings of the Twenty-Seventh International Ocean and Polar Engineering Conference*, San Francisco, CA, USA, pp.1160-1165.